Defect chemistry of single crystalline MgO(001) films

Dissertation zur Erlangung des akademischen Grades des
Doktors der Naturwissenschaften (Dr. rer. nat.)

eingereicht im Fachbereich Physik
der Freien Universität Berlin

vorgelegt von

Frau Dipl.-Phys. Anastasia Gonchar
geboren am 12.06.1986 in Rostow-am-Don, Russland

Berlin 2011

Die vorliegende Arbeit wurde im Zeitraum Juli 2008 bis Juni 2011 am Fritz-Haber-Institut der Max-Planck-Gesellschaft, Abteilung Chemische Physik, unter der Leitung von Prof. Dr. H.-J. Freund angefertigt.

1. Gutachter: Prof. Dr. Hans-Joachim Freund
2. Gutachter: Prof. Dr. Robert Bittl

Disputation am: 5 July 2011

You see things; and you say, 'Why?' But I dream things that never were; and I say, 'Why not?'.

George Bernard Shaw

Acknowledgments

> If I have seen further it is only by standing on the shoulders of giants.
>
> Sir Isaac Newton

I would like to thank Prof. Hans-Joachim Freund for the opportunity to perform this work in his research group in the Department of Chemical Physics at the Fritz Haber Institute.

I gratefully acknowledge my scientific advisor Prof. Thomas Risse for his help and invaluable scientific knowledge. You proposed interesting research directions for me and gave me the freedom to develop my own ideas.

I would like to thank all members of the Magnetic Resonance group for various help and discussions.

There are many people in the Department of Chemical Physics whom I would like to acknowledge for the friendly atmosphere. Special thanks go to

- Zita Hüsges for being an amazing Master student and for the beautiful purple flowers
- Dr. Esther Kieseritzky for being a good officemate, for support, and for introducing me to some aspects of German culture
- Matthias Peter for introducing me to Berlin nightlife, sharing numerous music and theater experiences, discussing literature, and for lots of other things included in the definition of being a good friend
- Elena Primorac for fun times together and invaluable support during difficult moments

- Dr. Aditya Savara for support, advice, and for introducing me to some aspects of American culture
- Anja Seiler for fun times in the cinema, help, and support
- Dr. Shamil Shaikhutdinov and Dr. Alex Bondarchuk for advice
- Philip Schambach for fun times together and support
- Dr. Fernando Stavale for fun times together and discussions
- Dr. John Uhlrich for sharing numerous music, theater, museum, and zoo experiences (holding a huge fish!), appreciating Cheburashka and other clay creatures, and for just being a good friend

I would like to thank the International Max Planck Research School (IMPRS) for financial support, helpful block courses, and numerous opportunities to meet nice people.

I am grateful to Misha Lemeshko for introducing me to the exciting world of science, for support, and for advice.

I am indebted to my bachelor thesis advisor, Prof. Rostislav Vedrinskii, who unfortunately is no longer with us. I think the work presented in this thesis would appear good to him. At least I finally learned how one can grow an oxide film (that was the question I previously failed to answer during the exam).

Many thanks go to my Russian friends who always were proud of me, believed that I could make it, and tolerated my bad mood for ages.

I would like to acknowledge my parents who gave me a good education and my sister who supported and encouraged me in many aspects of my life.

I am grateful to Vladimir for advices, for supporting me and cheering me up during the last stressful part of writing the thesis.

I thank coffee, drum and bass, pumping house, and trance music for helping me every now and then while writing.

If I have forgotten to acknowledge somebody or something above, this is the fault of my bad memory, but thank you nonetheless.

Contents

Chapter 1

Introduction and Motivation

God created the solids, the devil their surfaces.

Wolfgang Pauli

The understanding of surface properties is crucial for a variety of technological applications such as sensor technology, semiconductor device manufacturing, fuel cells development and catalysis. Among these, heterogeneous catalysis has been and still is a central technology in chemical industry. In spite of the importance of heterogeneous catalysis, today's understanding of many catalytic processes at the microscopic level is still poor. In most cases, this is due to the high complexity of the chemical reactions since the amount of parameters influencing them are too large and too involved. To reduce this complexity, model systems for heterogeneous catalysis have been designed. Using this strategy, significant progress has been made in the last few decades toward a better understanding, and surface science has proven to be very important in this respect. This is highlighted by the 2007 Nobel Price in chemistry awarded to Gerhard Ertl for his contribution to the understanding of surface chemistry.

The simplest model for a supported metal catalyst were metal single crystals [53]. These single crystal studies have demonstrated the relevance and utility of using simple single crystal surfaces to mimic more complex catalytic systems [54]. They have also highlighted the need for more complex model systems, in order to grasp important aspects of the industrial catalysts which are not included in models based on metal single crystal surfaces [59]. To this end, model

systems featuring metal clusters supported on single crystalline oxides were developed [20; 63; 41; 24]. Well defined, planar oxide surfaces may be prepared by cleavage of oxide single crystals or, alternatively, the growth of thin oxide films on metallic supports. From an experimental point of view, the latter approach circumvents the drawback of low electrical and thermal conductivity of the bulk oxides often used as supports such as alumina, silica and magnesium oxide. One has to keep in mind that ultrathin films can exhibit special properties [42; 125; 50] mediated by the metal support. Chemical reactions may therefore differ from reactions on bulk oxides.

The ideal stoichiometric MgO(001) surface is considered to be quite inert, but a defect-rich MgO surface shows complex surface chemistry. Apart from extended defects such as steps or dislocation lines, point defects such as impurity atoms or ion vacancies are an important class of defects. Chemically, some defects like vacancies [117] or dislocation lines [82] on oxide surfaces are expected to be able to donate or abstract electrons to/from adsorbed molecules or deposited metal clusters, which is considered an important mechanism to change the electronic and in turn catalytic properties of metal deposits or adsorbates. Even though the importance of surface defects is generally accepted, experimental characterizations of these species and a subsequent analysis of their influence on adsorbed species at the atomic level is scarce. Electron paramagnetic resonance (EPR) spectroscopy has been used for decades to characterize point defects in the bulk and on the surface of powders, due to the paramagnetic nature of some of these sites. With respect to single crystal surfaces, it has been shown that EPR spectroscopy has the necessary sensitivity to detect paramagnetic species in submonolayer coverage even under UHV conditions [110]. Since EPR spectroscopy is exclusively sensitive to paramagnetic species, which are generally minorities on the surface, EPR alone is insufficient to achieve a comprehensive picture of the surface. Thus, EPR spectroscopy should be combined with other techniques such as infrared spectroscopy or tunneling microscopy to address additional properties. The application of EPR spectroscopy to single crystal surfaces allows characterization of paramagnetic surface species in terms of their geometric as well as electronic environment.

This thesis is structured as follows: Chapter 2 reviews the main experimental techniques, namely EPR spectroscopy and infrared spectroscopy. Chapter 3 gives a detailed description of the experimental setup and sample preparation procedures. Chapter 4 describes the first experiments to characterize intrinsic defects in MgO films. In the following studies of paramagnetic point defects created by Mg additive coloring and hydrogen atom adsorption will be presented. In Chapter 5, the reactivity of MgO films will be discussed. The concept of modified reactivity on ultrathin films will be introduced, and the results on the activation of oxygen molecule on ultrathin MgO films will be discussed. Finally, the reactivity of point defects created by electron bombardment with nitrous oxide will be discussed as well.

Chapter 2

Experimental Techniques

In this chapter the two experimental techniques mainly used in this thesis (Electron Paramagnetic Resonance and Infrared Spectroscopy) will be introduced.

2.1 Electron Paramagnetic Resonance Spectroscopy

Electron paramagnetic resonance (EPR), also known as electron spin resonance (ESR), is a powerful technique for examining the environment of unpaired electrons. EPR is based on the process of resonant absorption of radiation by unpaired electrons in the presence of a strong magnetic field. The following chapter will first give an introduction into the theoretical basis of EPR and will conclude with a description of the EPR spectrometer.

2.1.1 Theory

Electrons possess an intrinsic angular momentum called spin. The corresponding magnetic moment of a free electron $\vec{\mu}_s$ is directly proportional and antiparallel with the spin vector $\vec{S}$:

$$\vec{\mu}_s = -\frac{g_e \mu_B}{\hbar} \vec{S}. \tag{2.1}$$

$\mu_B = \frac{e\hbar}{2m_e}$ is the Bohr magneton which expresses the magnetic moment one expects for one unit of quantum mechanical angular momentum, $\hbar$ is the reduced Planck constant ($\hbar = h/2\pi$), m_e the electron mass and g_e is the so-called free electron g-factor. The g-factor is a dimensionless, system-specific quantity that

relates the magnetic moment to the spin angular momentum. For the free electron g_e equals 2.002319 [132]. If a free electron is in an external magnetic field, the interaction can be described by the following Hamilton operator:

$$\mathbf{H} = \frac{g_e \mu_B}{\hbar} \vec{S} \vec{B} \tag{2.2}$$

A particle with spin $\vec{S}$ has $2S+1$ possible orientations with respect to the magnetic field. A single electron has a spin of 1/2, therefore two energy levels exist. The energy difference between these two levels in an external field B_0 (more precisely the magnetic flux density in units of Tesla) is:

$$\Delta E = g_e \mu_B B_0 \quad \text{if} \quad \vec{B} \; = \; (0, 0, B_0). \tag{2.3}$$

The splitting of the energy levels in a magnetic field is called the Zeeman effect [145]. Transitions between these levels are the basis of EPR spectroscopy.

When the unpaired electron is located in a molecule or compound, other angular momenta present in the system have to be taken into account, as they will also interact with the external magnetic field. An electron can have an orbital angular momentum $\vec{L}$ or be close to atoms with a nuclear angular momenta $\vec{I} \neq 0$. This leads to the following Hamiltonian for the interaction [5; 55]:

$$\mathbf{H}_{Zeeman} = \frac{g_e \mu_B}{\hbar} \vec{S} \vec{B} + \frac{\mu_B}{\hbar} \vec{L} \vec{B} + \frac{g_n \mu_n}{\hbar} \vec{I} \vec{B} \tag{2.4}$$

g_n is the nuclear g-factor and μ_n the nuclear magneton with $\mu_n = \frac{e\hbar}{2m_P}$, m_P being the proton mass. As μ_B and μ_n are reciprocally related to the electron and proton mass respectively, the third term in $\mathbf{H}_{Zeeman}$ is about three orders of magnitude smaller than the first one. For this reason the nuclear Zeeman interaction is often neglected as will be done here [55].

The electron spin $\vec{S}$ can also interact with its own orbital angular momentum $\vec{L}$. This is spin-orbit coupling, resulting in:

$$\mathbf{H}_{LS} = \xi(r) \vec{L} \vec{S}, \tag{2.5}$$

where $\xi(r)$ is a spin orbit constant.

The interaction of the electron spin with the nuclear spin is called hyperfine interaction. This interaction can be divided into two parts. One is the dipole-dipole interaction of two magnetic moments:

$$\mathbf{H}_{HF,dipolar} = \frac{g_e \mu_B}{\hbar} \frac{g_n \mu_n}{\hbar} \left(\frac{3(\vec{S}\vec{r})(\vec{I}\vec{r})}{r^5} - \frac{\vec{S}\vec{I}}{r^3} \right) \tag{2.6}$$

For orbitals with s character, the electron has a finite probability to be found at the nucleus, and one more term has to be added. This is called the Fermi contact interaction [38] and is described by:

$$\mathbf{H}_{HF,contact} = \frac{8\pi}{3} \frac{g_e \mu_B}{\hbar} \frac{g_n \mu_n}{\hbar} |\psi(0)|^2 \, \vec{S}\vec{I}, \tag{2.7}$$

where $|\psi(0)|^2$ is the probability to find the electron at the nucleus. The Fermi contact interaction depends on the dot product $\vec{S} \cdot \vec{I}$ and is isotropic in space. The total hyperfine interaction is the sum of the anisotropic and the isotropic part.

$$\mathbf{H}_{\mathrm{HF}} = \mathbf{H}_{HF,dipolar} + \mathbf{H}_{HF,contact}. \tag{2.8}$$

The spin Hamiltonian $\mathbf{H}$ used to describe typical interactions (Zeeman, spin-orbit and hyperfine) that may be present in an atomic framework can be written as follows:

$$\mathbf{H} = \mathbf{H}_{Zeeman} + \mathbf{H}_{LS} + \mathbf{H}_{\mathrm{HF}}. \tag{2.9}$$

First we will combine the three terms describing the interaction between electron spin, orbital angular momentum, and magnetic field such that one characteristic parameter suffices for a complete description. We will use quantum mechanics and apply perturbation theory. This is allowed because the energies involved in the interaction between electron spin, orbital angular momentum, and magnetic field are much smaller than those of the remaining electronic Hamiltonian (e.g. kinetic energy, Coulomb energy). The important aspect in this respect is the so-called "quenching" of the orbital angular momentum. Lets take as an example the p-orbitals of an atom in a molecule. In the molecule, the p-orbitals are subjected to electrostatic forces from the neighboring atoms and the degeneracy of the three atomic p-orbitals is lifted. Lets consider a p_z orbital (Fig. 2.1).

As a non-degenerate single-electron wavefunction it can always be described by a real function [6]. The operator of the orbital angular momentum is purely imaginary. However, as $\vec{L}^2$ is an observable, the expectation value has to be real. These conditions can only be fulfilled if $L = 0$. More generally, whenever the ground state is non-degenerate the orbital angular momentum is 'quenched' with the above meaning.

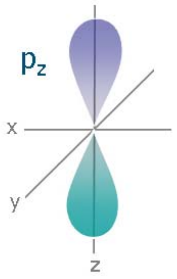

Figure 2.1: Electron density of the p_z orbital.

The eigenstates of the unperturbed Hamiltonian will be denoted by $|n\rangle$ and the corresponding energy eigenvalues by $E_n^{(0)}$. Applying first order perturbation theory, one obtains for every non-degenerate state the correction to the ground-state energy. The correction term is calculated using the expectation value of the perturbing operator applied onto the ground-state wavefunction [81]:

$$\begin{aligned} E_0^{(1)} &= \langle 0|\mathbf{H}'|0\rangle \\ &= \frac{g_e\mu_B}{\hbar}\langle 0|\vec{S}\vec{B}|0\rangle + \frac{\mu_B}{\hbar}\langle 0|\vec{L}\vec{B}|0\rangle + \langle 0|\xi(r)\vec{L}\vec{S}|0\rangle \end{aligned} \tag{2.10}$$

$\vec{S}$ only acts on spin space and $\vec{L}$ on real space. In the case of quantization along the z-direction $E_0^{(1)}$ can then be rearranged to:

$$E_0^{(1)} = \frac{g_e\mu_B}{\hbar}B_z\langle 0|0\rangle S_z + \frac{\mu_B B_z}{\hbar}\langle 0|L_z|0\rangle + \lambda\langle 0|L_z|0\rangle S_z \tag{2.11}$$

Here it was assumed that the ground-state wavefunction can be separated into a radial component and an angular dependent component, then λ is the expectation value of $\xi(r)$ whereas $\vec{L}$ only acts on the angular one. As $L = 0$, the term $\langle 0|L_z|0\rangle$ also has to vanish. Thus, only the first term remains. The according Hamiltonian describing an isotropic interaction between an electron and a magnetic field is given by:

$$\mathbf{H}'^{(1)}_{spin} = \frac{g_e \mu_B}{\hbar} \vec{S}\vec{B} \tag{2.12}$$

Performing perturbation theory to the second order reveals the anisotropy of the g-factor. The second-order energy correction is the following [81]:

$$E_0^{(2)} = -\sum_{n\neq 0} \frac{\langle 0|\mathbf{H}'|n\rangle\langle n|\mathbf{H}'|0\rangle}{E_n^{(0)} - E_0^{(0)}} \tag{2.13}$$

It is again assumed that the wavefunctions are separable into angular and radial components. After insertion of the $\vec{L}$-dependent terms for $\mathbf{H}'$ the following spin Hamiltonian is obtained [55]:

$$\begin{aligned}\mathbf{H}'^{(2)}_{spin} = -2\frac{\mu_B}{\hbar}\lambda \sum_{i,j=x,y,z} \Lambda_{ij} B_i S_j - \lambda^2 \sum_{i,j=x,y,z} \Lambda_{ij} S_i S_j \\ -\frac{\mu_B^2}{\hbar^2} \sum_{i,j=x,y,z} \Lambda_{ij} B_i B_j,\end{aligned} \tag{2.14}$$

with

$$\Lambda_{ij} = \sum_{n\neq 0} \frac{\langle 0|L_i|n\rangle\langle n|L_j|0\rangle}{E_n^{(0)} - E_0^{(0)}} \tag{2.15}$$

The last term describes the diamagnetic interaction. It is small compared to the first term and is generally neglected. The middle term accounts for anisotropic spin-spin interactions that are mediated by spin-orbit coupling. They are intramolecular interactions that are small in nature and vanish for single unpaired electrons [55]. Therefore only the first term remains.

The spin Hamiltonian, including first and second order perturbations without hyperfine interactions, thus reduces to:

$$\begin{aligned}\mathbf{H}_{spin} &= \mathbf{H}^{(1)}_{spin} + \mathbf{H}^{(2)}_{spin} \\ &= \frac{g_e \mu_B}{\hbar}\vec{S}\vec{B} - 2\frac{\mu_B}{\hbar}\lambda \sum_{i,j=x,y,z} \Lambda_{ij} B_i S_j \\ &= \frac{\mu_B}{\hbar} \sum_{i,j=x,y,z} g_{ij} B_i S_j,\end{aligned} \tag{2.16}$$

with

$$g_{ij} = g_e\delta_{ij} - 2\lambda\Lambda_{ij} \tag{2.17}$$

$$\text{with } \delta_{ij} = \begin{cases} 1 & i = j \\ 0 & i \neq j \end{cases} \tag{2.18}$$

As $2\lambda\Lambda_{ij}$ is a 3×3 matrix, this also holds true for g_{ij}, g_{ij} is frequently called the g-matrix. Eq.2.16 can be abbreviated by:

$$\mathbf{H}_{spin} = \frac{\mu_B}{\hbar}\vec{S}\hat{g}\vec{B} \tag{2.19}$$

All operators in Λ_{ij} are hermitian and the result is therefore a symmetric matrix. Thus, the matrix can always be diagonalized by choosing an appropriate coordinate system. The task is to determine the three principal components of the g-matrix and their orientations with respect to the molecular framework. The latter can be greatly simplified by symmetry considerations. The second spectrum in Fig. 2.3 shows the three different absorption lines for an anisotropic g-matrix where each spectrum is obtained by aligning the magnetic field with one of the principal g-axes.

To include the hyperfine interaction, the nuclear-dependent term in eq. 2.9 has to be evaluated. Conducting a derivation similar to the one for the g-matrix it is found that [55]:

$$\mathbf{H}_{HF} = \sum_{i,j}\left(A_{ij}^{anisotrop} + \delta_{ij}a_{iso}\right)S_iI_j = \vec{S}\hat{A}\vec{I} \tag{2.20}$$

The A- and g-matrices have the same properties. Combining the two expressions the spin Hamiltonian is given by:

$$\mathbf{H}_{spin} = \mathbf{H}_{Zeeman} + \mathbf{H}_{HF} = \frac{\mu_B}{\hbar}\vec{S}\hat{g}\vec{B} + \vec{S}\hat{A}\vec{I} \tag{2.21}$$

If there is no hyperfine interaction, eq. 2.21 consists of only the first term. For this case, the energy eigenvalues will be derived below. The magnetic field, $\vec{B}$, is defined in the laboratory frame whereas $\vec{S}$ is defined in the spin coordinate system.

Before the energy eigenvalues can be evaluated, the coordinate systems have to be aligned appropriately. In the language of quantum mechanics: a common set of eigenfunctions for $\mathbf{H}_{spin}$ and S_z has to be found. The magnetic field B_0 is taken to be aligned along the z-direction of the laboratory frame. By an Euler transformation it is rotated into the coordinate system in which the g-matrix is diagonal. The combined system $\widehat{g}\vec{B}_0$ is transformed such that it is aligned along the quantization axis (here the z-axis) by a second Euler transformation. The stationary solutions of the Schrödinger equation then become:

$$E_n^{(0)} = E_{S,\,m_S}^{(0)} = \mu_B g_{eff} B_0 m_s \tag{2.22}$$

with

$$g_{eff} = \sqrt{(g_{xx}^2 \cos^2\phi + g_{yy}^2 \sin^2\phi)\sin^2\vartheta + g_{zz}^2 \cos^2\vartheta} \tag{2.23}$$

ϑ is defined as the polar angle between the static field and g_{zz}, and ϕ is the azimuthal angle in the xy-plane of the g-matrix (between x axis and the projection of the magnetic field on the xy-plane). To incorporate hyperfine coupling in the analysis, the strength of the Zeeman interaction has to be evaluated in comparison with the hyperfine interaction. When the Zeeman interaction is much larger than the hyperfine interaction, the latter can be treated as a perturbation. As this becomes true for high magnetic fields, the application of first order perturbation theory is called the 'high field' approach [5]. Extending the treatment to second order induces shifts in the expected transitions leading to asymmetry in the spectrum [5]. If the electron Zeeman interaction and the hyperfine coupling are of the same order of magnitude the problem can no longer be treated by perturbation theory and a full matrix diagonalization must be performed. This is in most cases done numerically and open source programs like Easyspin are available to solve such problems[124].

We will derive expressions for the transition probability between spin states that allow the determination of the transition selection rules. The static magnetic field itself cannot induce transitions between spin states. Transition between states require an oscillating magnetic field $B(t)$ which is oriented perpendicular to the static field [5]. Usually it is assumed that B_0 is aligned along the z-axis of the

laboratory frame while $B(t)$ is linearly polarized along the x-axis. If the amplitude of $B(t)$ is sufficiently small the problem can be treated by perturbation theory. The perturbing term can be described by a sinusoidal function with angular velocity ω ($B(t) = B_1\vec{e}_x \sin\omega t$). The additional term arising in the Hamiltonian is:

$$\mathbf{H}_{MW} = \mu_B \vec{S}\hat{g}\vec{B}(t) \tag{2.24}$$

Using time-dependent perturbation theory one can derive a transition probability which is time independent for the periodic perturbation [78]:

$$W_{fi} = \frac{2\pi}{\hbar}|\langle f|\mathbf{H}_{MW}|i\rangle|^2\delta(E_f - E_i - h\nu) \tag{2.25}$$

where i represents the initial state and f the final state. The δ-function only differs from zero for $E_f - E_i = h\nu$ and ensures energy conservation. Substituting $\mathbf{H}_{MW}$ by the appropriate expression given in eq. 2.24 and explicitly writing the components of the angular momentum operator gives:

$$W_{fi} = \frac{2\pi\mu_B^2}{\hbar}|B_1|^2|\langle f|c_xS_x + c_yS_y + c_zS_z|i\rangle|^2 \tag{2.26}$$

To extract the selection rules for allowed transitions, it is useful to express the x- and y-components of $\vec{S}$ in terms of raising and lowering operators. The applied static field along z prevents transitions taking place in this direction and the S_z-component can be neglected. The above equation thus transforms to:

$$W_{fi} = \frac{\pi\mu_B^2}{2\hbar}|B_1|^2|\langle f|(c_x - ic_y)S_+ + (c_x + ic_y)S_-|i\rangle|^2 \tag{2.27}$$

Whereas the raising operator S_+ describes the absorption of a photon and the lowering operator S_- relates to the induced photon emission. Both events are equally probable. Therefore, no conclusion about the net absorption of the system can be drawn from the probabilities. To observe absorption during the experiment, a population difference of the spin states, as described for an ensemble of spins at thermal equilibrium by the Boltzmann distribution, has to be present. From eq. 2.27 it follows that the integral is only non-zero when m_s of the initial and

the final state differ by 1; that is $\Delta m_s = \pm 1$. In the case of a single unpaired electron, photon absorption thus takes place for excitations between $m_s = -1/2$ and $m_s = +1/2$. The coefficients c_x and c_y depend on the polar angles ϑ and ϕ. Therefore, also the transition probability containing these parameters depends on the orientation of the static magnetic field, B_0, in the g-matrix framework.

Lets consider the electron in an environment close to a nucleus with $\vec{I} = 1$. Schematically, the energy levels are as depicted in Fig. 2.2. If we do a Gedanken-experiment and orient the magnetic field along the three main axis of g and A matrix (if we assume they have the sme orientation), it will result in different spectra as shown in Fig. 2.3. If the B_0-field is aligned along one axis, three (2I + 1) transitions are expected, one for each state of $\vec{I}$ ($m_I = +1, 0, -1$) with m_s changing by 1. The spacing of the lines is determined by the hyperfine component of the observed orientation. Technical aspects lead to the fact that in most EPR experiments the frequency is kept constant whereas the magnetic field is swept. Obviously the magnetic field value at which the transition occurs depends on the orientation between the molecular coordinate system and the field itself. In the case of disordered samples, such as powders, the spectrum is obtained by integrating over all possible orientations between the molecular coordinate system and the magnetic field. An example of this is shown at the bottom of Fig. 2.3.

Now we will discuss the interaction of an ensemble of paramagnetic species and the magnetic field, as it is observed in an EPR experiment. Putting an ensemble of unpaired electrons into an external magnetic field leads to an alignment of the magnetic dipole moments along the magnetic field and thus a magnetic polarization which is commonly called magnetization ($\vec{M}$). In the case of paramagnetic materials, the magnetization is proportional to the magnetic field strength H_0 and can be expressed as:

$$M = \chi H_0 = \frac{\chi}{\mu_0} B_0 \tag{2.28}$$

The proportionality factor, χ, defined in this equation, is the volume magnetic susceptibility. If N independent particles contribute to M and the Hamiltonian for the system is described by $\mathbf{H} = g\mu_B B_0 S_z$, then the expectation value of the magnetization is related to the microscopic spin S by [5; 45]:

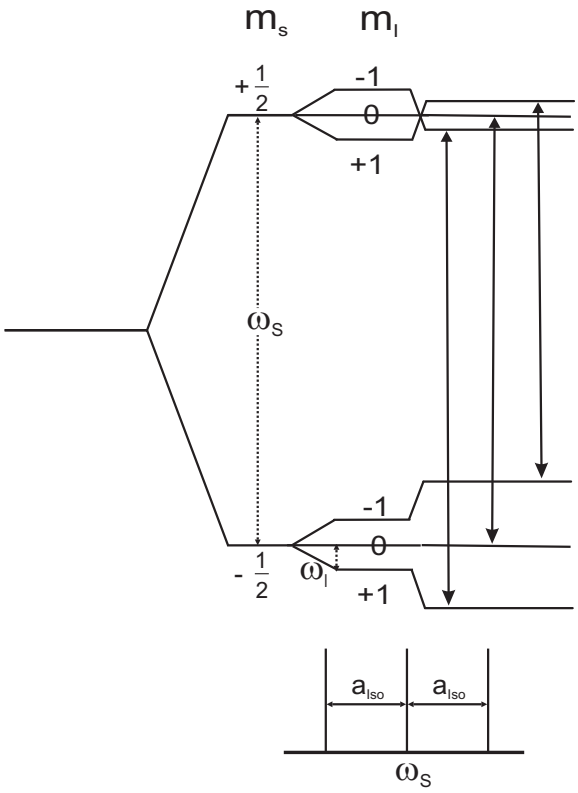

Figure 2.2: The scheme of energy levels of an isotropic spin system with an electron spin S=1/2 and a nuclear spin I=1. Figure is adapted from ref. [71].

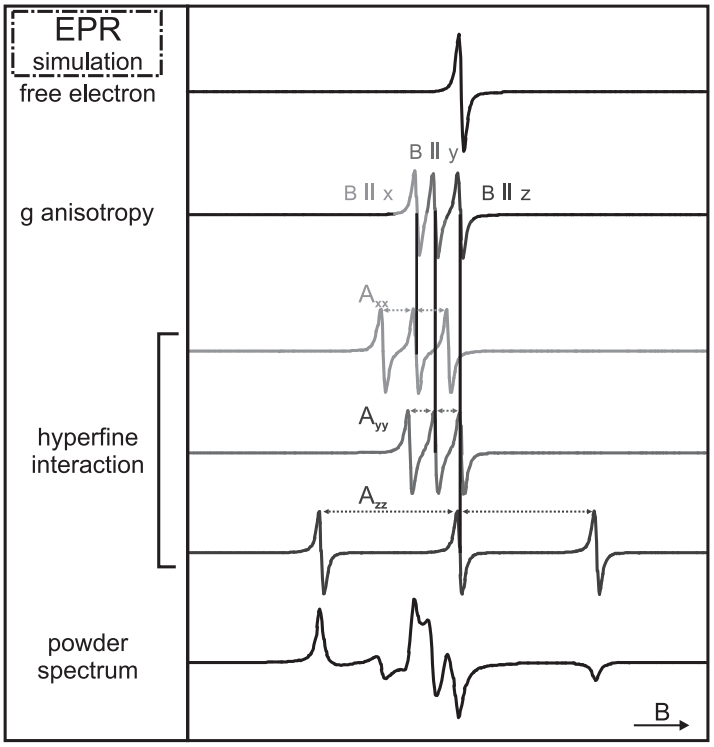

Figure 2.3: Effects of molecular anisotropy on the appearance of the EPR spectrum. Figure is adapted from ref. [70].

$$\langle M \rangle = \frac{N g^2 \mu_B^2 S(S+1) B_0}{3 V_s k T} \tag{2.29}$$

with V_s being the sample volume, k the Boltzmann constant, and T the temperature. Combining eq. 2.28 and eq. 2.29, the magnetic susceptibility relates to the microscopic world by the following equation:

$$\chi = \frac{\mu_0 N g^2 \mu_B^2 S(S+1)}{3 V_s k T} \tag{2.30}$$

The inverse relationship between the susceptibility and temperature is known as Curie's law. The direct scaling of χ with the number of spins as well as the inverse temperature dependence are used in quantitative analysis of signal intensities in EPR.

As excitation in EPR is achieved by an alternating field, the spectrum is not determined by the above mentioned static susceptibility but has to be related to the complex high-frequency susceptibility:

$$\chi_{compl} = \chi' + i\chi'' \tag{2.31}$$

It can be shown that the dissipation of energy is associated with the imaginary part χ'' [5] and is usually the observed quantity in EPR experiments. The proportionality to N/T shown in eq.2.30 also holds true for χ'' [4]. One can decrease the temperature to increase the intensity, but it has a lower limit given by the necessary dissipation of the energy absorbed. This process called relaxation and will be the subject of the next section.

The simplest model to describe relaxation of a spin system in EPR is the Bloch ansatz. Applying a static magnetic field along the z-axis induces – within a classical picture – a precession of the present spins about this axis. The Boltzmann statistics in this case predicts a population difference between the two spin states taking part in the excitation and therefore a magnetization along the z-axis. A change in magnetization along this axis is thereby directly correlated with a change in population difference. The single spin also has a magnetization component in the xy-plane, but there is no phase coherence to the other spins of the ensemble in this plane. Thus, there is no macroscopic magnetization in the

xy-plane. Bloch wanted to describe relaxation by two processes: one is the energy dissipation to get back to the initial population difference, the other the loss in coherence between magnetic field and magnetization. In a classical picture, one can describe the magnetization being in the form of in phase and out of phase. In phase magnetization is coherent with the applied magnetic field, and the out of phase magnetization has a phase shift of $\pi/2$. In his ansatz, both processes are described by an exponential decay. The characteristic time constants appearing in the exponential terms are called T_1 and T_2. T_1 characterizes the exponential recovery of the z-component whereas T_2 describes the exponential drop of phase coherence. In general, the two times are not equal as they are connected to different physical processes. Loss in phase coherence is not necessarily coupled to spin flipping, while transitions between two spin states also lead to phase decoherence. The equations of motion including the relaxation take the following form:

$$\frac{dM_z}{dt} = \gamma(\vec{B} \times \vec{M})_z + \frac{M_0 - M_z}{T_1} \tag{2.32}$$

$$\frac{dM_x}{dt} = \gamma(\vec{B} \times \vec{M})_x - \frac{M_x}{T_2} \tag{2.33}$$

$$\frac{dM_y}{dt} = \gamma(\vec{B} \times \vec{M})_y - \frac{M_y}{T_2} \tag{2.34}$$

with γ being the gyromagnetic ratio $(-g_i\mu_B/\hbar)$. To perform an EPR experiment, a periodic oscillating field with amplitude B_1 is applied (commonly along the x-axis) and has to be added to the equations of motion above. Applying an oscillating field in the plane perpendicular to the static field causes a change in the value of the projection of that magnetic moment in the direction of the static field. Under these conditions the magnetization has a time dependent component perpendicular to the static field and thus can be described by a complex susceptibility. Solving the resulting equations and expressing them in terms of the components of the complex susceptibility leads to [5]:

$$\chi' = \frac{1}{2}\left\{\frac{\gamma M_0(\omega_0 - \omega)}{\gamma^2 B_1^2(T_1/T_2) + (1/T_2)^2 + (\omega_0 - \omega)^2}\right\} \tag{2.35}$$

$$\chi'' = \frac{1}{2}\left\{\frac{\gamma M_0(1/T_2)}{\gamma^2 B_1^2(T_1/T_2) + (1/T_2)^2 + (\omega_0 - \omega)^2}\right\} \tag{2.36}$$

where ω_0 is equal to γB_0. To deduce the lineshape of the absorption signal eq. 2.36 has to be analyzed. Obviously χ'' depends on the incident microwave field, B_1. As the term B_1^2 describes saturation effects, it can be neglected as long as an appropriate incident microwave power is chosen in the EPR experiment. In this case eq. 2.36 reduces to an expression of the well known Lorentzian lineshape. Therefore the EPR spectra of an ensemble of non-interacting spins with a single transition frequency are expected to show Lorentzian line.

So far we discussed independent particles, next we are going to discuss the influence of intermolecular interactions. In the case of diluted samples the effect of intermolecular interactions on the EPR signal is small and in most cases ignored. However, for sufficiently concentrated samples intermolecular interactions (dipolar and exchange) can change the EPR spectrum substantially. Exchange interactions result from orbital overlap and are therefore important only at short distances. If the distance between spins is larger than about 8 Å the dipolar interaction has a greater influence [74].

The spin of an electron is a magnetic dipole whose field acts upon other magnetic moments in its surroundings. Assuming isotropic g-values g_1 and g_2 the dipolar interaction between electrons can directly be written as:

$$\mathbf{H}_{d-d} = \frac{g_1 g_2 \mu_B^2}{\hbar^2} \left(\frac{-3(\vec{S}_1\vec{r})(\vec{S}_2\vec{r})}{r^5} + \frac{\vec{S}_1\vec{S}_2}{r^3} \right) \tag{2.37}$$

In this simple case the dipolar interaction leads to splitting of an EPR line into two lines. The size of the splitting is given by:

$$\text{dipolar splitting} = g_1 g_2 \mu_B^2 (1 - 3cos^2\theta)/r^3 \tag{2.38}$$

with r being the interspin distance and θ the angle between magnetic field and $\vec{r}$. For large separations of the adjacent spins, the splitting is not observed due to the r^{-3} dependence.

In the general case, both centers can have anisotropic g-values. Assuming coincident principal axes for the two g-matrices involved and that the interspin vector is aligned along the z-axis, the Hamiltonian of dipolar interaction can be divided

into two components, an isotropic component and an anisotropic component:

$$\mathbf{H}_{d-d} = -J_{d-d}\vec{S_1}\vec{S_2} + \vec{S_1}\widehat{D}\vec{S_2} \tag{2.39}$$

It has to be emphasized that the isotropic contribution is only significant for systems with large g-anisotropy.

The other interaction that comes into play if two paramagnetic centers are close to each other is the exchange interaction. At large distances the electron orbitals do not interact. However, as the separation is decreased, two energy levels are formed with either an antiparallel bonding orientation of the spins or a parallel antibonding one. The energy separating these two levels is called exchange energy and depends strongly on the distance of the two spins. Assuming that the wavefunctions are negligibly disturbed by this interaction, the exchange will not influence the Zeeman interaction which is generally describe by $\widehat{g}$. In the isotropic case the Hamiltonian describing the exchange interaction is:

$$\mathbf{H}_{ex} = J_{12}(r)\vec{S_1}\vec{S_2} \tag{2.40}$$

Similar to the spin-orbit coupling of a single paramagnetic species that leads to anisotropy in $\widehat{g}$, the exchange interaction of the ground state of one center with the excited states of another center introduces an anisotropic exchange term. This anisotropic exchange term which can – in analogy to the dipolar coupling – be written in the form $\vec{S_1}\widehat{D}_{ex}\vec{S_2}$ is large for systems that have considerable spin-orbit coupling.

Dipolar and exchange interactions were discussed separately here, but both arise from the interaction between two paramagnetic centers and are present at the same time. Which one of the interactions dominates the spectrum depends on the details of the system, the distance between adjacent spins allows already a good estimation of which interaction dominates. In the case of experiments with powders, molecular orientations are distributed randomly with respect to the magnetic field and all possible pair interactions overlap in the spectrum. However, in many cases the spectrum can be interpreted in a simplified way by pair interactions. Two effects that lead to broadening and narrowing of the

observed EPR signal in disordered samples shall be mentioned here. In the solid state, the dipolar interaction leads to a splitting of the EPR line as discussed above. If the only free parameter is the angle between interspin vector and magnetic field, the powder EPR signal results from an integration over the angular distribution. The resulting line shape is called a pake pattern in which the line splitting is still observable. If in addition to the angle, the interspin distance varies in the disordered system, then the resulting EPR signal consists of one broadened line.

The effects of a dominant exchange interaction mostly leads to line narrowing. In the picture of a pairwise interaction leading to spin exchange the isotropic exchange interaction can be properly described by identifying an effective exchange frequency. The exchange interaction then influences the EPR spectrum in disordered samples in the following way: the combined response of electrons that rest at many different positions within a disordered cluster in a short (compared with the relaxation time) time interval is observed. This destroys g-anisotropy as each single electron occupies sites with different g-values during the time interval. Furthermore, if an electron interacts with a statistical distribution of the possible nuclear spin states, then the hyperfine coupling can no longer be observed.

In conclusion, dipolar and exchange interactions can be used to study the interactions of paramagnetic centers. While the first reveals important information on distances and geometrical orientations, the latter additionally allows access to dynamics information.

2.1.2 EPR Spectrometer

For typical magnetic fields in the range of 1 Tesla, the required radiation belongs to the microwave region. The most commonly used EPR spectrometers operate between 9-10 GHz (X-band), which corresponds to a field around 0.35 T for the free electron g-value. Continuous wave experiment are done using a constant frequency and varying the applied magnetic field to fulfill the resonance condition.

A typical cw-EPR system consists of (Fig. 2.4) :

i) a microwave source, supplying monochromatic radiation whose power is controlled by an attenuator between the source and the sample.

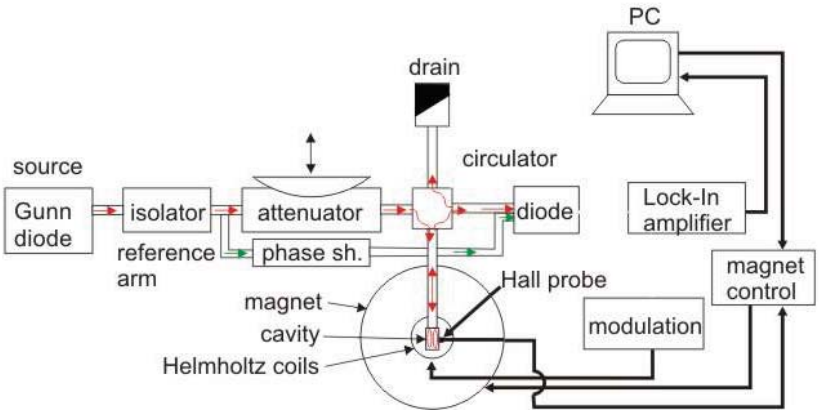

Figure 2.4: Schematics of an EPR experiment. Figure is adapted from ref. [70].

ii) a waveguide system to propagate the microwave radiation from the source to the resonant cavity.

iii) a resonator with a high Q-factor (Fig. 2.5), to take advantage of the enhanced electromagnetic fields in the resonator structure for the excitation of magnetic dipole transitions.

iv) a magnet system capable of providing a homogeneous field across the sample volume.

v) detection, modulation and recording systems.

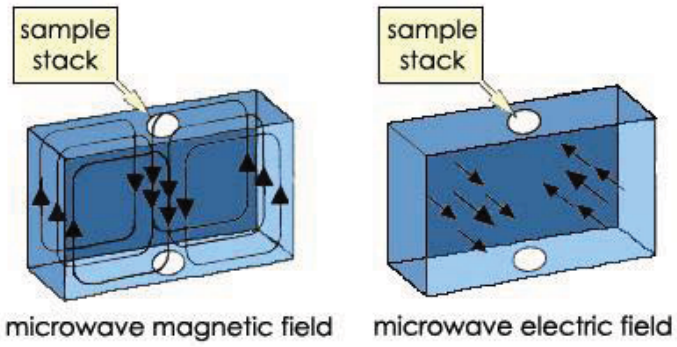

Figure 2.5: Field distribution in a TE_{102} EPR cavity used in our experiments. Adapted from ref. [1]

Microwave source

The main requirement for the microwave source apart from stability is a monochromaticity of the radiation. Nowadays, typical microwave generators are klystrons and solid state generators. In the current experimental setup, a Gunn diode was used. It consists only of n-doped semiconductor material. Three regions exist: two of them are heavily n-doped, with a thin layer of lightly doped material in

between. When a voltage is applied to the device, the electrical gradient will be largest across the thin middle layer. Conduction will take place as in any conductive material with current being proportional to the applied voltage. Eventually, at higher field values, the conductive properties of the middle layer will be altered, increasing its resistivity and reducing the gradient across it, preventing further conduction and current actually starts to fall down. This means a Gunn diode has a region of negative differential resistance. To use a Gunn diode as a stable microwave source, it is put into a suitable resonator in which the resonator determines the output frequency, which must be higher than the Gunn frequency. By proper superposition of direct and alternate voltages, the whole Gunn diode is put in a state of negative differential resistivity which increases the generation of oscillations effectively. The assembly of a Gunn diode and resonator is called a Gunn oscillator. The small variability of the microwave source just described leads to the common practice in EPR experiments of keeping the frequency stable and sweeping the magnetic field. The Gunn effect [58] was first observed by J. B. Gunn and was discovered in GaAs, which is still the most commonly used material in Gunn diodes.

Waveguide

Waveguide is a linear structure that conveys electromagnetic waves between its endpoints. The type of waveguide used here as a transmission line at microwave frequencies is a hollow metal-pipe. Electromagnetic waveguides are analyzed by solving Maxwell's equations with boundary conditions determined by the properties of the materials and their interfaces. These equations have multiple solutions, or modes, which are eigenfunctions of the equation system. Each mode is therefore characterized by an eigenvalue, which corresponds to a cutoff frequency below which the mode cannot exist in the guide. Waveguide propagation modes depend on the operating wavelength, polarization, the shape and size of the guide. The longitudinal mode of a waveguide is a particular standing wave pattern formed by waves confined in the cavity. The transverse modes are classified into different types:

TE modes (Transverse Electric) have no electric field in the direction of propagation.

TM modes (Transverse Magnetic) have no magnetic field in the direction of propagation.

TEM modes (Transverse ElectroMagnetic) have neither electric nor magnetic field in the direction of propagation.

Hybrid modes have both electric and magnetic field components in the direction of propagation.
In the current setup we use a rectangular TE_{10} waveguide.

Resonator

We use a microwave a cavity to amplify weak signals from the sample. A microwave cavity in its simplest form is a metal box with a shape which allows the build up of a standing wave structure inside. Resonance means that the cavity stores the microwave energy. Cavities are characterized by their Q or quality factor, which indicates how efficiently the cavity stores microwave energy. The Q factor is defined as: Q = $(2\pi$(energy stored))/(energy dissipated per cycle), where the energy dissipated per cycle is the amount of energy lost during one cycle. Energy can be lost e.g. due to ohmic losses in the side walls of the cavity because the microwaves generate electrical currents in some of them. We can measure Q factors easily because there is another way of expressing Q: Q = $(\nu_{res})/(\Delta\nu)$, where ν_{res} is the resonant frequency of the cavity and $\Delta\nu$ is the width at half height of the resonance. As Q increases, the sensitivity of the spectrometer increases. But there is an upper limit for the desirable Q factor because of too sharp resonance at high Q values. A consequence of resonance is that there will be a standing wave inside the cavity. Standing electromagnetic waves have their electric and magnetic field components exactly out of phase. The spatial distribution of the amplitudes of the electric and magnetic fields in the TE_{102} EPR cavity used throughout this thesis is shown in Figure 2.5. We can use the spatial separation of the electric and magnetic fields in a cavity to great advantage. Most samples have non-resonant absorption of the microwaves via the electric field (this is how a microwave oven works) and Q will be degraded by an increase in the dissipated energy. It is the magnetic field that drives the absorption in EPR. Therefore, the highest sensitivity is obtained when we place our sample in the electric field minimum and the magnetic field maximum.

Detection, modulation and recording

When the sample absorbs microwave energy, Q is lowered due to the increased losses and the coupling changes because the absorbing sample changes the impedance of the cavity. The cavity is therefore no longer critically coupled (coupling that provides the maximum transfer of signal energy from one resonant circuit to another when both are tuned to the same frequency) and microwaves will be reflected back to the bridge, resulting in an EPR signal. However, the absorbed microwave power is very weak, which renders a direct detection of this absorption difficult. EPR spectroscopy employs a technique known as phase sensitive detection to enhance the sensitivity of the spectrometer by reducing unwanted noise contributions. The detection scheme works as follows. The magnetic field strength which the sample sees is modulated sinusoidally at the modulation frequency. If there is an EPR signal, the field modulation quickly sweeps through part of the signal and the microwaves reflected from the cavity are amplitude modulated at the same frequency with a well known phase. For an EPR signal which is approximately linear over an interval as wide as the modulation amplitude, the EPR signal is transformed into a sine wave with an amplitude proportional to the slope of the signal (See Figure 2.6). The signal channel (more commonly known as a lock-in amplifier or phase sensitive detector) produces a DC signal proportional to the slope of the modulated EPR signal. It compares the modulated signal with a reference signal having the same frequency as the field modulation and it is only sensitive to signals which have the same frequency and phase as the field modulation. Any signals which do not fulfill these requirements (i.e, noise and electrical interference) are suppressed. As a result, the detected signal appears as a first derivative of the adsorption spectrum with respect to the magnetic field. Phase sensitive detection with magnetic field modulation can increase the sensitivity by several orders of magnitude; however, one must be careful in choosing an appropriate modulation amplitude and frequency, to avoid distortion of the EPR signals. A good compromise between signal intensity and signal distortion occurs when the amplitude of the magnetic field modulation is equal to the width of the EPR signal.

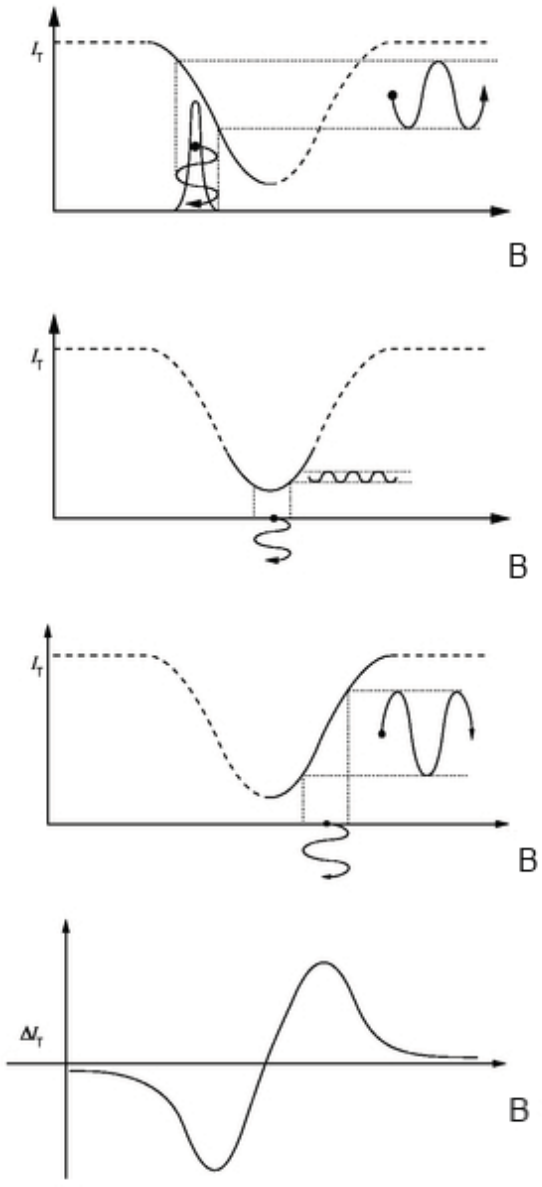

Figure 2.6: Field modulation and phase sensitive detection. Adapted from ref. [1]

2.2 Infrared Reflection Absorption Spectroscopy

Infrared spectroscopy (IR) is the subset of photon based spectroscopies that deals with electric dipole excitations in the infrared region of the electromagnetic spectrum. Infrared radiation has wavenumbers from roughly 13000 to 10 cm^{-1}, or wavelengths from 0.78 to 1000 μm. It not only allows chemical identification of the species but also reveals information about adsorbate-substrate interactions on surfaces as well as intermolecular interactions.

2.2.1 Theory

The excitation of molecular vibrations through interaction with the electromagnetic field can be treated with time dependent perturbation theory [6]. In the case of the incident wavelength being much longer than the dimensions of molecular vibrations the electric dipole approximation can be used. It assumes that the electric field component is a constant at the site of interaction. This is a valid approximation for all infrared frequencies. The perturbing term is the inner product of the electric field vector $\vec{E}$ and the electric dipole operator $\vec{\mu}$

$$\mathbf{H}^{(1)} = -\vec{E} \cdot \vec{\mu}. \tag{2.41}$$

Fermi's golden rule is a way to calculate the transition rate (probability of transition per unit time) from one energy eigenstate of a quantum system into a continuum of energy eigenstates, due to a perturbation. Inserting the perturbing term into Fermi's Golden Rule leads to the following expression for the transition probability in dipöle approximation:

$$W_{i \to f} \propto \left| \vec{E_0} \cdot \langle \Psi_f | \vec{\mu} | \Psi_i \rangle \right|^2 \tag{2.42}$$

Ψ_i and Ψ_f being the initial and final state wavefunctions, respectively. In the harmonic approximation, i.e. when the molecular Hamiltonian corresponding to the electronic ground state can be approximated by a harmonic oscillator in the neighborhood of the equilibrium molecular geometry, the resonant frequencies are determined by the normal modes corresponding to the molecular electronic

ground state potential energy surface. The transition probability is only nonzero if the integrand in eq. 2.42 is totally symmetric. From this fact it can be deduced [6] that a vibrational excitation is only infrared active if the molecular dipole moment changes along the normal coordinate Q_k during the vibration that is

$$(\partial\vec{\mu}/\partial Q_k)_0 \neq 0. \tag{2.43}$$

Only transitions between neighboring vibrational levels (v_n) can occur:

$$\Delta v = \pm 1. \tag{2.44}$$

Infrared spectroscopy was among the first techniques to be applied to the direct characterization of adsorbates [142]. Early studies employed transmission infrared spectroscopy, in which the infrared beam passes through a suitably prepared sample [83; 72]. However, transmission mode is not suitable for the investigations of non transparent metal single crystal substrates. As the transmittance of IR for metals is low, absorption by adsorbates on the surface is usually measured in reflection geometry. This technique is then called infrared reflection absorption spectroscopy (IRAS). In all IR measurements conducted here, the adsorbate is close (less than one micrometer) to a metal surface.

In Fig. 2.7 the decomposition of the electric field component of the incident beam on the metal surface into p- and s-polarized (E_P and E_S) components is shown. As can be deduced from Fresnel equations, the s-component undergoes a phase shift near π for all possible incident angles on a metal surface. Therefore, the incident and reflected beam practically cancel on the surface. The amplitude of the p-polarized vector depends strongly on the incident angle. Interference of incident and reflected light almost doubles the normal to the surface electric field component of E_P near the grazing angle compared to the incoming wave. The parallel to the surface component of E_P of the p-polarized wave is several orders smaller than the normal component and does not contribute to the observed absorption. As there is no parallel component of the electric field on the surface the dynamic dipoles can only interact with the normal electric field component. Angles near grazing incidence are used to maximize $E_{P\perp}$.

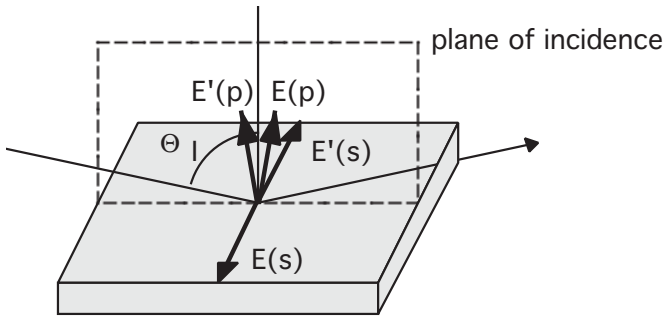

Figure 2.7: Electric vectors of the s- and p-polarized radiation on a metal surface. Primed and unprimed vectors refer to reflected and incident rays, respectively. Figure is adapted from ref. [71].

This interaction between electromagnetic wave and the metal surface can also be understood in a dipole picture. The oscillating dipole moment of the electromagnetic wave creates a corresponding image dipole in the metal surface. The dipole component perpendicular to the surface is amplified by its image dipole whereas the parallel components are canceled as seen in (Fig. 2.8). Thus, only the perpendicular component of the electromagnetic wave contributes to the vibrational excitation. This dipole picture is also useful for analysis of the adsorbate-metal interaction. A vibrating molecule adsorbed on a metal surface induces a corresponding image dipole in the latter. Amplification and cancellation are equivalent to the light-metal interaction as depicted in (Fig. 2.8). Again – this time for the molecule – only the dipole component perpendicular to the surface remains. In conclusion, the electrodynamic properties of metals lead to the metal surface selection rule that states that only species with a dipole moment perpendicular to the surface can be detected and that the incident light needs to have a *p*-component in order to do so (e.g.[64; 66; 56]). This is also valid for an oxide film on a metal surface as long as the film thickness is small compared to the IR wavelength [64].

The interaction between adsorbate and substrate as well as within the adsorbate layer usually leads to a frequency shift compared to the gas phase value.

Frequency shifts of the molecule induced by interaction with the substrate are:

1. mechanical renormalization: The coupling of the molecule to the (rigid) substrate leads to a blueshift that can be understood by using a simple model of masses and springs.

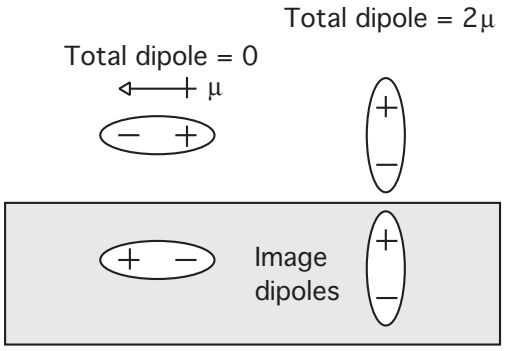

Figure 2.8: Surface dipole selection rule. Figure is adapted from ref. [71].

2. the interaction of the dynamic dipole with its image dipole: The dynamic dipole moment induces an image dipole which in turn changes the local electric field of the molecule. This shifts the gas phase value downward to lower frequencies.

3. chemical and electrostatic effects: This includes changes in the electronic structure induced by chemical bonding between adsorbate and substrate as well as charge redistribution due to electrostatic interaction.

Frequency shifts induced by interaction within the adsorbate layer are:

1. dipole-dipole interaction: The direct coupling of neighboring dipoles as well as through-metal coupling interactions between adsorbed molecules shifts the frequency upward.

2. chemical and electrostatic effects: The presence of neighboring molecules can change the electronic structure of the molecule considered as well as the substrate and thereby influence the interaction between them.

As the dipole-dipole interaction is only strong for molecules with similar vibrational frequencies, the last two effects can be differentiated by isotopic mixture experiments.

The coupling of neighboring dipoles not only influences their frequencies but also the observed intensities. With increasing coverage, the interaction between the molecules gets stronger and leads to depolarization. While at low coverage the intensity of the absorption band grows linearly with increasing coverage, the depolarization for higher coverages typically reduces or even inverts the intensity

growth [64]. Furthermore, the intensities are strongly dependent on the geometric orientation of the molecules and their dynamic dipole moment due to the metal surface selection rule. An additional effect which can be observed if two different species with similar vibrational frequencies are present is 'intensity borrowing' [65]. By dipole coupling, the absorption intensity of the lower frequency band is partially transferred to the higher frequency. This effect can be substantial and may lead to a larger intensity for minority species. This renders a quantitative analysis of IR data difficult.

2.2.2 Infrared Spectrometer

Technically the IR spectra are measured using a Fourier transform spectrometer. The main component of such a spectrometer is a Michelson interferometer (Fig. 2.9) which consists of a moving mirror, a fixed mirror, and a beamsplitter positioned at an angle of 45 degrees with respect to these mirrors. Radiation from the broadband IR source (a globar) is collimated and directed into the interferometer, and impinges on the beamsplitter. The beamsplitter, divides the IR beam into two portions. One half is transmitted to the fixed mirror and the other half is reflected to the moving mirror. After reflection at the respective mirrors the two beams are recombined at the beamsplitter. The resulting beam then passes through or is reflected at the sample and is focused on the detector, which is a nitrogen cooled MCT detector in this particular setup. The detector signal is recorded as an interference pattern of the measured signal intensity with respect to the position of the movable mirror (determined by a HeNe-laser). The displacement, x, of the movable mirror determines the path difference: $s = 2x$ (in case of central symmetric displacement). The detected quantity is the total IR intensity as a function of the path difference. At zero path difference all wavelenghts interfere constructively. This leads to the center burst in (Fig. 2.10 a). For a path difference $\neq 0$ some wavelengths can interfere constructively while others undergo destructive interference therefore the measured intensity is smaller than for $x = 0$. In an ideal experiment the interferogram in (Fig. 2.10 a) would be symmetric. However, the measured interferogram is usually asymmetric due to phase shifts introduced by electrical and optical disturbances and the phase has

to be corrected for it. To transform the intensity as a function of path difference into a function of the wavenumber a discrete Fourier transform is applied. The result is a so-called single channel spectrum shown in Fig. 2.10 b. The intensity distributions of the single channel spectrum are mainly caused by the experimental setup including the emission function of the source, properties of optical elements used, reflectivity of the sample, and spectral characteristics of the detector. For this reason a single channel background spectrum, usually the adsorbate free surface, is measured. Subtraction of the two single channel spectra results in a transmittance spectrum that is independent of the parameters used (Fig. 2.10 c).

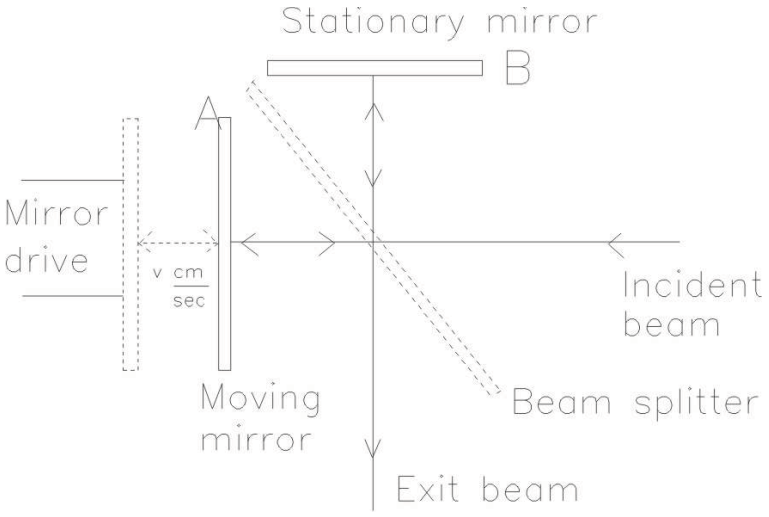

Figure 2.9: Schematics of a Michelson interferometer.

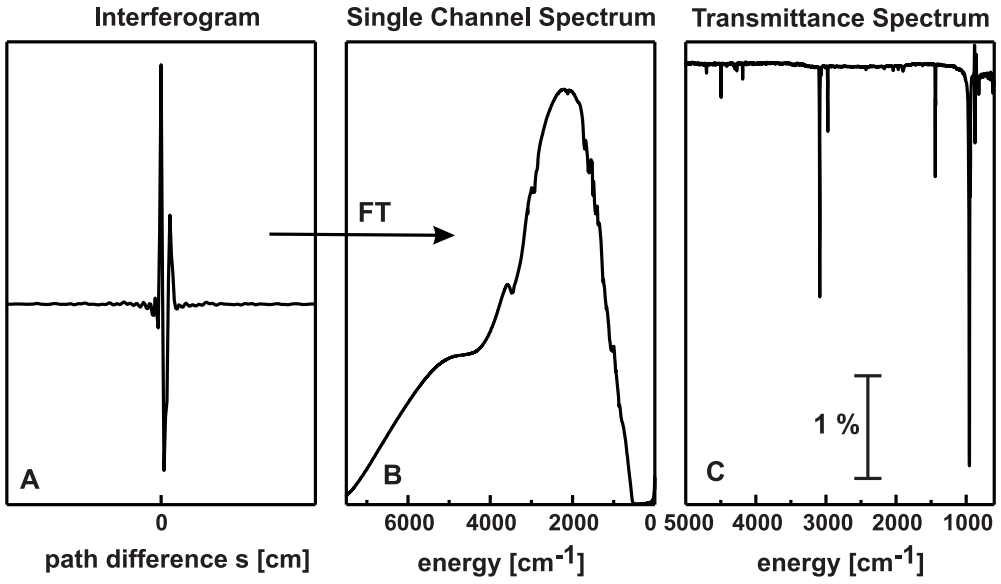

Figure 2.10: a) interferogram b) single chanel spectrum c) transmittance spectrum. Figure is adapted from ref. [71].

Chapter 3

Experimental Details

3.1 Experimental Setup

Studies of clean surfaces demand Ultra High Vacuum (UHV) pressures in the range of 10^{-8} Pascal (10^{-10} mbar). UHV requires the use of special materials in creating the vacuum system and extreme cleanliness to maintain it. The mean free path of a gas molecule at 10^{-9} mbar is approximately 40 km, so gas molecules will collide with the chamber walls many times before colliding with each other. Thus, almost all interactions take place on various surfaces in the chamber.

The experiments have been performed in an ultrahigh vacuum apparatus [111] with a base pressure of 2×10^{-10} mbar shown schematically in Fig. 3.1. The chamber is pumped with an ion-getter, a turbo-molecular and a titanium sublimation pump. The apparatus combines a preparation stage located in the upper chamber, which is equipped with a LEED/Auger system, a mass spectrometer for TPD experiments and for residual gas analysis, as well as evaporation sources and a quartz microbalance for the preparation of the sample. In addition, the apparatus allows for infrared spectroscopic characterization using grazing incidence reflection absorption IR (IRAS) (middle part) and EPR spectroscopic investigations at the bottom of the chamber. The long travel manipulator allows manipulation of the sample inside the chamber in the X, Y, and Z directions, as well as a rotation around the long axis. The sample is attached at the end of a helium cryostat which is mounted inside the manipulator and allows cooling of the sample down to approximately 40 K.

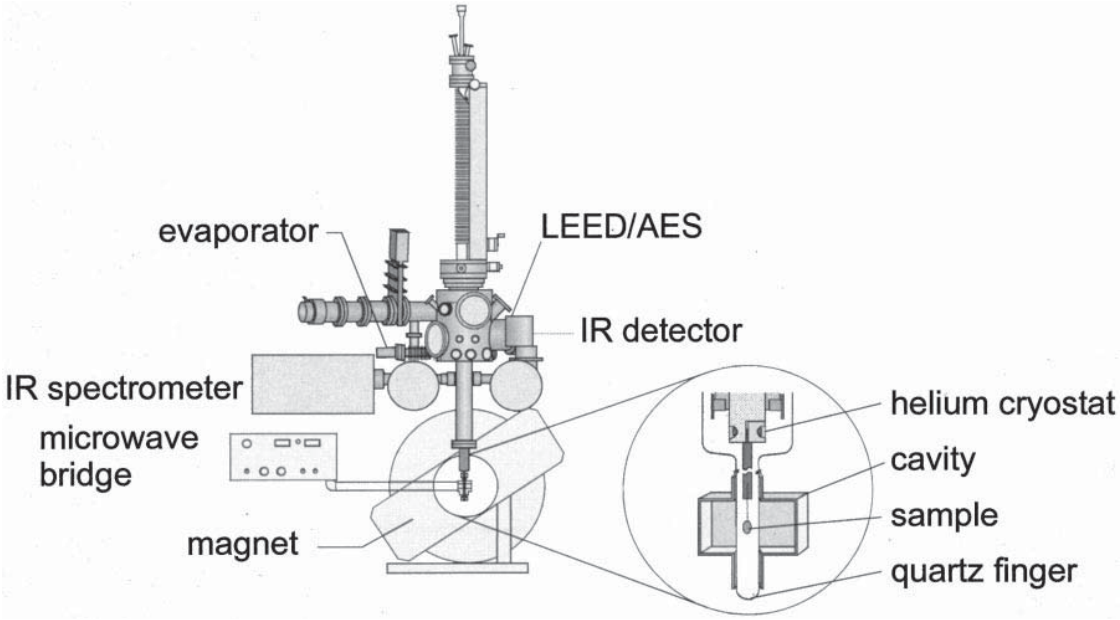

Figure 3.1: Schematics of the experimental setup (adapted from ref. [111])

The sample itself consists of a cut and polished Mo(100) single crystal serving as the substrate for the MgO(100) film preparation. The crystal is held by a loop made of 0.3 mm molybdenum wire sitting in grooves on three sides of the crystal. The loop is mounted on tungsten rods (Fig. 3.2). The tungsten rods are pushed into a sapphire block which is attached to the primary heat exchanger of the helium cryostat. The sapphire block is implemented for electrical isolation of the sample from the cryostat. The sample can be heated directly by passing current trough the molybdenum loop or by electron impact. A W/Re (5% and 26% Re) thermocouple spot welded to the top edge of the crystal is used to measure the temperature of the substrate. The sample can be heated up to 1100 K via direct heating and up to 2300 K using an electron beam from an external filament. The pressure is in the low 10^{-9} mbar range when the sample is at 2300 K.

With the manipulator, the sample can be transferred to an intermediate position to perform IRAS measurements. A BIO-RAD type FTS-40 VM FTIR spectrometer extended by home made optics allows for grazing incident reflection measurements. The spectrometer is evacuated by a rotary pump to avoid gas phase absorption by CO_2 and water. During the measurement, dry nitrogen flows through the spectrometer, serving as a gas cushion for the movable mirror of the Michelson interferometer. The coupling of the spectrometer to the vacuum

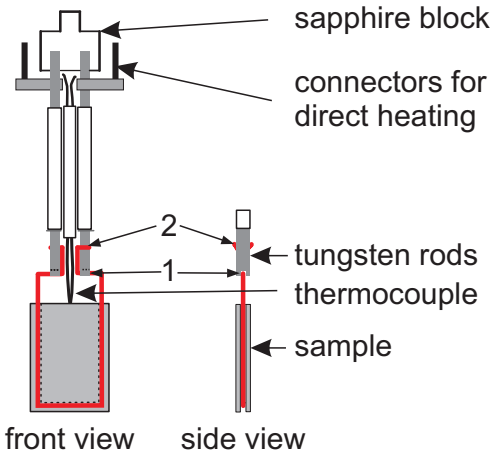

Figure 3.2: Sample setup. Figure is adapted from ref. [107].

chamber is realized via two Viton sealed KBr windows which allow for measurements in the low 10^{-10} mbar range. The reflected infrared radiation is measured by a mercury cadmium telluride (MCT) detector, which is liquid nitrogen cooled. For the IRAS experiments, CO was used as a probe molecule and the sample was exposed at low temperatures (typically 30 K) to different amounts of CO up to saturation coverage. The IRAS spectra were recorded with 4 cm^{-1} resolution. For each spectrum one thousand scans were accumulated and recorded at 30 K if not stated otherwise. Background spectra were recorded using the same settings. For the IR measurements, high purity CO was passed through a liquid nitrogen trap for further purification prior to its introduction into the vacuum chamber.

From the intermediate IR position, the sample may be moved into the EPR stage after passing through a metal-glass connection. This ends in a quartz tube which sits in the bore of an EPR cavity (type TE_{102} from Bruker (Fig. 3.3)). The cavity is part of a Bruker EMX spectrometer equipped with a high-current 12" Varian electromagnet to create the static magnetic field. The magnet can be moved in and out of the measurement position on rails to allow adjustment of the sample and cavity. For EPR measurements radiation in the X-band ranging between 9-10 GHz is used. The incident microwave power used in the experiments was chosen to avoid saturation effects. The EPR spectra were recorded with a modulation amplitude of 4 G. Typically EPR spectra were taken at 30 K and 100 scans were accumulated to obtain a reasonable signal to noise ratio.

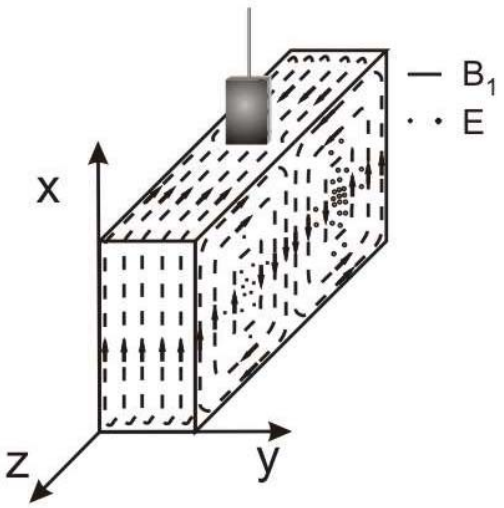

Figure 3.3: Schematics of the crystal in the TE_{102} cavity. Figure is adapted from ref. [107].

3.2 Sample preparation

The crystal cleaning and MgO film growth was done in upper chamber. Thin MgO films were grown on Mo(100) surfaces using established procedures [141]. The Mo substrate was cleaned by cycles of oxidation with O_2 at 1500 K and a pressure of 1×10^{-6} mbar followed by subsequent flashes to 2300 K in UHV. The MgO(100) films were prepared by evaporation of Mg in a background pressure of oxygen (1×10^{-6} mbar) onto the clean Mo(100) substrate. The temperature at which the substrate was held was 300 K or 600 K, and the influence of this parameter will be discussed in this thesis. Mg was evaporated from a carbon crucible using a commercial electron beam evaporator (Omicron EFM3). The sample was biased to the voltage of the evaporant during metal deposition to avoid acceleration of metal ions onto the surface. The deposition rate was 1 monolayer (ML) MgO/min. The thickness of the film was controlled by a quartz microbalance.

To create surface color centers, MgO films were bombarded with electrons of 100 eV energy extracted from a filament at room temperature. The time of exposure and emission current at fixed energy were chosen to get a nominal electron dosage of 1200 electrons per surface oxygen ion (e^-/O^{2-}). This dosage was found to be optimal to maximize the amount of color centers [121; 116]. Hydrogen atoms were produced by the well established process of H_2 thermal

cracking by a hot filament [79; 80]. For experiments, we used hydrogen from Linde (99,9999 Vol % purity) and deuterium from CAMPRO Scientific (99,8 Atom % purity). The nominal exposure of hydrogen was 30 Langmuir (one Langmuir corresponds to an exposure of 1×10^{-6} torr during one second). For reactivity experiments we used N_2O from Linde (99,0 Vol % purity) and O_2 from Linde (99,9996 Vol % purity). The nominal exposures of these gases was 20 Langmuir if not stated otherwise.

Chapter 4

Defects on MgO(001)/Mo(001) films

4.1 MgO: general aspects

Magnesium oxide is an ionic oxide with insulating properties. It crystallizes in the rocksalt structure (Fig. 4.1) with a lattice constant of 421 pm. Simplicity of the structure as well as the highly ionic character renders easier experimental and theoretical analysis, relative to more complex oxides. In heterogeneous catalysis MgO is used as a support for catalytic particles and clusters as well as bare oxide [86; 16; 146]. The development of knowledge about insulating oxide surfaces benefited from the possibility to grow thin films on metal substrates. From an experimental point of view, film growth circumvents the drawback of low electrical and thermal conductivity of bulk oxides, which complicates the application of techniques using charged particles as information carriers such as photoemission or STM. Although one has to pay attention to the fact that some properties of the film may be different from bulk oxides and may depend upon the details of the film growth. For example, film thickness has been recognized as an important parameter to tune properties of thin films as well as properties of adsorbates [42; 125; 50]. The importance of film thickness for the adsorption properties of MgO films will be discussed in this thesis. MgO can be prepared as a thin film on different substrates. Stoichiometry, structure and morphology have been investigated for MgO films grown on Ag(001) e.g. [109; 116; 44],

Fe(001) [89; 73] and Mo(001) [141; 121]. There are various reasons to choose a substrate for a film growth. An important parameter influencing the epitaxial growth of a film onto a substrate is the lattice mismatch. It is defined as $m = (a_f - a_s)/a_s$, with a_f and a_s being the film and substrate lattice parameters, respectively. In the case of MgO (001) and molybdenum (001), it is -5.4%, which is quite large compared with silver (001) (+2.9%) [141]. One also has to note the different sign, which means that in the case of Mo the film experiences tensile stress, and in case of Ag substrate compressive stress. The larger lattice mismatch on molybdenum leads to stronger distortions in MgO layers. Despite this complication the Mo substrate is the most facile one for the EPR experiments planned within this thesis. Fe is out of range due to its ferromagnetic properties, while Ag suffers from th fact that it cannot be efficiently mounted for the EPR experiments. This results in a lowest obtainable temperature of 100 K which renders various experiments impossible. Initial studies on thin MgO films on Mo(001) studies [141] by the means of LEED, Auger electron spectroscopy (AES), temperature programmed desorption (TPD) and high-resolution electron energy-loss spectroscopy (HREELS) have shown that in spite of the 5.4% lattice mismatch between MgO(001) and Mo(001), an ordered stoichiometric MgO film can be formed on the substrate with its (001) face parallel to the (001) face of Mo (Fig. 4.2), where the [100] direction of MgO is rotated by 45° with respect to the [100] direction of the Mo(001) surface. The morphological changes have been investigated in detail for MgO films grown on molybdenum at room temperature after post-annealing them to about 1100 K [10; 11]. These studies show that a regular array of interfacial misfit dislocations forms to release the strain [10]. This results in tilting of the MgO planes, which is visualized by a complex spot structure in LEED. Observation of the simple 1×1 structure expected for MgO indicates flattening of the surface which happens with increasing thickness. This is accompanied by the formation of screw dislocations to compensate the remaining strain [10; 11]. Depending on the literature, flattening of the films is described to occur between 7 and 15 ML. However, the LEED pattern can be used to ensure that experiments are performed on rather flat films. Increased crystallinity is reflected by sharpening of the LEED spots. In this thesis, 20 ML thick films

were used (unless stated otherwise) to ensure that they were flat.

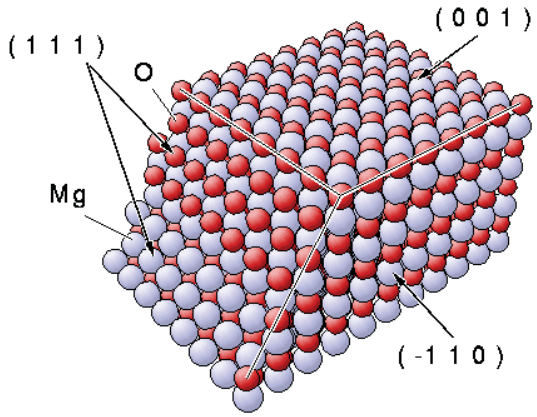

Figure 4.1: Magnesium oxide structure. Adapted from ref. [2].

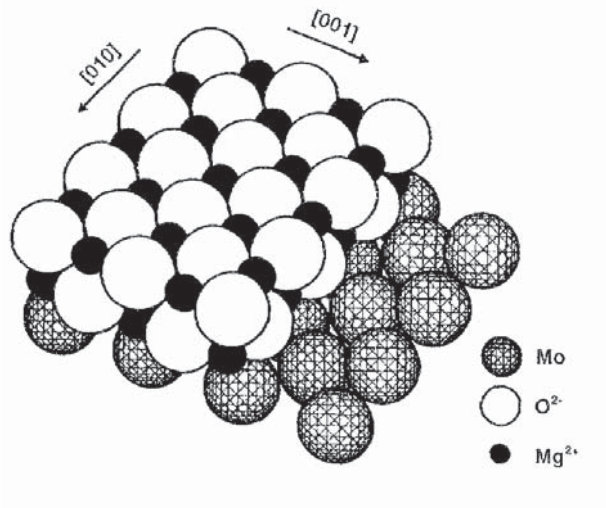

Figure 4.2: Magnesium oxide (001) on a molybdenum (001) substrate. Adapted from ref. [141].

Very often, the chemical and physical properties of solid materials are not controlled by the ideal terraces, but by structural defects (Fig. 4.1). The stoichiomtric (001) surface of bulk MgO is quite inert while the defect rich MgO surface shows a complex surface chemistry [115; 98]. Apart from extended defects such as steps or dislocation lines, point defects are an important class of defects. These point defects can influence optical, electronic and transport properties of the materials [131].

The most important classes of point defects present on MgO surfaces are the following [98; 97]:

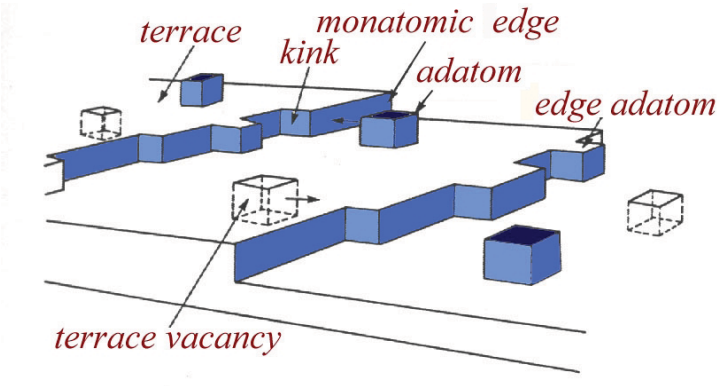

Figure 4.3: Simple defects, which are often found on a low-index crystal faces. Adapted from ref. [3].

- Low coordinated cations. These are Mg^{2+} ions with a coordination number lower than five, found on the flat (001) surface (fourfold-coordinated ions located on steps and threefold-coordinated ions located at kinks and corners)

- Low coordinated anions. These are O^{2-} ions with a coordination number lower than five (fourfold-coordinated ions located on steps and threefold coordinated ions located at corners and kinks)

- Divacancies. These defects are created by removing a neutral MgO unit, therefore their presence does not modify the surface stoichiometry, and they are diamagnetic [9]. Although divacancies can trap electrons and become paramagnetic.

- Oxygen vacancies commonly called color centers or F centers from the German word Farbe for color. The reason for this nomenclature comes from the adsorption of light in the visible region giving color to the oxide. On magnesium oxide, F-centers can exist in three electronic states, depending on the charge present in the vacancy [40]. Diamagnetic oxygen vacancies can be either neutral, F^0, or doubly charged F^{2+}, with respect to the stoichiometric lattice, thus having two or no electrons trapped in the cavity, respectively. The formal removal of an O^- ion results in a F^+ center with one electron, trapped in the cavity. F^+ centers are paramagnetic. In the case of a simple cubic lattice of a highly ionic oxide, the charge state is sufficient to describe the isolated anion vacancies in the bulk. On the sur-

face the situation is more complex, because the surface analogous (usually designated with the subscript s) may exist not only on perfect terrace sites but also at structural defects present on every surface such as steps, corners, or kinks. Energetically the latter are strongly preferred as compared to the ideal terrace sites and calculation suggest that diffusion from the terrace to low coordinated sites has to be expected [21].

- Cation vacancies. Cation vacancies are related to the removal of Mg, Mg^+, or Mg^{2+} species resulting in V^0, V^- and V^{2-} defects. The V^- centers are paramagnetic. In cases of V^- and V^{2-}, the electrons are localised on neighboring O atoms [39].

- Impurity atoms. A prominent case in which the chemistry of a point defect is believed to be decisive for the reaction, is the oxidative coupling of methane by Li-doped MgO [86], where highly reactive O^- ions are created by substitution of divalent Mg^{2+} ions by monovalent Li^+ [86]. The O^- ion is a paramagnetic center. Within this thesis, O^- ion will be studied, but will be created by different methods.

The study of bulk point defects in MgO and other alkaline earth oxides has been quite comprehensive in the past, see e.g. Refs. [136; 137; 95; 62]. Substantial effort was made to reveal the nature and properties of the surface F_s centers [137; 62; 144; 49; 48; 129; 94; 130; 93; 127; 113]. In particular, paramagnetic F_s^+ centers containing single electrons were studied in great detail, e.g by electron paramagnetic resonance (EPR) spectroscopy. The F_s centers were generated by different techniques, namely UV irradiation in the presence of adsorbed H_2 [129; 94; 130; 93; 127], exposure of the oxide to H atoms [113], irradiation [137; 62], and additive coloring with metal vapors having low ionization energy [144; 49; 48]. Depending on the preparation method, neutral F_s^0 and/or paramagnetic F_s^+ centers are formed. In the case of hydrogen treatment, so-called F_s^+(H) centers are created, which consist of electrons trapped at morphological defects (e.g. reversed corners) stabilized by protons close by. The nomenclature of these centers is not rigorous with respect to the definition mentioned above, because it refers to a trapped electron rather than an anion vacancy as clas-

sically meant by the term F-center. However, we will adopt this nomecature to simplify referral to the literature. Due to their electronic properties, surface F-centers often react readily with adsorbed molecules [128; 23; 25; 47]. A strategy to avoid the undesirable reactivity and gain more insight into geometric and electronic properties of surface color centers is the use of well defined single crystal surfaces under ultrahigh vacuum conditions. Along the same line, it is also expected that metal particles nucleated at such F-centers can have altered properties which in turn may alter their catalytic properties. The former effect was recently demonstrated showing that the nucleation of Au clusters at surface color centers leads to a charge transfer from the color centers onto Au clusters, thus, becoming negatively charged [117]. Experimental studies to characterize point defects at the atomic level are rather scarce. Recently, EPR, atomic force microscopy (AFM) and scanning tunneling microscopy (STM) studies have shown that F_s^+ centers as well as F_s^0 centers, generated by electron bombardment of single-crystalline MgO(001) thin films, are located on edges and corners of the MgO(001) islands [121; 116; 75]. AFM studies on thin MgO films have provided evidence that upon electron bombardment F_s^{2+} centers and negatively charged divacancies are also generated [75]. Within this thesis, two new ways of color center production on MgO(001) film surface will be discussed, namely Mg additive coloring and hydrogen atoms deposition. However, before looking into the properties of surface defects, we will discuss the intrinscic defects of the film originating from its growth on a molybdenum substrate. One might expect an increase in defect concentration due to the stress induced by the growth process at room temperature. Stress induced defects will be discussed from an EPR point of view within this thesis. Growing films at elevated temperatures might help to overcome stress induced defect formation, but can cause other problems, which will be discussed as well.

4.2 Paramagnetic defects in room-temperature grown thin MgO films

4.2.1 Results and Discussion

In Fig. 4.4 (lower spectrum) the EPR spectrum of a 20 ML thick MgO film prepared at 300 K is reported. A single symmetric EPR resonance line around the free electron g-value (g_e = 2.0023) is observed. The linewidth of the signal is 5.5 Gauss at 50 K, which remains constant within a temperature range of 50-300 K, while the intensity obeys Curie's law. These paramagnetic centers detected by EPR are located within the bulk of the MgO film, as it is impossible to quench the EPR signal upon adsorption of molecular oxygen at 50 K as observed for surface species due to line broadening induced by physisorbed molecular oxygen. The signal does not change with film thickness. The same spectrum in terms of resonance position, line shape, and intensity has been detected for 10, 20 and 40 ML thick films. The fact that the amount of species is not scaling with the thickness of the film points to the fact that species are not homogeneously distributed in the film. Growing a MgO film at 300 K on a preexisting 20 ML thick film grown at 600 K, which lacks the line around g = 2.0023 (it will be shown in the next chapter), results in the appearance of the same signal. Therefore there is evidence that the signal does not originate from the interface between Mo and MgO. Based on these data, the possible assumption is that paramagnetic centers are located in the subsurface region. To estimate the number of paramagnetic species, the signal obtained here was compared to spectra measured for Au atoms deposited at low temperatures [143]. Based on the correlation with the Au spectra, the amount of spins can be estimated to be $5\pm2 \times 10^{12}$. Qualitatively, this corresponds to submonolayer quantities of paramagnetic species.

To obtain information about the location of trapped electrons, angular-dependent EPR measurements were performed. On single crystals, an angle between the magnetic field and surface crystallographic directions may be chosen which may allow determination of not only the g-matrix anisotropy of the paramagnetic center, but also its orientation. To extract g-matrix anisotropy in the surface plane we performed experiments with the magnetic field lying in the surface plane.

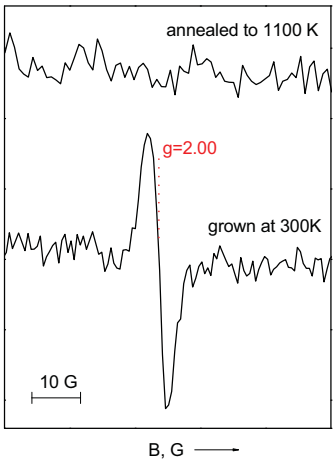

Figure 4.4: EPR spectra of a 20 ML MgO(001) film as prepared at 300 K (lower spectrum) and after annealing to 1100 K (upper spectrum).

Spectra taken for the magnetic field parallel to the [100] direction and [110] direction of MgO exhibit no change in lineshape or resonance position. This means that the g-matrix anisotropy for the system in the surface plane is small compared to the linewidth at this frequency. One has to mention that the intensity of these lines is around 40% smaller than for one line observed for the other orientation. Such an intensity was constantly found for this experimental setup and is attributed to experimental imperfections. The out of plane anisotropy of the g-matrix was probed by EPR varying the angle between the surface normal and the magnetic field. No changes in lineshape or resonance position were observed for the angles between the surface and magnetic field from 0 to 90°. Therefore, g-matrix anisotropy for the system must be small as compared to the linewidth at this frequency.

A rational strategy to get more insight into the location of the trapped electrons is to probe their interaction with oxygen ions of the surroundings. To this end, isotope labeling experiments with $^{17}O_2$ were performed. Based on the crystal structure, we would expect that unpaired electrons of the paramagnetic centers would interact with more than one oxygen ion. The probability of finding m $^{17}O^{2-}$ nuclei in a given array of n equivalent O^{2-} ions can be calculated using the following formula:

$$P_n(m) = \binom{n}{m} p^{n-m} q^m \tag{4.1}$$

where q is the mole fraction of ^{17}O, p is $(1-q)$, and $\binom{n}{m}$ the binomial coefficient. In Fig. 4.5 the probabilities for edge (n=4) and bulk (n=6) are shown. The MgO film was grown with 20% enrichment of $^{17}O_2$. The ^{17}O enrichment was chosen to maximize (40 - 35 %) the probability $P_n(1)$ of having one $^{17}O^{2-}$ anion ($m = 1$) in a given array of $n = 3, 4, 5, 6$ (corner, kink, edge, terrace and bulk) of surrounding ions. The corresponding probability $P_n(2)$ of having two $^{17}O^{2-}$ ($m = 2$) is lower (12 - 20 %), while the probability of having no $^{17}O^{2-}$ $P_n(0)$ ($m = 0$) ranges between 40 - 25 %. In the simplest scenario of coupling to 4-6 equivalent oxygen atoms, one would expect to observe two predominant features: a sextet of lines due to interaction with one ^{17}O (nuclear spin I = 5/2) and an unperturbed central line for centers having a pure ^{16}O environment. The intensities of these lines would be correspondingly ($P_n(1) \times$ intensity of original line)/6 for one line of the sextet and $P_n(0) \times$intensity of original line, respectively (Fig. 4.6). In the present experiment we observed only the central line with 40 % of its original intensity, same linewidth and no additional features in a broad field range (Fig. 4.7). In Fig. 4.7 the ^{17}O enriched film is shown together with the spectrum for a film grown with 100 % ^{16}O. This experiment allows us to draw several conclusions. We observed the central line with about 40 % of the original intensity, which means that it is well in line with our expectation for 4-6 oxygen atoms surrounding the unpaired electron. With the given mole fraction of ^{17}O atoms in the system, this signal corresponds to the unpaired electron in a purely ^{16}O environment. The fact that the lineshape of the central signal is not changed indicates that the hyperfine constant with ^{17}O is bigger than 1 G, otherwise we would have observed a broadening of the line due to the overlap with the sextet of lines. Most likely we do not observe the spectral features arising from interaction of unpaired electron with ^{17}O because there are several inequivalent sites. Therefore, the intensity is distributed between several sextets of lines with different hyperfine coupling constants which makes it impossible to be observed experimentally.

Annealing of the film to various temperatures in the interval 300-1100 K leads to a decrease of the signal intensity (Fig. 4.8) without a change of signal position or lineshape. The main portion of the signal intensity disappears between 500 and 600 K. The signal disappears completly upon annealing to 1100 K. This sets

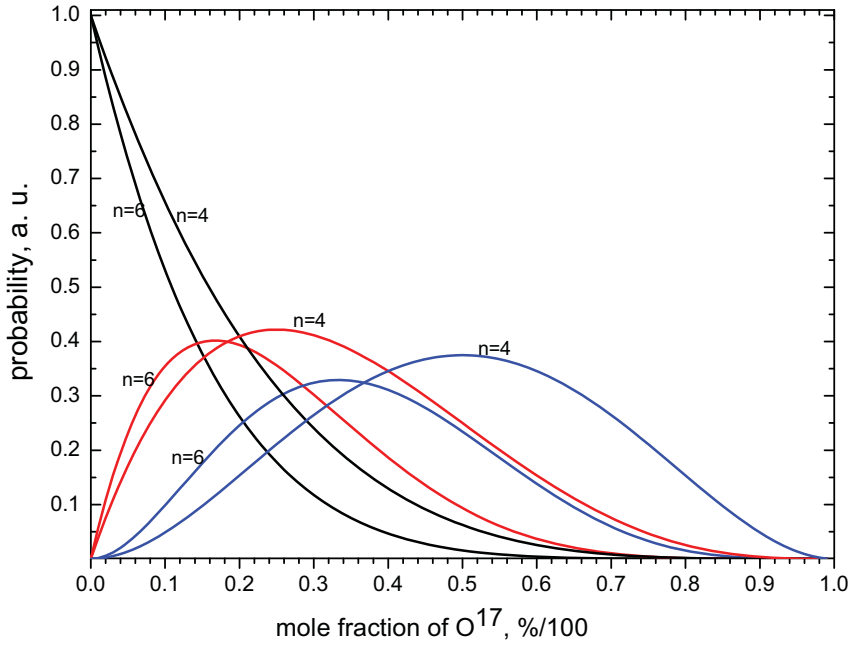

Figure 4.5: Probabilities of finding no ^{17}O atoms (black curves), one ^{17}O atom (red curves) and two atoms ^{17}O (blue curves) for edge (n=4) and bulk (n=6) on MgO.

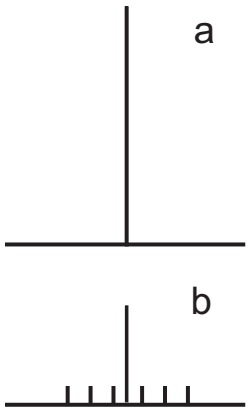

Figure 4.6: Stick diagrams for the original line in a 100% $^{16}O_2$ grown film (a) and for the expected hyperfine pattern with 20 % enrichment of the MgO film with $^{17}O_2$ if the Mo ion interacts with one oxygen ion.

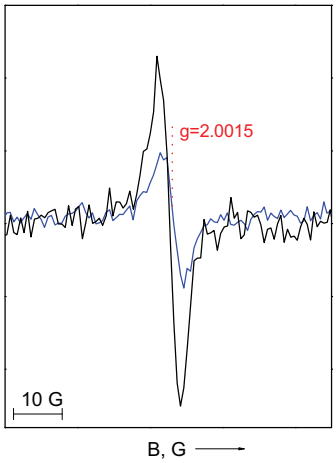

Figure 4.7: EPR spectra of freshly prepared 20 ML MgO(001) film. Blue line: 20 % enrichment of the MgO film with $^{17}O_2$. Black line: for comparasion 100 % $^{16}O_2$ grown film. The spectra were recorded at T = 50 K.

an upper bound for the number of paramagnetic color centers in the film grown at 300 K and annealed to 1100 K of approximately $5\pm2 \times 10^{11}$ [111]. The fact that the signal has several thresholds for the temperature treatment points to the inhomogeneity of the species.

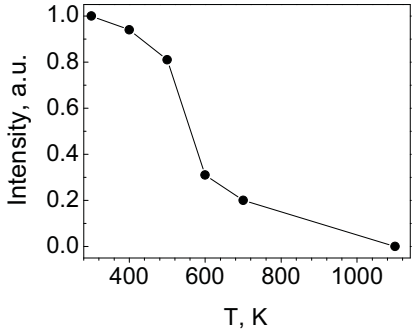

Figure 4.8: EPR intensity of a 20 ML MgO(001) film grown at 300 K as a function of annealing temperature.

Previously, surface color centers were created by electron bombardment on 20 ML thick MgO film grown at 600 K on Mo [121; 116]. These results are going to be compared with the effect of electron bombardement on films grown at 300 K and annealed to 1100 K (see Fig. 4.9). A single asymmetric EPR line around the free electron g-value ($g_e = 2.0023$) is observed (see Fig. 4.9, lower spectrum). The linewidth of the signal is 7 Gauss at 50 K which is broader than the line

appearing upon growth on a pristine film. It remains constant between 50-300 K and the intensity of the line obeys Curie's law. The energy of the electrons was 100 eV, and electron dosage was varied via time of exposure at fixed energy with 10 to 1000 electrons per surface oxygen atom. We observed no change between the amount of species created with different electron dosages, which means that the amount of paramagnetic species is saturated at lower dosages already. The amount of spins can be estimated to be $5\pm2 \times 10^{13}$. It is possible to partially (by 10%) quench this EPR signal upon adsorption of molecular oxygen at 50 K. Therefore, most of these paramagnetic centers are located within bulk of the MgO film. Electron bombardment of MgO films of 8 and 20 ML thickness result in the same signal intensity (Fig. 4.11), which means that the amount of trapped electrons is independent of film thickness. The EPR signal is not observed in films of 4 ML thickness, most likely because the electrons are drained to the Mo support as suggested in ref. [13]. This would require the states for electron traps to be higher in energy than the Fermi energy of Mo. Alternatively, if the traps were below the Fermi energy, electrons could flow from Mo into the traps and form diamagnetic species. Which of the two processes is responsible for the absence of the EPR signal cannot be decided on the basis of our data.

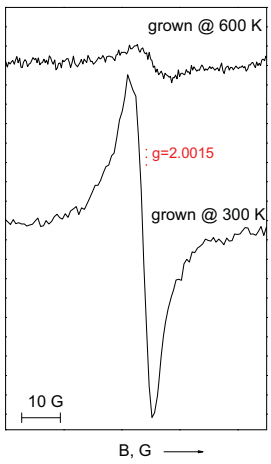

Figure 4.9: EPR spectra of electron bombarded 20 ML films. Bottom: prepared at 300 K and annealed to 1100 K; top: prepared at 600 K.

To obtain information about the g-matrix anisotropy, angular-dependent EPR measurements were performed. We detected no change in lineshape or reso-

nance position; both in the surface plane as well as perpendicular to the surface. Therefore, the g-matrix anisotropy for the paramagnetic species must be small compared to the linewidth.

To further elucidate the location of the trapped electrons, the same isotope substitution experiment with 20% $^{17}O_2$, as already discussed above for the pristine film, was performed. In contrast to the pristine film, in the present experiment a broad resonance with an envelope width of about 20 G was observed (Fig. 4.10). The trapping site for the electron in the electron bombarded annealed film has to be different from the electron in an as-grown film, since the hyperfine interaction has a different pattern (see Fig. 4.7). The intensity of the central line in the spectrum is now about 6 % of the intensity of the line in the purely ^{16}O film. This number was obtained by substraction of the scaled central line, such that the substracted spectrum is a symmetric broad feature. The observed spectrum can be interpreted as an unpaired electron which is surrounded by 10-12 oxygen atoms (as estimated according to Eq.4.1). This is clearly inconsistent with the anticipation of significant hyperfine coupling to the nearest neighbor oygen atoms only. This can mean that the unpaired electron interacts not only with the first coordination shell, but also with the second coordination shell. From the line broadening in the ^{17}O labeling experiment, one can estimate the hyperfine constant for the system to be less than 4 G. This estimate was obtained from the assumption that the sextet has to be accomodated within the 20 G linewidth of the resonance.

90% of the trapped electrons which appeared after electron bombardment have several differences from the surface paramagnetic color centers reported before [121; 116]. The first argument is that the intensity of the EPR line which appeared after electron bombardment is a factor of ten larger than the highest number of electrons that can be stored in paramagnetic point defects (see Fig. 4.9, upper spectrum for comparasion) [121; 116]. Next, we do not observe a decrease in the amount of paramagnetic color centers with increased electron dosage [116], the amount of produced species is saturated much faster than reported for surface paramagnetic color centers, and remains constant. The decrease of the amount of surface paramagnetic color centers was attributed to the formation of diamag-

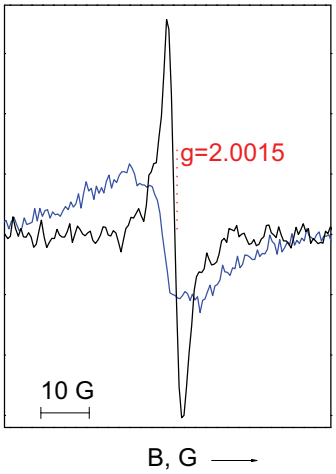

Figure 4.10: EPR spectra of electron bombarded 20 ML MgO(001) films prepared at 300 K and annealed to 1100 K. Blue line: 20 % enrichment of the MgO film with ^{17}O. Black line: for comparasion film grown with 100 % ^{16}O. The spectra were recorded at T = 50 K.

netic counterparts. We would expect a similar mechanism to take place in the present experiment, but the saturation takes place much faster. This can be due to either the higher formation probability or a larger amount of supplied electrons with energies sufficient to form the center. The latter can be explained by the formation of secondary electrons. Finally, in our experiments the linewidth remained constant in the temperature range of 50-300 K, whereas the EPR line from color centers exhibits significant narrowing at room temperature. The other 10% of the observed signal is consistent with the presence of paramagnetic point defects on the surface. Their spectroscopic behaviour is different from surface paramagnetic color centers reported before [121; 116]. While the linewidth of the signal appearing on the film grown at room temperature remains constant between 40-300 K, the signal on the film grown at 600 K shows a considerable narrowing (approx. 1.3 G) at room temperature.

To understand the nature of the electron trapping sites in the as-grown at 300 K film and the film annealed to 1100 K, the literature was reviewed. MgO films grown at 300 K were studied by XPS, GIXD, LEED and STM [141; 31; 11]. As grown at 300 K films are uniform, they consist of small domains between 20 and 60 Å in size, with domain shapes that are random and the perimeters show no preferred orientation [44]. After annealing to 1100 K, a network of

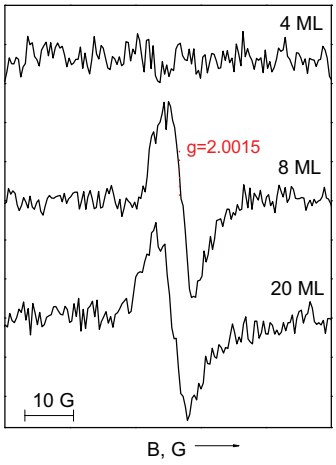

Figure 4.11: EPR spectra of an electron bombarded 20 ML MgO(001) film prepared at 300 K and annealed to 1100 K MgO(001). Films of different thicknesses as indicated.

screw dislocations along the [100] and [010] directions of MgO develops [11]. The dislocations exhibit a distribution of tilting angles. It was shown that grain boundaries are able to serve as electron traps [88]. Therefore we will attribute the EPR signal observed on pristine MgO films grown at 300 K to electrons trapped at grain boundaries of MgO domains. Since the distribution of these trapping sites can be quite broad, this EPR signal shows neither an angular-dependence nor a distinct hyperfine ^{17}O pattern. The quenching of the signal with annealing to 1100 K can be due to the rearrangement of the MgO lattice. After annealing the film to 1100 K, the film reorders and exhibits a network of dislocations. Most likely, the screw dislocations are filled with electrons by electron bombardment. The estimated amount of captured electrons is up to three electrons per nanometer of dislocation line. This observation is consistent with STM studies [13] where it was shown, that it is possible to trap electrons in the dislocation lines by injecting electrons from the STM tip.

4.2.2 Conclusions

We have shown by the means of EPR that a single line appears near the free electron g-value upon the growth of MgO films at 300 K, with the amount of spins being about 5×10^{12}. We will attribute the EPR signal observed on pristine MgO films grown at 300 K to electrons trapped at grain boundaries of MgO domains.

Annealing the film to 1100 K quenches the signal which was attributed to the rearrangements of the film. Electron bombardment of this annealed film results in the appearance of an EPR line near free electron g-value, the amount of spins is about 5×10^{13}. We attribute this signal to trapping of electrons in screw dislocations of MgO films, in line with previous observations by STM.

4.3 Mo ions on high-temperature grown films

4.3.1 Results and Discussion

In Fig. 4.12 (lower spectrum) the EPR spectrum of a 20 ML thick MgO film prepared at 600 K is reported. The spectrum is characterized by one central asymmetric EPR resonance line around g=1.9319 and a sextet of hyperfine lines with a splitting of 37 G. Since the sextet is located symmetrically relative to the central signal, it is likely that they have the same nature. The intensity ratio of the central signal and the sextet of lines is around 75 to 25. The linewidth of the central signal is 9 Gauss at 50 K and it remains constant within a temperature range of 50-300 K while the intensity obeys Curie's law. The EPR signal belongs to a paramagnetic surface species as one can completely quench the EPR signal by adsorption of molecular oxygen at 50 K (Fig. 4.12, upper spectrum). Neither clean nor oxidized Mo crystals exhibit this signal. As in previous chapters, the estimate for the amount of species was based on correlation with the Au spectra [143]. The number of species is about $3\pm2 \times 10^{13}$ cm^{-2}.

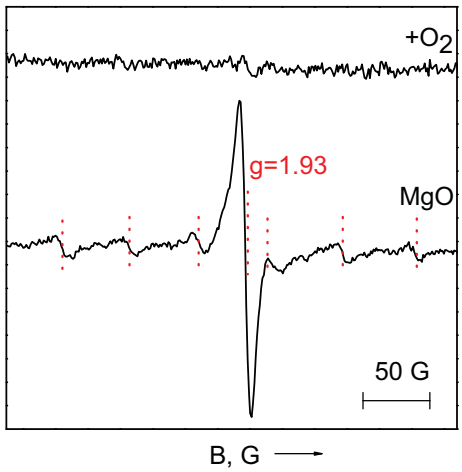

Figure 4.12: EPR spectra of a 20 ML MgO(001) film prepared at 600 K (lower spectrum) and after exposure of the film to molecular oxygen at 50 K (upper spectrum). The spectra were recorded at T = 50 K.

One can think about the most plausible candidates to contribute to this signal. Such a big shift from the free electron g-value has to be due to spin-orbit coupling. Among the possible candidates which could give rise to this signal

the most promising is the Mo^{5+} ion. EPR of Mo^{5+} ions was studied in various polycrystalline, amorphous solids and solutions e.g. [8; 7; 15; 135; 90; 84; 18; 14]. Mo^{5+} has EPR signals with g-values from 1.75 to 1.98, depending upon the local geometry. Molybdenum has six stable isotopes: ^{98}Mo (24.13%), ^{97}Mo (9.55%), ^{96}Mo (16.68%), ^{95}Mo (15.92%), ^{94}Mo (9.25%), ^{92}Mo (14.84%). Only the odd isotopes ^{95}Mo and ^{97}Mo have non-zero nuclear spin (I = 5/2), and their total abundance is around 25%. These odd isotopes will lead to hyperfine structures centered around the main line given by the even isotopes of molybdenum, with I = 0. If an unpaired spin interacts with one Mo^{5+} ion, the intensity distribution will be 75% for the central line (isotopes with I = 0) and 25% for the sextet (isotopes with I = 5/2), as observed in our experiment. The nuclear magnetic moments of ^{95}Mo and ^{97}Mo differ only by 2% (-0.9099 and -0.9290) [36], so the isotopic splitting is not expected to be resolved in the EPR spectra. On MgO powders, Mo^{5+} was found to have $g_1 = 1.9209$, $g_2 = 1.9268$, $g_3 = 1.9310$, $A_x = 38.7$ G, $A_y = 39.4$ G, $A_z = 83.3$ G [90]. Based on comparison with these data, we attribute our EPR signal being due to single Mo^{5+} ions on the surface of MgO film.

In order to obtain the principal values and orientation of the g-matrix of Mo^{5+} ions on the surface, we performed angular-dependent EPR measurements. To extract the g-matrix anisotropy in the surface plane, we performed experiments with the magnetic field lying in different directions within the surface plane. Spectra taken for the magnetic field parallel to the MgO [100] direction and MgO [110] direction exhibit slight changes in the lineshape, the line becomes broader for the latter orientation. The intensity of the signal after rotation was about 40% smaller, which is the result of experimental difficulties and the use of another crystal. Therefore the intensity was too low to observe hyperfine splitting. To investigate g-matrix anisotropy in out-of-surface-plane EPR measurements, varying the angle between the surface normal and the magnetic field were performed. Minor changes in the lineshape and resonance position for the central line were observed, the line slightly shifts to higher fields when going from 90° to 0°. Therefore, the g-matrix anisotropy for the paramagnetic species must be small compared to the linewidth. The g-matrix anisotropy here is smaller than

the one previously reported on MgO powders, although one has to keep in mind that the parameters were extracted from complex powder spectra (see Fig. 4.13), therefore they may be not very precise. The limited signal-to-noise ratio prevents determination of the hyperfine splitting for the hyperfine sextet as a function of magnetic field orientation, which could have given information about the A-matrix anisotropy.

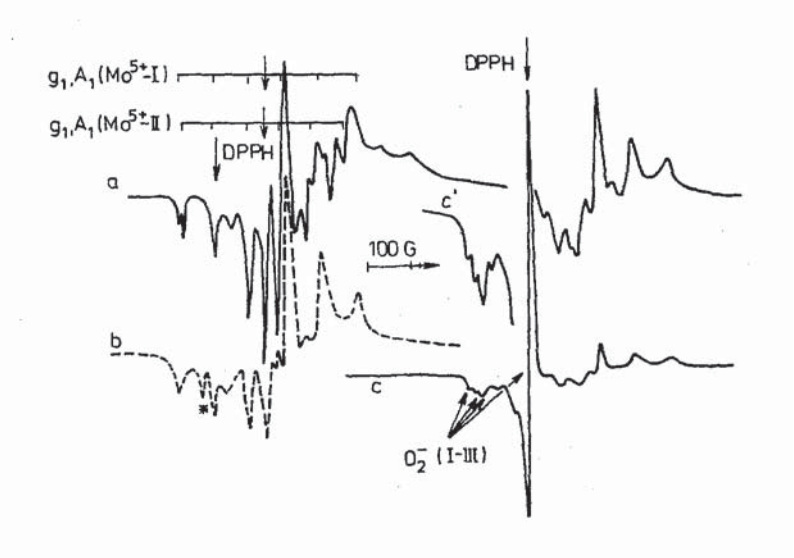

Figure 4.13: EPR spectra of Mo-MgO samples. Picture adopted from ref. [90]

The local oxygen environement of the Mo^{5+} ions can be probed by isotope substitution experiments with $^{17}O_2$. Here, we are going to monitor only the central line of the Mo ion spectrum since the hyperfine sextet has too low intensity for consideration. The same approach as in the previous chapter will be used. The probability of finding m ^{17}O nuclei among n equivalent O^{2-} ions can be calculated using the formula in Eq.4.1. The MgO film investigated here was grown with 20% enrichment of $^{17}O_2$. We do not expect Mo^{5+} ions to substitute for Mg^{2+} ions, but as a first reasonable assumption the coordination number for Mg^{2+} ions in an MgO lattice will be chosen. The percentage of the enrichment was chosen as to maximize the probability $P_n(1)$ of having one $^{17}O^{2-}$ anion ($m = 1$) in a given array ($n = 3, 4, 5, 6$, which corresponds to corner, kink, edge, terrace and bulk) of equivalent ions. $P_n(1)$ was found to be 40 - 35 % for $n = 3 - 6$. The probability $P_n(2)$ of having two $^{17}O^{2-}$ ($m = 2$) is lower (12 - 20 %), the probability to find no $^{17}O^{2-}$ $P_n(0)$ ($m = 0$) is 40 - 25 %. In the case of considerable hyperfine coupling to the nearest neighbor oxygens only, and the simplistic assumption of

equivalent oxygen neigbors, one would expect to observe two predominant features: a sextet of lines due to interaction with ^{17}O (nuclear spin I = 5/2) and one unperturbed line due to Mo in a purely ^{16}O environement. The intensities of these lines would be correspondingly ($P_n(1) \times$ intensity of original line)/6 and $P_n(0) \times$ intensity of original line (Fig. 4.6). In the present experiment, a superpostion of a broad resonance with an envelope width of about 20 G and a small contribution of a central line was observed. In Fig. 4.14, the ^{17}O enriched film is shown on the same plot as a scaled spectrum of Mo ions in a purely ^{16}O film. The intensity of the central line in the spectrum is about 6 % of the intensity of the line in the purely ^{16}O film. This was obtained by substraction of the scaled central line such that the substracted spectrum is a symmetric broad feature. It is clear that this observation is inconsistent with the initial assumption, namely the number of the oxygen atoms surrounding Mo ion. Instead, the apparent increase in the linewidth may be understood in terms of unresolved hyperfine couplings to several ^{17}O nuclei with different hyperfine coupling constants, which suggests that the unpaired electron wavefunction extends over a number of oxygens. One can estimate the biggest hyperfine constant for the system to be less than 4 G if one assumes that the sextet of the unresolved hyperfine structure has to be accomodated in the broad resonance of 20 G.

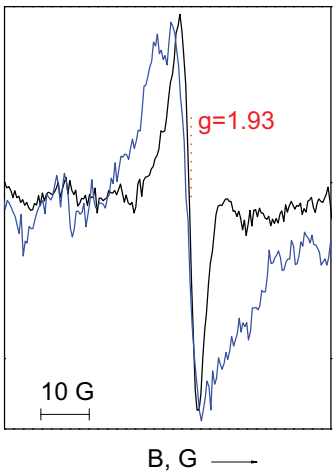

Figure 4.14: EPR spectra of a 20 ML MgO(001) film grown at 600 K. Blue line: 20 % enrichment of the MgO film with $^{17}O_2$. Black line: for comparasion, 100% $^{17}O_2$ grown film, the spectrum was scaled to 30 % of original amplitude. The spectra were recorded at T = 50 K.

To get an idea of how the amount of Mo ions depends on the thickness, we prepared MgO films of different thicknesses. Recently it was shown by AES (Auger Electron Spectroscopy) that 25% of the surface atoms in MgO films of 2 ML thickness are Mo atoms [96]. In Fig. 4.15 we report EPR spectra of MgO films of 4, 8, 20 and 50 ML thicknesses prepared at 600 K. One can see that the signal undergoes severe changes in terms of the amplitude, shape and linewidth from 4 to 50 ML. In Fig. 4.16 the comparison of the amplitudes, intensities and linewidths of the signals is presented. EPR allows estimation of the relative number of paramagnetic species by comparision of the relative intensities. Intensities were calculated by double integration of the spectra. One has to note that the determination of the intensity of spectra corresponding to films of 4 and 8 ML is severely hampered by the baseline as well as signal-to-noise problems. The amount of Mo^{5+} ions grows with film thickness up to 20 ML, then decreases by 30 % for the 50 ML film. The linewidth is monotonically decreasing from 19 G for 4 ML film to 7 G for 50 ML film, whereas the amplitude is monotonically increasing. The larger linewidth at smaller MgO film thicknesses can be explained by inhomogeneous broadening caused by the presence of spins in a larger variety of local environments since thinner films exhibit a more disordered surface [10]. The paramagnetic centers were shown to be stable at least up to 1100 K. The amount of Mo^{5+} ions and the linewidth does not change upon annealing.

One can expect Mo paramagnetic ions to be reactive species, because they can take part in redox chemistry. Next we are going to show that Mo^{5+} ions are reactive species. In the previous chapter it was demonstrated that films grown at room temperature are free of paramagnetic Mo surface ions. On the other hand, they exhibit other type of imperfections, namely a large fraction of dislocation lines and a lower level of long range order. Because of the lack of Mo ions, these surfaces are well suited to serve as controls for the impact Mo ions have on the properties of the paramagnetic species investigated here. This will be done throughout the thesis to make sure that the results are not film preparation dependent. It will be shown in Chapter 5.2.3 that MgO reactivity can be discussed separately from Mo reactivity under the treatments discussed further. Namely, it will be shown that upon electron bombardement of MgO

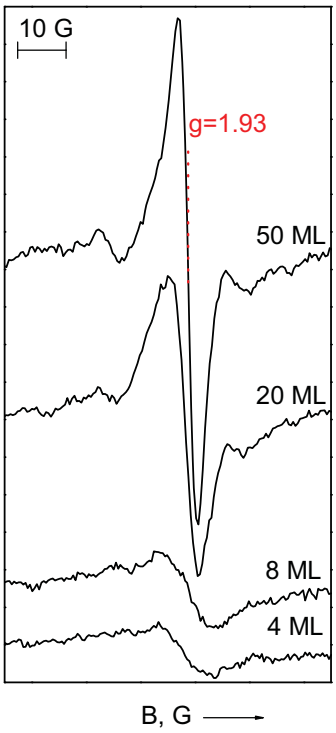

Figure 4.15: EPR spectra of MgO(001) films of different thicknesses as indicated prepared at 600 K. The spectra were recorded at T = 50 K.

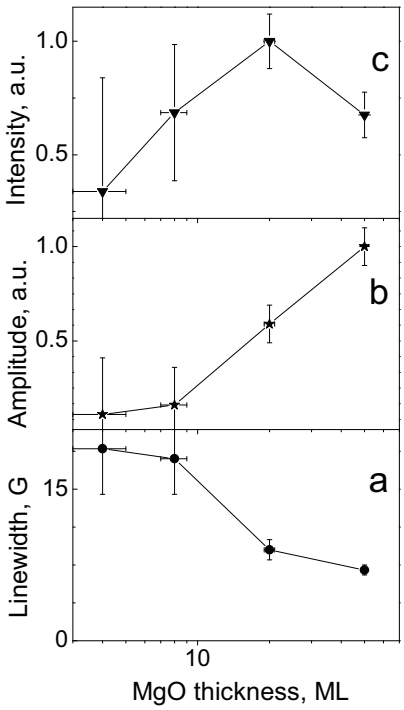

Figure 4.16: Linewidth (plot a), amplitude (plot b) and intensity (plot c) of EPR spectra of MgO(001) films prepared at 600 K as a function of MgO thickness.

with subsequent nitrous oxide treatment, O^- radicals can be created indepedent of the presence of Mo ions on the surface. The Mo^{5+} signal can be completely quenched by electron bombardment, since the EPR signal disappears after the treatment (see Fig. 4.17). The Mo^{5+} EPR signal remains silent after the addition of one monolayer of N_2O at 50 K. With annealing, the signal at g=1.93 slowly grows (see Fig. 4.17, inset). After heating to 300 K, the signal around g = 1.93 is restored, and the intensity is 3 times smaller, while the linewidth and shape are the same. Simultaneously, a new signal around g = 1.98 appears (Fig. 4.17, upper curve). The linewidth of the signal around g = 1.98 is 8 Gauss at 50 K. The new paramagnetic species observed by EPR are located on the surface of the MgO film as verified by a complete quenching of the EPR signal upon adsorption of molecular oxygen at 50 K. In this experiment the magnetic field direction was perpendicular to the surface normal and was oriented in the surface plane collinear with a MgO [100] equivalent direction. Rotating the sample in the surface plane by 45° (B || [110]) changes the feature located around g = 1.98. The linewidth becomes 11 G (3 G broader) and shifts by 2 G to higher fields. The change in the spectrum indicates some g-matrix anisotropy in the surface plane. The species were found to be stable up to at least 600 K.

Reaction of Mo^{5+} ions with N_2O has been studied on oxides, e.g. SiO_2 powders [22; 76]. It was found that the adsorption of 30 torr N_2O at 100 °C on molybdenum catalysts results in the creation of O^- radicals with g-matrix components higher than the free electron g-value. The signal around g=1.98 is not compatible with the O^- species described in the literature (e.g. [22; 76; 128]). No reaction of Mo^{5+} with N_2O without electron bombardment was observed, because adsorption of N_2O at 50-100 K does not quench the Mo signal. One can expect this signal to originate from paramagnetic Mo ions, which are spectroscopically different from the original Mo ions giving rise to the signal at g = 1.93. There are two possibilities as far as the Mo species is concerned: Mo^{5+} ions with different coordination and Mo^{3+} ions. Mo^{5+} ions were shown to have a very broad range of g-matrix values, depending upon the coordination. In particular, g-matrices with rather small anisotropy, compatible with what was observed here, and values such as g_1 = 1.999; g_2 = 1.985; g_3 = 1.964 or g_1 =1.980; g_2 =1.973; g_3 =

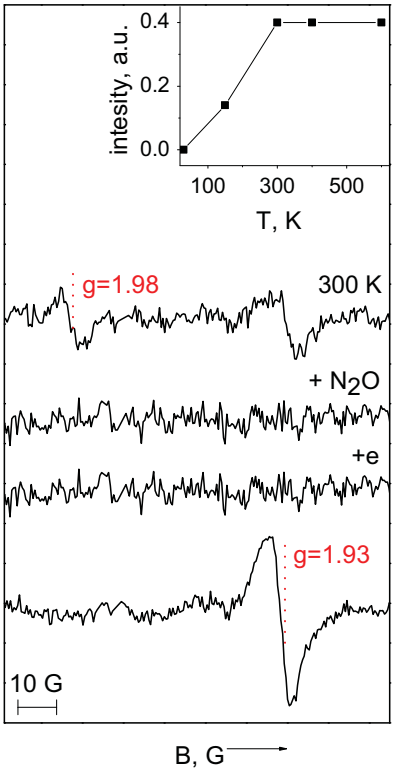

Figure 4.17: EPR spectra of a MgO(001) film prepared at 600 K (lowest curve) and consequently treated as indicated above each spectrum. The spectra were recorded at T = 50 K. The inset shows the dependence of the relative intensity of the signal around g = 1.93 (the inital signal at the lowest curve is a unity) on annealing temperature after electron bombardment and nitrous oxide admission.

1.967 were observed for Mo^{5+} ions on enzymes [133; 85]. EPR of Mo^{3+} ions was studied in corundum [112], where g-values were found to be around $g_{||} = 1.968$, $g_{\perp} = 1.98$. Most likely after electron bombardment the paramagnetic Mo^{5+} ions are reduced to diamagnetic Mo ions. Simultaneously oxygen vacancies near Mo ions can be created by electron stimulated desorption. After N_2O admission and thermal activation, we are changing the coordination of Mo^{5+} ions, leading to the appearance of Mo^{5+} ions species with a g-value around 1.98. One would not expect that after electron bombardment and oxidative treatment of N_2O we would be able to create Mo^{3+} ions. The total intensity of the signal around g=1.98 plus the signal around g=1.93 after the treatment is about 20% smaller than the initial intensity of the Mo^{5+} ions. Given the error of the determination this is rather close to the original amount of paramagnetic Mo species. It is possible that Mo ions are present on the surface in other than paramagnetic Mo^{5+} oxidation states. Since EPR is sensitive only to paramagnetic species, we can not comment on the fate of such non-paramagnetic species. These reactivity experiments show that Mo ions are reactive species.

4.3.2 Conclusions

We have shown that Mo^{5+} ions appear on the surface of MgO(001) films grown on Mo(001) at 600 K. The maximal amount of the paramagnetic ions can be estimated to be $3\pm2 \times 10^{13}$ cm^{-2} and they are stable up to 1100 K. These ions were detected on the surface of ultrathin (8 Å) as well as thick films (100 Å). One has to be careful when analyzing the interaction of adsorbates with MgO films, since Mo^{5+} ions were shown to be reactive species. The best strategy to achieve the preparation-independent result is to compare data obtained on films grown at 600 K versus 300 K.

4.4 Mg additive coloring of thin MgO films

4.4.1 Motivation

First, the information available in the literature on color centers produced by Mg additive coloring will be briefly reviewed. Surface color centers on MgO powders produced by Mg addition were studied by EPR [144; 49; 48]. After evaporation of Mg at temperatures around 800 K on MgO powders, an EPR signal near the free electron g-value was observed and attributed to the formation of F_s^+ centers. Several surface science studies on additive coloring by Mg on single-crystalline MgO films have been performed [126; 68]. Kantorovich *et al.* used metastable impact electron spectroscopy (MIES) to study Mg deposition at 100 K on MgO(001) films. Experimental results were compared with theoretical calculations. After the deposition of a small amount of Mg (which is not exactly defined in the reference [68]) a new feature 2 eV above the valence band appeared. Based on the theoretical calculations, the peak around 2 eV found at low coverage was rationalized, as the presence of Mg atoms or small clusters, while at high coverage the work function measurements prove the existence of metallic Mg clusters. There was no clear indication for the presence of color centers. In the paper by Tegenkamp *et al.* [126] defects on MgO films were produced by evaporating monolayers of Mg at 300 K and studied using electron energy loss spectroscopy (EELS). Two new features in the bandgap of MgO were detected by EELS after Mg treatment and subsequent thermal annealing, and were tentatively assigned to color centers.

In this chapter, experimental evidence for the formation of paramagnetic color centers upon Mg deposition on a single-crystalline MgO(001) thin film under UHV conditions will be provided.

4.4.2 Results and Discussion

First, low temperature (50 K) deposition of Mg adatoms on a MgO(001) film grown at 600 K will be discussed. In Figure 4.18, EPR spectra collected after deposition of different amounts of Mg on a 20 ML thick MgO(001) film are shown. The lowest spectrum represents the background spectrum of the freshly

prepared MgO film, indicating no EPR signal beyond the detection limit of our EPR setup (except the signal from Mo ions discussed in previous chapter). After deposition of the lowest amount (0.005 ML) of Mg onto the pristine film, a new signal around the g-value of a free electron appears. The linewidth of the signal is 7 Gauss and remains constant within the temperature range of 50–300 K. These paramagnetic centers are located on the surface of the MgO film, because the EPR signal can be completely quenched upon adsorption of molecular oxygen at 50 K. The EPR line is almost symmetric and angular dependent measurements reveal neither a change in the lineshape nor in resonance position. This means that the g-matrix anisotropy for the system must be small as compared with linewidth at this frequency. Based on a comparasion with Mg coloring of MgO powders [144; 49; 48], this EPR signal can be attributed to paramagnetic surface color centers (also denoted as F_s^+ centers). Although one has to mention that F_s^+ centers were produced on powders by high (around 800 K) temperature deposition, so the location of these paramagnetic centers may be different from our species. As was already mentioned in the Chapter 4.2.2, surface color centers on MgO films created by electron bombardment were characterized recently using EPR spectroscopy as well as STM [121; 116]. At low temperatures, these centers show a very similar EPR spectrum in terms of their resonance position and linewidth when compared to the Mg induced ones (Figure 4.19). However, there are two differences between the two methods of color centers production. The first difference is the different temperature behavior of the linewidth. While the Mg induced signal exhibits a 7 G wide signal between 50 and 300 K, the electron bombarded system shows a considerable narrowing ($\Delta H_{pp}(300K) \approx 1.3$ G) of the signal at high temperatures. The larger linewidth observed for Mg induced signal is attributed to inhomogeneous broadening caused by the presence of color centers at a variety of different local environments. The g-matrix anisotropy found for electron induced color centers is small (0.5 G) at this frequency. Therefore it is not to be expected that this anisotropy can be picked up by angular dependent measurements of the inhomogeneously broadened line corresponding to Mg induced centers. The second difference is in the location of the color centers. In the case of the electron bombarded system it was shown that the F-centers are

predominately located at the edges of the MgO islands (Figure 4.21) [121; 116]. There, the electrons are located in oxygen vacancies which are created through an electron stimulated desorption process [77]. High resolution STM measurements show that the number of oxygen vacancies present on the as-grown film is very low if present at all[116]. Therefore, it is not reasonable to assume that the Mg induced color centers are also trapped electrons within oxygen vacancies. Instead, the EPR signal observed here is attributed to electrons which are scavenged at morphological defects of the surface, such as kinks or reversed corners (Figure 4.20). Theoretical calculations have shown that a stabilization of electrons is possible at a variety of sites as kinks, and reversed corners [106; 27]. Since the amount of low coordinated sites (kinks, reversed corners) is limited, it is worth looking at what happens with the amount of color centers produced as a function of the Mg coverage.

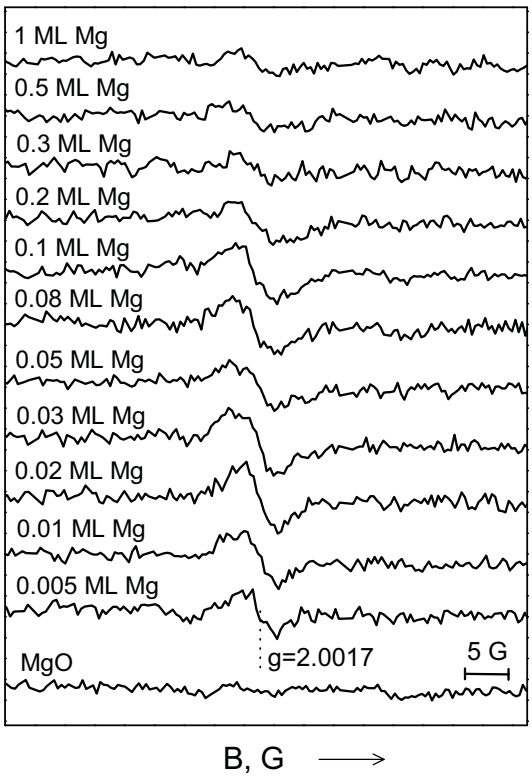

Figure 4.18: EPR spectra of the bare 20 ML MgO(001) film (lowest spectrum) and after Mg deposition with increasing coverage.

In Figure 4.22, one can see the peak-to-peak amplitude of the F_s^+ centers related signal (deduced from Fig. 4.18) as a function of the Mg coverage. The

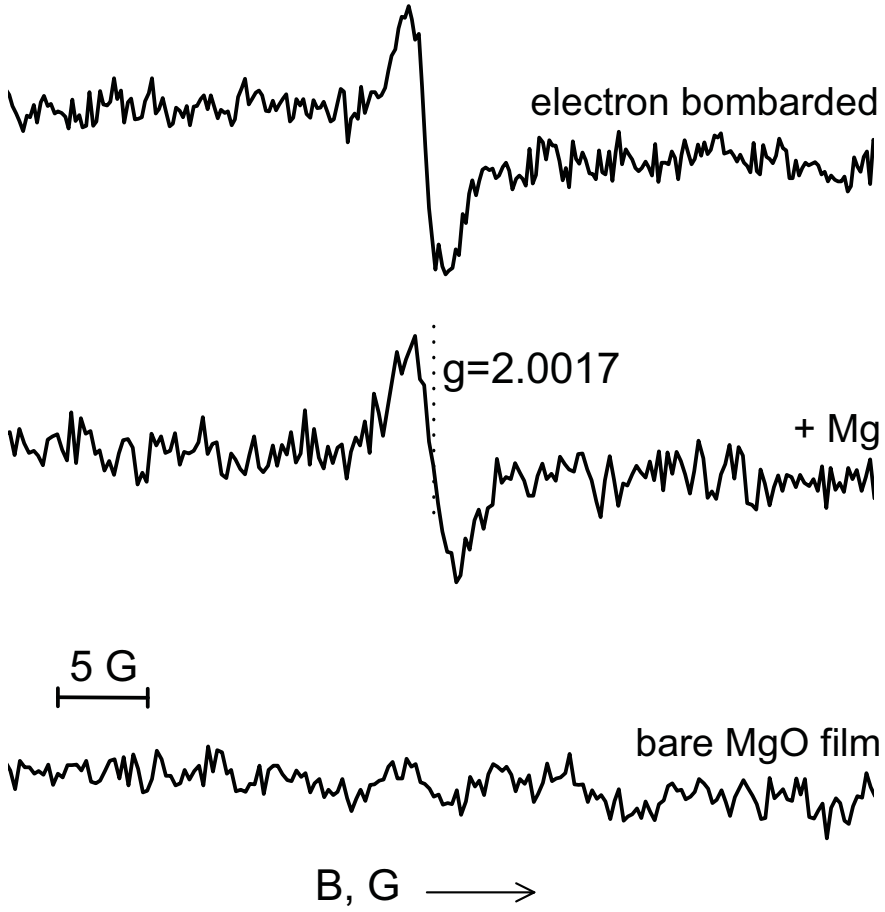

Figure 4.19: EPR spectra of bare 20 ML MgO(001) film (lowest spectrum), after Mg deposition, and after electron bombardment.

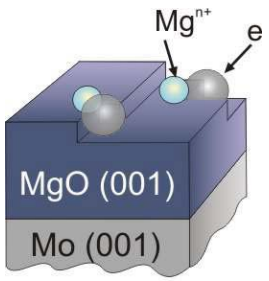

Figure 4.20: Schematic location of color centers made by Mg addition.

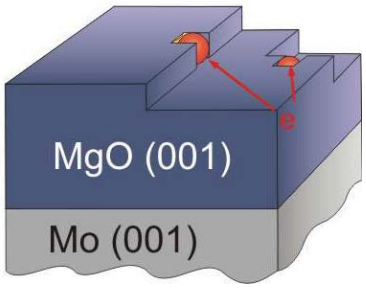

Figure 4.21: Schematic location of color centers made by electron bombardment.

use of the peak to peak amplitude as a measure of the intensity is valid, because there is no variation in lineshape within this series of experiments. The lack of changes in lineshape also means that there is no significant change in the nature of the environment of the defects. The signal intensity increases by 50 % from 0.005 ML to a Mg coverage of 0.03 ML and decreases again for higher exposures. Based on a correlation with the EPR spectra of deposited Au atoms, the maximal amount of Mg induced color centers is estimated to be 2-3 $\times$ 10^{12} cm^{-2}.

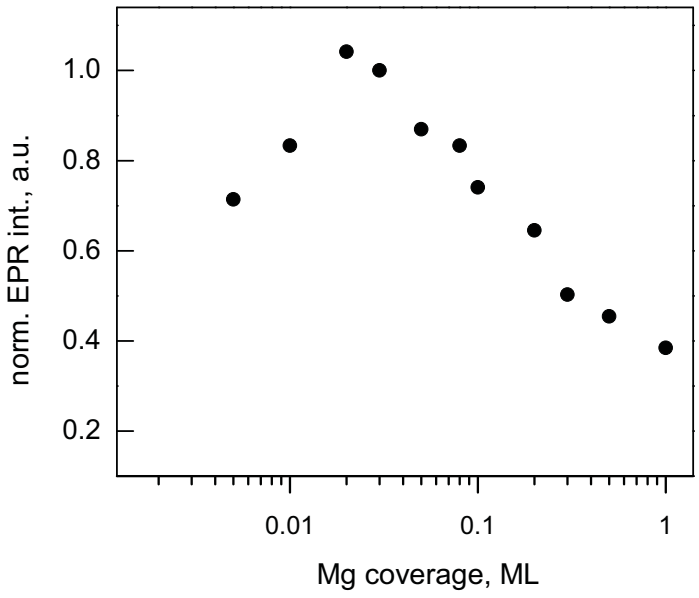

Figure 4.22: Semilogarithmic plot of the F_s^+ center EPR peak-to-peak intensity, depending on the Mg coverage derived from the spectra in Fig. 4.18.

There are various possible explanations for the observed decrease of the EPR intensity for Mg coverages beyond 0.03 ML. The dependence on electron dosage has shown a similar behavior observed for electron induced F_s^+ centers. The decrease of the amount of F_s^+ centers was explained by the formation of diamagnetic

F_s^0 centers, which are more stable oxygen vacancies [116]. The formation of diamagnetic color centers cannot be excluded based on the EPR data and was also proposed [49]. However, one has to keep in mind that the location of the electron induced centers is different from Mg induced ones. While the doubly filled oxygen vacancies are more stable than a single trapped electron in the oxygen vacancy, this is not true for electrons trapped at morphological defects. Thus, it cannot be considered the natural explanation for the observed effect. Another explanation for the decrease of F_s^+ center related signal intensity at higher coverage could be the formation of Mg clusters nucleating at or close to the trapping sites. This scenario is in agreement with TPD measurements by Goodman and coworkers which show evidence of the growth of 3-dimensional Mg clusters from very early stages of the Mg deposition [51]. To support the hypothesis of Mg cluster formation at higher Mg coverages, the same system was investigated by IR spectroscopy using CO as a probe molecule.

First, we will revisit infrared spectra of CO adsorbed on the surface of MgO(100). The interaction of CO with the MgO surface was studied theoretically [104; 100; 24; 97] and experimentally for powders, single crystals and thin films e.g. [87; 122; 60; 35; 138]. The binding mode of CO on the regular MgO surface and the influence of differently coordinated binding sites on the CO infrared frequency shift was investigated theoretically [97]. It is now established that CO binds with the carbon-end down to surface magnesium sites and that the binding is almost purely due to electrostatic interactions. A blue shift of the CO stretching mode with respect to the stretching mode of gaseous CO (2143.3 cm^{-1}) has been explained as being due to the repulsive interaction between the carbon atom and the surface anions. A reduction of the coordination number of Mg sites, e.g. at steps or corners, leads to stronger binding because of the larger local electric field for low-coordinated ions. Accordingly, a shift of the CO stretching frequency to higher energies is observed, which arises from a stronger polarization of the adsorbed molecule at these sites. The p-polarized infrared spectra taken after saturating the surface of a vacuum-cleaved MgO single crystal with CO below 40 K exhibit three bands at 2151, 2137 and 2132 cm^{-1} [60]. Excitation with s-polarized light reveals a spectrum with a single line at 2132 cm^{-1}. A combination

of temperature dependent IR measurements, LEED, and helium atom scattering experiments [60] allowed to assign the main band at 2151 cm^{-1} to perpendicularly oriented CO molecules adsorbed on regular terrace sites, while the latter two bands were attributed to the in-phase and out-of-phase vibrational excitation of tilted CO in a c(4 × 2) overlayer, respectively. The signal at 2132 cm^{-1} was assigned to the out-of-phase vibrational excitation of the tilted CO molecule, which corresponds to a parallel orientation of the dynamic dipole moment with respect to the surface. The characteristic c(4 × 2) superstructure and the two bands for the in-phase and out-of-phase vibrational excitation disappear at temperatures above 40 K. The infrared spectra taken after saturating the surface of a well ordered 20 ML MgO(001) thin film supported on Mo(001) at 30 K with CO is characterized by a relatively sharp band at 2152 cm^{-1} with a shoulder at higher frequency and a pronounced feature at 2138 cm^{-1} [122]. The lack of the band at 2132 cm^{-1} is due to the metal surface selection rule, which limits the observable transitions to those with dynamic dipole moments oriented perpendicular to the surface. TPD experiments on well annealed thin MgO(001) films show a CO desorption behavior which is very similar to that of single crystals, namely that the main desorption peak (corresponding to CO desorption from terrace sites) is found at 52 K, followed by a broad and less intense desorption feature up to 100 K which is assigned to CO bound to low coordinated Mg ions [35; 122]. At temperatures of about 50 K, the corresponding CO IR spectrum at saturation coverage is characterized by a symmetric signal around 2168 cm^{-1}, which corresponds to CO bound to morphological defects of the MgO surface.

The IR spectra taken for different amounts of deposited Mg are shown in Fig. 4.23. All spectra were measured after saturating the surface with CO at 50 K. The upper curve shows the IR spectrum for CO on a pristine high temperature grown MgO film, which is characterized by a symmetric signal around 2168 cm^{-1}, in line with the previous study discussed above [122; 123]. After the deposition of a small Mg amount (0.1 ML), the spectral feature of the bare MgO film (2168 cm^{-1}) changes only slightly. No new feature associated with the added Mg metal can be found. The amplitude of the peak at 2168 cm^{-1} is slightly reduced and the lineshape is altered. These changes in the spectrum can

be explained by accommodation of a small Mg amount at morphological defects of MgO. After deposition of 1 ML of Mg a new relatively broad band appears around 2100 cm^{-1}. At the same time one can observe a significant reduction of the intensity of the MgO related peak which is also shifted by 4 cm^{-1} to the red (peak at 2164 cm^{-1}). An increase of the Mg coverage to 2 ML results in a further decrease of the signal at 2160 cm^{-1} while the band around 2100 cm^{-1} becomes more pronounced. This new band at 2100 cm^{-1} is typically found for CO adsorbed on top of metal surfaces. Therefore we assign it to CO bound to metallic Mg. The decrease of the intensity of CO bound to defects of MgO film (band at 2160 cm^{-1}) can be explained by nucleation of Mg on these sites, hence blocking them for CO adsorption. The fact that the band at 2160 cm^{-1} is still observed after deposition of 2 ML Mg points to 3-dimensional (3D) growth of Mg clusters, in agreement with the TPD data mentioned above [51].

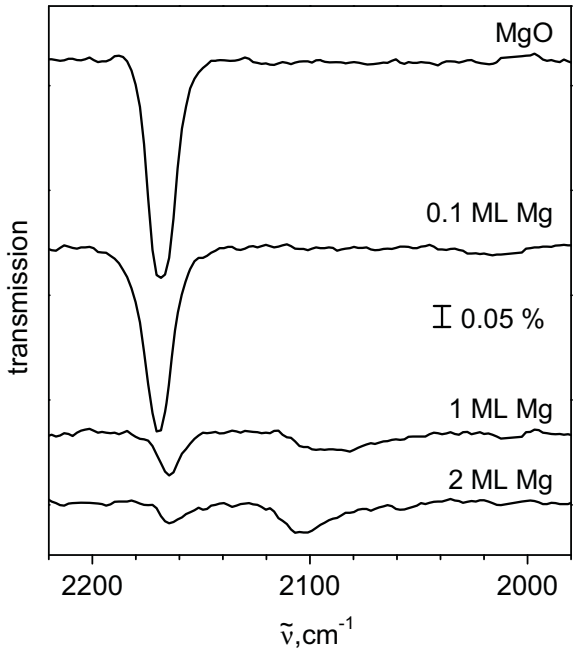

Figure 4.23: IR spectra of adsorbed CO molecules at saturation coverage for bare MgO (upper curve) and different Mg coverages on the MgO(100) thin film. CO adsorption and IR measurements were performed at 50 K.

To the best of our knowledge, the stretching frequency of CO on magnesium clusters or single crystals has not yet been reported. Based on an analogy with other sp band metals such as Al it is expected that the interaction of the CO with Mg is rather weak and that the red shift should be small. Within a simple

Blyholder model [17], it can be explained by small back donation into the π^*-orbital of the CO due to the lack of appropriate filled orbitals. For Al(100) this results in a CO stretching frequency of 2135 cm^{-1} [108]. The red shift observed here is significantly larger and closer to values found for CO on top of transition metals. The adsorption strength of CO on the Mg clusters can be estimated by annealing experiments. The three traces at the top of Figure 4.24 show that the CO adsorbed on the Mg clusters (1 ML Mg on MgO) is already desorbed at 70 K. This confirms a rather weak interaction of CO with metallic Mg. The corresponding CO binding energy is estimated to be around 0.14 eV within the Redhead approximation [105] and assuming a desorption maximum in the given temperature window. To find out whether the desorption at 70 K is reversible or not, we performed readsorption experiments. A subsequent readsorption of CO at 50 K restores the original situation, indicating a reversible behavior, and thus stable Mg clusters, in this temperature range. The band at 2168 cm^{-1}, corresponding to CO molecules bound to the MgO surface undergoes a small shift to higher wavenumbers and decreases in intensity after annealing to 70 K. This indicates partial desorption of CO from the MgO surface, in agreement with previous studies [122; 123]. In a subsequent step, the system was annealed to 110 K, which resulted in complete CO desorption from the surface. After CO readsorption at 50 K only one band appears at 2168 cm^{-1}. This band is broader and more intense than the original one. This points to an increase in the amount of morphological defects on the MgO surface. The lack of an IR band around 2100 cm^{-1} indicates an irreversible change of the metallic Mg clusters after annealing to 110 K.

A similar result is observed when Mg adatoms are deposited at room temperature on 20 ML thick MgO film grown at 600 K. Figure 4.25 reports IR spectra of CO molecules adsorbed on 1 ML Mg deposited on MgO film, where Mg was deposited at 50K with subsequent annealing to 300 K (curve b), and 1 ML Mg deposited on MgO film, where Mg was deposited at 300 K (curve c). The upper curve (a) gives CO infrared spectra of the bare MgO film for comparision. CO infrared spectra of the film with up to 3 ML of deposited Mg at 300 K results only in the appearance of the band associated with CO on MgO morphologi-

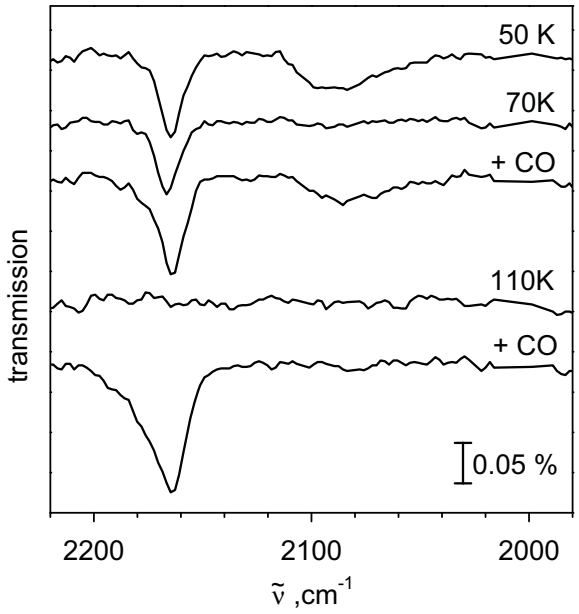

Figure 4.24: IR spectra of CO molecules adsorbed on a 1 ML Mg/20 ML MgO(100) film. At 50 K, the surface was saturated with CO. The sample was annealed to the indicated temperature. All spectra were measured at 50 K.

cal defects. This can be rationalized by a reaction of the metallic Mg clusters at elevated temperatures with the MgO surface, resulting in the formation of a reduced MgO film. Recently, the absence of Mg particles in the STM images after depositing 1 ML Mg onto the MgO/Mo films at 300 K was shown [12]. It was suggested that the various line defects are possible candidates to trigger the partial oxidation of Mg or the reduction of the film.

4.4.3 Conclusions

EPR experiments have shown the possibility to produce paramagnetic surface color centers, F_s^+, by deposition of small amounts of Mg at low temperatures on MgO(001) single-crystalline thin films. These centers are assigned to unpaired electrons trapped at morphological defects of the MgO surface. The number of Mg-induced F_s^+ centers goes through a maximum with increasing Mg coverage and decreases for Mg coverages above 0.03 ML. The depletion of the color centers at higher coverages is attributed to the formation of metallic magnesium clusters. The formation of metallic Mg clusters was confirmed by IR spectroscopy using CO as a probe molecule. CO binds to Mg clusters weakly (the binding

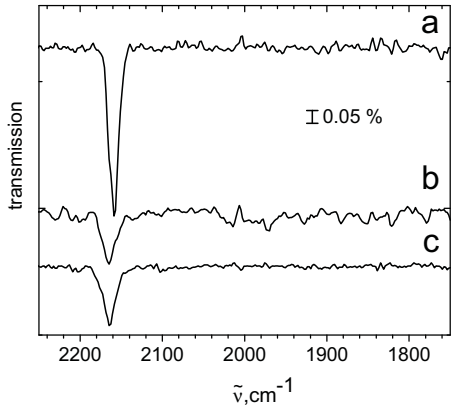

Figure 4.25: IR spectra of CO molecules adsorbed on the bare MgO film (a), 1 ML Mg/20 ML MgO(100), where Mg was deposited at 50 K with subsequent annealing to 300 K (b), 1 ML Mg/20 ML MgO(100) where Mg was deposited at 300 K (c). The surface was saturated with CO at 50 K. All spectra were measured at 50 K.

energy is around 0.14 eV). Mg metallic clusters were found to be substantially low temperature species, they become oxidized already at 100 K.

4.5 Hydrogen-generated surface excess electrons on thin MgO films

4.5.1 Motivation

Two methods used to create surface color centers on MgO films, electron bombardment [121; 116; 75] and addition of Mg at low temperatures (Chapter 4.4.3), have been already discussed. As hydrogen addition was used to create color centers on MgO powders, it is desirable to obtain information about color centers created by this method on the surface of MgO films, too.

First, the current knowledge about paramagnetic centers created by hydrogen treatment on MgO powder will be reviewed. In the first generation of experiments, hydrogen atoms produced by microwave discharge were used to create paramagnetic centers on MgO powders [113]. EPR experiments have shown a single line with a small doublet splitting attributed to electrons trapped at a surface anionic vacancy with a nearby hydrogen nucleus. A similar effect was obtained in the same group by UV irradiation in the presence of adsorbed H_2 [129; 94; 130; 93; 127]. The observed paramagnetic centers were called $F_s^+(H)$ centers (H stresses the presence of a proton close to the trapped electron). Schematically this can be expressed in a following way:

$$\begin{array}{cccccccccc} & & & & & & & & & H^+ \\ & & & & & & & & & O \\ O & Mg & O & Mg & \xrightarrow{H} & O & Mg & e & & Mg \\ Mg & O & Mg & O & & Mg & O & Mg & & O \end{array}$$

Later, this model was reexamined on the basis of more detailed EPR data, improved MgO powder preparation and quantum chemical calculations [106; 28; 29; 26; 27; 120; 33]. In the later experiments, paramagnetic centers were produced on the surface of the MgO powder by UV irradiation in the presence of adsorbed H_2. The mechanism of formation of trapped electrons is complex and comprised at least two distinct processes. The first reaction mechanism happens in the two following steps. The first step is the heterolytic dissociation of H_2 molecules

on low-coordinated (steps, edges, corners, reversed corners) sites. This step was confirmed by IR experiments. The next step, which was confirmed by EPR, is desorption of a neutral H atom under UV light and formation of a paramagnetic surface center:

$$\begin{array}{cccccccccccccc} & & & & & & H^- & H^+ & & & & e & H^+ & \\ O & Mg & O & Mg & \overset{H_2}{\rightarrow} & O & Mg & O & Mg & \overset{UV}{\rightarrow} & O & Mg & O & Mg + H \\ Mg & O & Mg & O & & Mg & O & Mg & O & & Mg & O & Mg & O \end{array}$$

The second type of reaction, which was monitored by IR and EPR, is the homolytic splitting of H_2 on a surface O^- ion produced at low coordinated sites, by UV-induced charge transfer at a surface cation-anion pair:

$$\begin{array}{cccccccccccccc} & & & & & & & & & & H^+ & e & & \\ O & Mg & O & Mg & \overset{UV}{\rightarrow} & O^- & Mg & O & Mg & \overset{H_2}{\rightarrow} & O & Mg & O & Mg + H \\ Mg & O & Mg & O & & Mg & O & Mg & O & & Mg & O & Mg & O \end{array}$$

The EPR line observed was around the free electron g-value with a ^{1}H (I=1/2) hyperfine splitting of 2.07 Gauss. Nowadays, it is accepted that so-called F_s^+(H) centers are identified by an electrons trapped at morphological defect stabilized by a proton close by. They are rather well defined species because monochromatic UV light makes excitations on specific MgO sites (corners or edges) depending upon the energy used.

In this chapter, the aim is to provide the first direct experimental evidence for the formation of color centers upon chemisorption of hydrogen atoms at 100 K on a single-crystalline MgO(001) thin film under UHV conditions. The formation of hydrogen-generated paramagnetic color centers and their local coordination as inferred from EPR spectroscopy will be discussed. In addition, the similarities and differences between surface trapped electrons generated by the three different methods (electron bombardment [121], Mg additive coloring and hydrogen-generated) employed here on thin single-crystalline MgO(001) films will be highlighted.

4.5.2 Results and Discussion

First, the interaction of H atoms with the film grown at 600 K will be discussed. In Figure 4.26, the EPR spectrum collected after reaction of a 20 ML thick MgO(001) film with hydrogen atoms is reported. The lowest spectrum shows the background spectrum of the freshly prepared MgO film indicating no EPR signal (except a signal related to Mo impurities discussed in Chapter 4.3.2) within the detection limit of our EPR setup. After exposure of the MgO film at 100 K to hydrogen atoms, a single asymmetric EPR resonance line around the free spin value ($g_e = 2.0023$) appears (Fig. 4.26, upper curve). The linewidth of the signal is 9 Gauss at 50 K and it remains constant between 50-300 K. One can quench the EPR signal completely upon adsorption of molecular oxygen at 50 K, which means that they are located on the surface of the MgO film. The same strategy as in previous chapters, based on comparison with spectra measured for Au atoms deposited at low temperatures [143], was used to estimate the number of paramagnetic centers. The amount of spins is about 2-3$\pm$2 $\times$ 10^{12} cm^{-2}. The centers were shown to be stable up to 600 K.

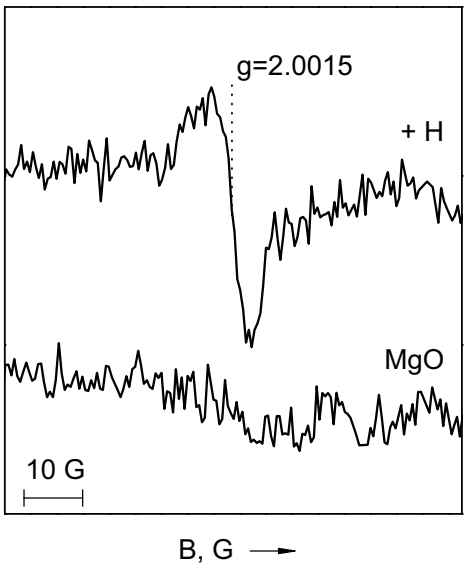

Figure 4.26: EPR spectra of a bare 20 ML MgO(001) film grown at 600 K (lower spectrum) and after exposure of the film to hydrogen atoms (upper spectrum).

Since the hydrogen atoms used for creation of paramagnetic centers have a non-zero nuclear spin, one can use this fact to study the hyperfine interaction

with the unpaired electron and thus get an idea how close the electron is to the H nucleus. If the electron is located in the 1s orbital of the hydrogen atom (nuclear spin I = 1/2), the EPR measurement should give a doublet with large hyperfine splitting. The size of the splitting depends strongly on the environment, e.g. a splitting of 500 G was found for hydrogen atoms trapped in point defect sites of alkali halides [114]. The lack of the hyperfine interaction expected for atomic hydrogen indicates that the electron is abstracted from the hydrogen atom. The spectrum obtained by reaction of H atoms with MgO films does not exhibit a distinct doublet pattern, but is clearly asymmetric. This can indicate either g-matrix anisotropy or the presence of unresolved hyperfine splitting. As it will be shown further, no sizable g-matrix anisotropy was observed. To prove that the hyperfine interaction contributes to the asymmetry of the spectrum and to study the interaction of the unpaired electron with hydrogen nucleus, we performed isotopic substitution experiments. Isotopic substitution with D (nuclear spin I = 1) should lead to the replacement of the doublet of lines by a triplet pattern with a smaller separation on the basis of the ratio of the the magnetic moments of the two isotopes ($\mu_H/\mu_D = 6.51$). In our case of unresolved hyperfine splitting, one would expect narrowing of the line. The lineshape of the EPR signals obtained by reaction of the MgO film with hydrogen and deuterium atoms is shown in Fig. 4.27 (black and red curves, respectively). The hydrogen-related line is slightly broader, as expected. Therefore, the spatial proximity between the H^+ and the e is evident from the reduced linewidth when substituting H_2 with D_2 due to a reduction in the unresolved hyperfine interaction.

The EPR resonance position and the indication for the comparable hyperfine splitting are in line with the observations of centers produced by hydrogen treatment on MgO powders [106; 28; 29; 26; 27]. Comparison of the properties of paramagnetic centers produced here by chemisorption of hydrogen atoms on MgO film and centers produced on powders [106; 28; 29; 26; 27] allows us to attribute our EPR signal to the formation of trapped electrons at low coordinated sites with a proton nearby. The loss of distinct hyperfine splitting in our experiment is consistent with previous observations with H atoms adsorbed on MgO powders [113; 46]. We will adopt a nomenclature of F_s^+(H) centers for our species,

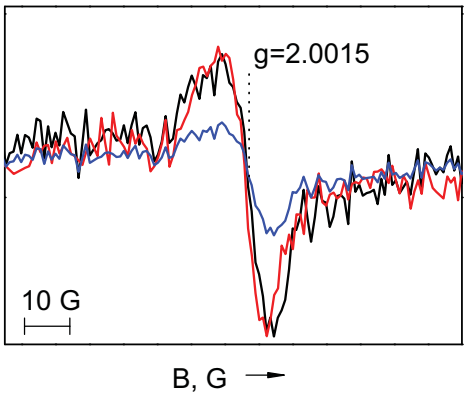

Figure 4.27: EPR spectra of a 20 ML MgO(001) film grown at 600 K, after exposure to hydrogen atoms (black line), and after exposure to deuterium atoms (red line). The blue line shows black line spectrum scaled to 40 %.

although most likely there are differences from the F_s^+(H) centers observed on MgO powders. One of the important facts to mention is that the F_s^+(H) centers obtained by UV irradiation in the presence of hydrogen molecules produces a distinct hyperfine pattern [29; 26; 27]. This can be explained by the fact that F_s^+(H) centers produced by UV irradiation in the presence of hydrogen are well defined species, whereas adsorption of H atoms leads to a distribution of types of F_s^+(H) centers. This leads to the superposition of lines and smearing out of the hyperfine structure.

In order to obtain information about the g-matrix anisotropy of the trapped electron on the surface we performed angular-dependent EPR measurements. To extract g-matrix anisotropy in the surface plane we performed experiments with the magnetic field oriented in the surface plane. Spectra taken with the magnetic field parallel to the [100] and [110] directions of MgO exhibit no change in the lineshape and resonance position. To investigate g-matrix anisotropy, out-of-surface-plane EPR measurements were performed, varying the angle between the surface normal and the magnetic field. We observed minor changes in lineshape and resonance position for the angles between 0 and 90°. Therefore, the g-matrix anisotropy for the system must be small compared to the linewidth, which is consistent with the experimental results and calculations on MgO powder [27].

To obtain additional information on the coordination of the trapped electrons on the surface, isotope substitution experiments with $^{17}O_2$ were performed. The

same approach as in Chapter 4.2.2 will be used. The MgO film was grown with 20% enrichment of $^{17}O_2$. In the present experiment, no signal was observed: neither the original line around the free electron g-value, nor a sextet of lines. If the assumption of the amount of 4-6 oxygen atoms interacting with trapped electron were correct, we would be able to observe the scaled central line (see Fig. 4.27, blue curve). This experiment implies that the assumption that the unpaired electron interacts only with 4 to 6 nearest oxygen atoms is wrong, but does not allow an exact determination of the total number of ions surrounding the trapped electron.

It is worthwhile to compare the properties of trapped electrons created by the different methods. Diffrences between surface trapped electrons created by electron bombardment [121; 116] and Mg-induced surface color centers were discussed in the previous chapter. One has to mention that H generated surface trapped electrons more closely resemble Mg generated ones, rather than the ones created by electron bombardement. At low temperatures all three methods (electron bombardment, Mg additive coloring and H atoms chemisorption) result in quite similar EPR spectra in terms of resonance position (Fig. 4.28). There are, however, differences in the behavior of color centers created by the different methods. First, there is a difference between these preparations in the temperature behavior of the linewidth. At 50 K, the linewidth of electron-generated centers is 6 G, of Mg-induced is 7 G and of H-generated is 9 G. While the Mg-induced and H-generated signals maintain the same linewidth between 50 and 300 K, the electron bombarded system shows a considerable narrowing ($\Delta H_{pp}(300K) \approx 1.3$ G) of the signal at room temperature. The rather large linewidth of Mg-induced and H-generated lines is attributed to inhomogeneous broadening caused by the presence of trapped electrons in a variety of local environments (corner, kink, reversed corner). Another difference between these preparations is the location of the trapped electrons on the surface. In the case of the electron bombarded system it was shown that the majority of the F-centers are located at the edges of the MgO islands [121; 116]. The trapped electrons created by electron bombardment are located in oxygen vacancies which are created through an electron stimulated desorption process [77]. The number of oxygen vacancies present on

the pristine film is very low if present at all, as was shown by high resolution STM measurements [116]. Therefore, it is not reasonable to assume that the Mg-induced and H-generated color centers also represent electrons located in anion vacancies. Instead, EPR signals of Mg-induced and H-generated species are due to electrons trapped at morphological defects of the surface such as kinks or reversed corners. It was shown that a stabilization of electrons is possible at a variety of sites having slightly different local environments, which is reflected in the slightly different g-values for H-generated ones [106; 27], with $g_{||} = 2.0007\text{-}2.0015$, $g_{\perp} = 1.9996\text{-}2.0003$. Within that scheme, a Mg cation as well as a proton has to be stabilized on the surface as well. Generally, the EPR data allows no comments on the fate of non-paramagnetic or not EPR detectable species. Although in the particular case of a proton one can draw some conclusions from the unresolved hyperfine splitting. As was shown in this chapter by isotope substitution experiments, the proton is stabilized in the proximity of the trapped electron. The number of species produced by different methods is approximately the same. For color centers created by electron bombardment one would have expected a larger amount since the amount of sites available for their creation (steps and corners, kinks, etc.) is considerably bigger than for Mg or H created color centers (only corners, kinks, etc.). It was shown by a combination of STM and EPR that at low electron doses singly occupied paramagnetic color centers are mostly formed, whereas at high electron doses the doubly diamagnetic occupied type is dominant, which were found to be more stable [116]. It is suggested that with increasing electron dose the paramagnetic color centers are transformed into diamagnetic ones [116]. Therefore one can explain the similar amounts of paramagnetic color centers created by electron bombardment and by the two other methods by the fact that along with paramagnetic color centers, doubly populated diamagnetic centers are created [116]. The amount of color centers produced by Mg additive coloring and H atoms adsorption is of the same order as the amount of low-coordinated sites (corners, reversed corners) on the MgO film surface as referred from the STM picture.

As seen for the electron bombardement considerable differences in behaviour may be found for films grown at 300 K (and annealed to 1100 K). The EPR

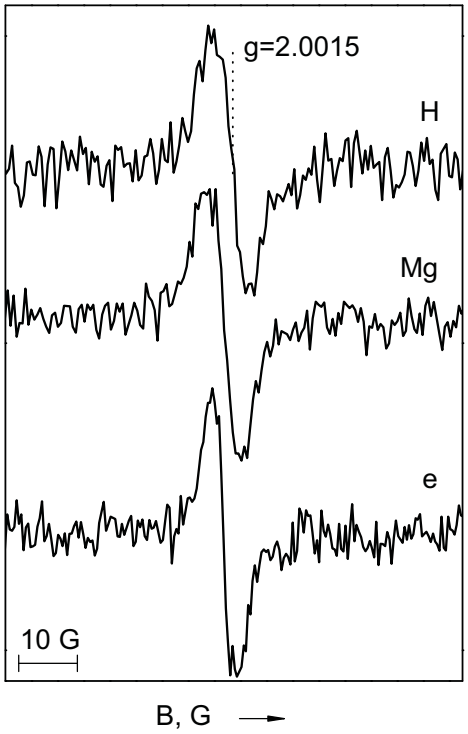

Figure 4.28: EPR spectra of a 20 ML MgO(001) film grown at 600 K after electron bombardment (lower spectrum), deposition of small amounts of Mg at 50 K (second spectrum) and exposure to hydrogen atoms (upper spectrum). The spectra were normalized by amplitude and recorded at T = 50 K.

spectrum taken after the interaction of H atoms at 100 K with the film grown at 300 K and annealed to 1100 K is shown in Figure 4.29 (red line). One can see a single asymmetric EPR resonance line around the free spin value ($g_e = 2.0023$) with a linewidth of 9 Gauss at 50 K. The linewidth remains constant between 50-300 K. The amount of spins is estimated to be $8\pm2 \times 10^{12}$ cm^{-2}. These paramagnetic centers observed by EPR are only partially (around 30 %) located on the surface of the MgO film as verified by an incomplete quenching of the EPR signal upon adsorption of molecular oxygen at 50 K. The amount of surface species is consistent with the amount of surface paramagnetic centers produced on MgO films grown at 600 K. The centers disappear upon annealing to 900 K. The signal position near the free-electron g-value and the lack of the resolved hyperfine splitting expected for hydrogen atoms indicates that the electrons are abstracted from the H atoms. However, the electrons remain close to the protons as the EPR line narrows upon exchanging hydrogen with deuterium. In Chapter 4.2.2 it was shown that MgO films grown at room temperature are able to trap electrons in dislocation lines. Therefore we will attribute bulk paramagnetic centers appearing upon adsorption of atomic hydrogen to unpaired electrons trapped at dislocation lines with protons stabilized nearby. Comparing the EPR signal intensity with the concentration of surface line defects as obtained from the STM measurements [13], it was found that there are 0.5 electrons per nanometer of line defect. This is almost an order smaller that the amount of electrons one can trap in dislocation lines by electron bombardement. The influence of the hydrogen dose on the EPR signal intensity was studied [67]. Varying the dosage from 4 and 400 L, it was observed that the signal intensity, starting with zero at zero hydrogen dose, passes through a maximum and then decreases again for higher doses. It was suggested that the paramagnetic species which are formed at low hydrogen doses are transformed into diamagnetic species if more hydrogen atoms are absorbed by the film, but desorption of molecular hydrogen can not be excluded. It was also studied how deeply atomic hydrogen diffuses into the grain boundary, therefore the measurement was performed with films of different thicknesses. Ultra-thin films (4 monolayer) showed no EPR signal upon H atom adsorption, which can be explained by electrons being drained into the Mo crystal, as in the case of

the electron bombardment described in Chapter 4.2.2. Films of 8 monolayer thickness gave a signal of about the same intensity as 20 ML thick films, so we can conclude that approximately the first five layers of all films do not contribute to signal intensity. Therefore, it is reasonable to assume that the number of layers that can provide electron traps is effectively more than doubled when increasing the thickness from 20 to 40 monolayers, although the increase of EPR signal intensity was shown to be only 17 % [67]. It was suggested that on the one hand a limited number of layers under the surface contributes to the signal, but on the other hand the concentration of dislocation lines at the surface was found to decrease with film thickness [31; 11]. So for a limited diffusion length, one would expect the signal intensity to decrease. One has to mention that the spectra were taken at the same hydrogen dosage and it is possible that higher intensities could be reached for different doses.

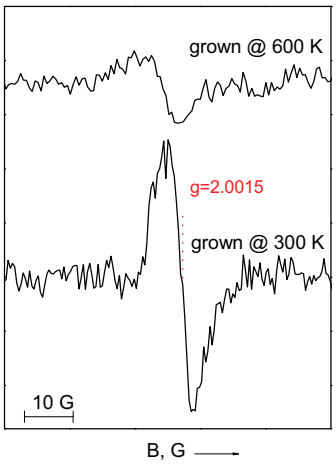

Figure 4.29: EPR spectra of a 20 ML MgO(001) film grown at 300 K and annealed to 1100 K (lower curve) and grown at 600 K (upper curve) after hydrogen atom exposure. The spectra were recorded at T = 50 K.

4.5.3 Conclusions

EPR experiments have shown the possibility to produce surface excess electrons on single-crystalline MgO(001) thin films grown at 600 K by contact with hydrogen atoms at 100 K. The unpaired electron is trapped close to the hydrogen nucleus, as shown by isotope-substitution experiments. The amount of trapped

electrons is estimated to be 2-3 $\times 10^{12}$ cm^{-2}, and they are stable up to 600 K. Adsorption of H atoms on the MgO films grown at 300 K with subsequent annealing to 1100 K results in both surface trapped electrons and electrons trapped at dislocation lines. The amount of paramagnetic centers is around 8 $\times 10^{12}$ cm^{-2} and they are stable up to 900 K.

Chapter 5

Oxygen radicals on MgO(001)/Mo(001) films

5.1 O_2^- radicals on ultrathin MgO films

5.1.1 Motivation

One of the important goals in catalysis research is to tune activity and selectivity of catalysts. Identification of parameters which contribute significantly to the performance of catalysts is one of the key issues in achieving this goal. For bulk-like oxides, some of the factors influencing the reactivity are oxide termination or surface defects [37]. In the case of MgO, the stoichiometric (100) surface is generally believed to be relatively inactive with respect to chemical reactions, and the chemistry occurring on such surfaces is driven by defects [37]. For ultrathin films, this presumption may not hold, as the reactivity may be altered by film thickness. The idea that the supporting metal may influence the properties of adsorbates and thus their reactivity has been around since the late 1940s. Cabrera and Mott [19] discussed whether electron tunneling through the growing oxide film during oxidation of a metal surface controls the oxidation rate via charge transfer towards the adsorbed species. Vol'kenshtein [134] also developed ideas that semiconducting oxide films of a few monolayer in thickness might be used to control electron transfer to adsorbates and render them catalytically active. Recently, the reactivity of ultrathin films has attracted attention, for instance

altered properties for metal deposits as well as molecular adsorbates were predicted [102; 57]. For example, it was first theoretically suggested [102] and then later experimentally verified [118; 119] that gold deposits will become negatively charged when adsorbed on ultrathin MgO films grown on Mo or Ag. Along the same line, it was recently shown that charging of adsorbates plays a key role in understanding CO oxidation on a monolayer thick FeO(111) film grown on Pt(111) [125]. In this case, the crucial initial step is an activation of molecular oxygen on the surface. In Figure 5.1, the energy diagram for interaction of O_2 with the FeO/Pt(111) film is shown. Oxygen has to overcome a small energy barrier (0.3 eV) to become chemisorbed molecularly with an adsorption energy of 0.7 eV. In the transition state, when it is overcoming the barrier, there are indications that it is in a metastable O_2^- state [99]. In the chemisorbed state, adsorbed O_2 becomes peroxo species, O_2^{2-}. The electron transfer to the oxygen is enabled mainly by structural changes in the oxide film. The activated peroxo species is a precursor along a dissociative pathway, which results in the formation of an O-Fe-O trilayer structure of FeO_2 stoichiometry. Next the CO oxidation reaction involves extraction of an oxygen atom from the trilayer film to form a CO_2 molecule. Key to the reactivity of the film is its ability to activate molecular oxygen by consecutive electron transfer reactions. This raises the question of whether this mechanism may also be found on other systems or if there is the possibility to find experimental evidence for the formation of the activated molecular oxygen species. For the FeO/Pt(111) system, such evidence is rather diffcult to obtain as the first step is an activated process with the O_2^- as a methastable species which renders its observation difficult. However, on different oxides these species might be more stable intermediates. Theoretical calculations have suggested such a scenario on ultrathin MgO films [61; 43]. Theory predicts the spontaneous formation of an O_2^- species upon adsorption of molecular oxygen on the surface of ultrathin MgO films (see Figure 5.2 for silver substrate). On MgO/Ag(100) there is no barrier for molecular oxygen adsorption, it becomes chemisorbed with an adsorption energy of 0.8 eV [61]. The O_2 molecule is centered above two adjacent Mg^{2+} cations of the surface (Figure 5.3). On the Mo substrate these O_2^- species were predicted to adsorb more strongly (1.5 eV) [43]. Next, CO adsorbs on the

MgO/Ag surface with an adsorbtion energy of 0.4 eV, and after overcoming a small (0.7 eV) barrier, CO_2 is formed from adsorbed CO and O_2. The aim of this study is to provide experimental evidence for the formation of O_2^- radicals upon adsorption of molecular oxygen on an ultrathin MgO film.

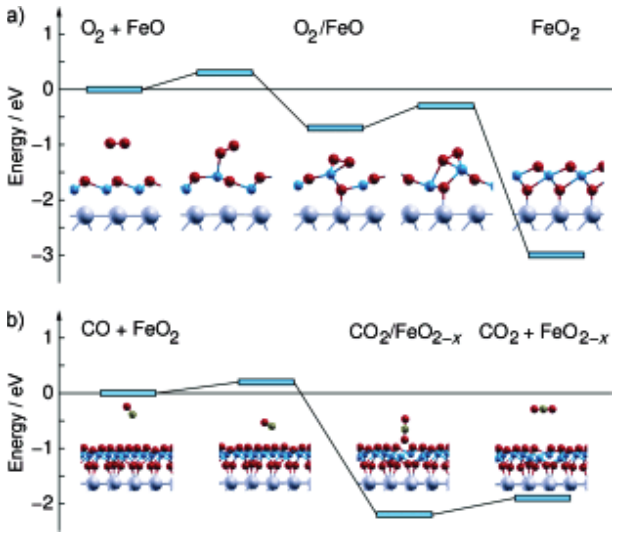

Figure 5.1: Energy diagram for CO oxidation over FeO(111)/Pt(111). Atomic color code: blue (Fe), red (O), and gray (Pt). Picture adapted from ref. [125].

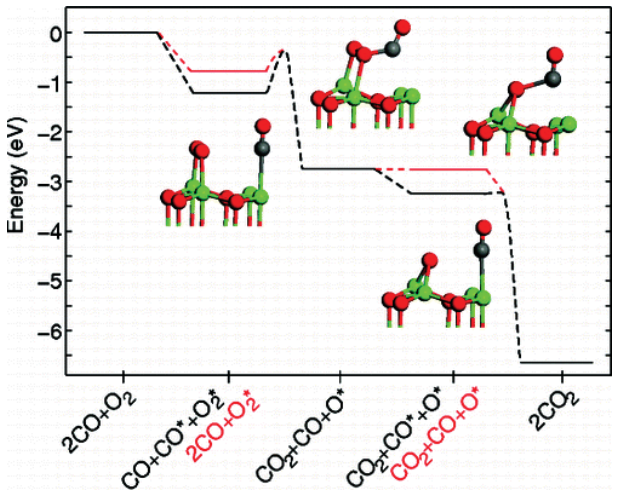

Figure 5.2: Enthalpy diagram for CO oxidation over MgO/Ag(100). Atomic color code: green (Mg), red (O), and gray (C). Picture adapted from ref [61].

5.1.2 Results and Discussion

First, we will discuss the adsorption of molecular oxygen on films grown at 600 K. The upper curve in Figure 5.4 shows an EPR spectrum obtained after adsorbing 20 Langmuir of molecular oxygen at 40 K on a 4 ML thick MgO(001) film. The

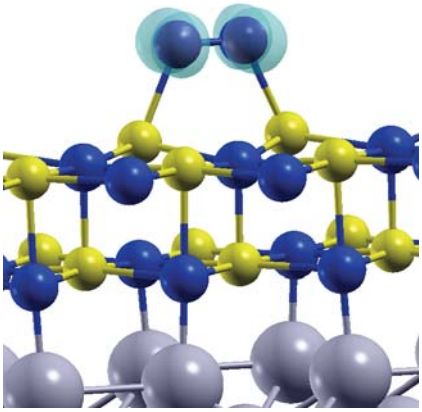

Figure 5.3: Adsorption geometry of molecular oxygen on an ultrathin MgO(001) film. Picture adapted from ref. [52].

magnetic field was oriented in the surface plane, collinear with a [100] equivalent direction. The spectrum consists of a single line localized at a g-value of 2.037. For O_2^- species on MgO powders, two g-matrix (g_{xx}, g_{yy}) components were found at around 2.0023 and 2.007, while the third one (g_{zz}) varies between 2.062-2.091 for different surface sites [25; 101; 34]. The signal position observed here is in the range expected from the principal components of the g-matrix formed on powders. On the other hand, it does not correspond to one of the prncipal g-matrix components, thus one expects a significant dependence of the line position on the angle between the surface and the magnetic field.

The EPR signal appearing upon O_2 adsorption is only observed for ultrathin MgO/Mo films. In Figure 5.5 one can see the intensity of EPR signal as a function of MgO film thickness. Increasing the film thickness from 4 ML to 8 ML results in a reduction of the signal intensity by 50% and above 15 ML no signal is found. Rather slow decrease of the signal intensity with thickness can be explained by the fact, that the film thickness can slightly vary from the nominal thickness in different areas of the film. In addition, the species were found to be stable upon annealing up to approximately 350 K, in agreement with theoretical prediction [43].

One can rationalize the spectrum containing one line in Fig. 5.4 by looking at the adsorption geometry as predicted by theory (Figure 5.6). It is seen that the molecules are expected to be oriented with their main axes along the [110] equivalent direction of the MgO(001) surface. As the orientation of the g-matrix adopts the symmetry of the problem, it is evident that one of the matrix com-

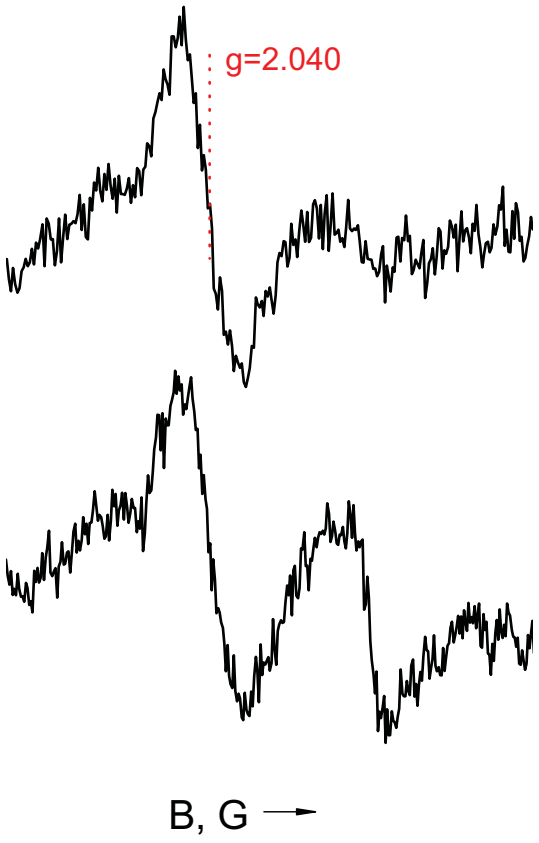

Figure 5.4: EPR spectra after a 20 Langmuir exposure of molecular oxygen at 40 K on 4 ML thick MgO(001) films grown at 600 K (upper curve) and at 300 K with subsequent annealing to 1100 K (lower curve).

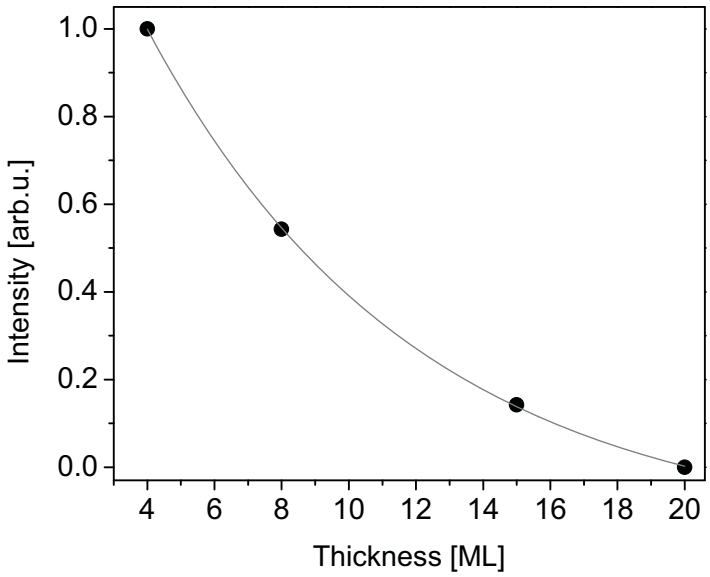

Figure 5.5: Intensity of the EPR signal as a function of MgO film thickness.

ponents is parallel to the long axis of the molecule, one is pointing perpendicular to the surface, and the third one is orthogonal to the former two. For O_2^- radicals, the three directions are labeled z, y, and x, respectively. In the case that the theoretically predicted adsorption geometry is correct, the spectrum shown in Figure 5.4 would allow determination of the average of z and x components of the g-matrix. To prove the azimuthal orientation of the molecule, an additional experiment is required. Given the symmetry of the surface one can see from the sketch in Figure 5.7 that a rotation of the magnetic field in the surface by 45° (along a [110] equivalent direction) would render the two molecules magnetically inequivalent, therefore it will be possible to determine the two components of the g-matrix. Figure 5.8 shows the corresponding spectrum. It consists of a doublet of lines localized at g-values of 2.072 and 2.002, respectively, as expected from the considerations mentioned above.

In addition to the spectrum taken with the magnetic field oriented in the surface plane, angular dependent spectra for different polar angles are reported in Figure 5.9. The magnetic field was oriented in the plane spanned by the direction equivalent to [100] and the surface normal. The angular dependence reveals a simple $\cos^2$ dependence with the extreme values found at 90° and 0°, respec-

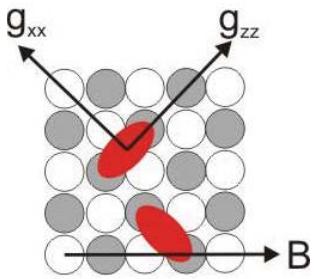

Figure 5.6: Top view of the adsorption geometry (O_2^- are depicted as ovals). The magnetic field is oriented in the surface plane collinear with a [100] equivalent direction.

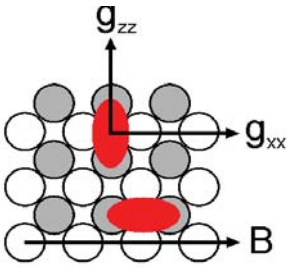

Figure 5.7: Top view of the adsorption geometry (O_2^- are depicted as ovals). The magnetic field is oriented in the surface plane collinear with a [110] equivalent direction.

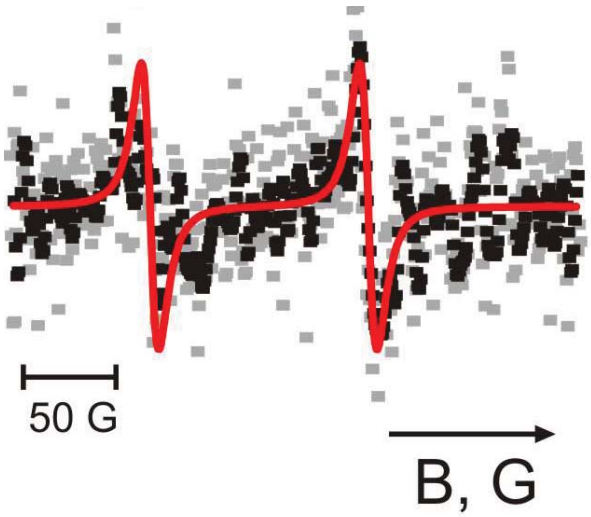

Figure 5.8: EPR spectrum after 20 Langmuir exposure of molecular oxygen at 40 K on a 4 ML thick MgO(001) film. The magnetic field was oriented in the surface plane collinear with a [110] equivalent direction.

tively. This allows us to determine the orientation of the matrix. Two matrix components are oriented in the surface plane and the two orthogonal components are aligned to the [110] equivalent directions, the third component is oriented perpendicular to the surface. Thus, the values of the g-matrix components can be directly extracted from the spectrum in Figure 5.8 and the topmost spectrum in Figure 5.9 to be $g_{xx} = 2.002$, $g_{yy} = 2.012$, $g_{zz} = 2.072$.

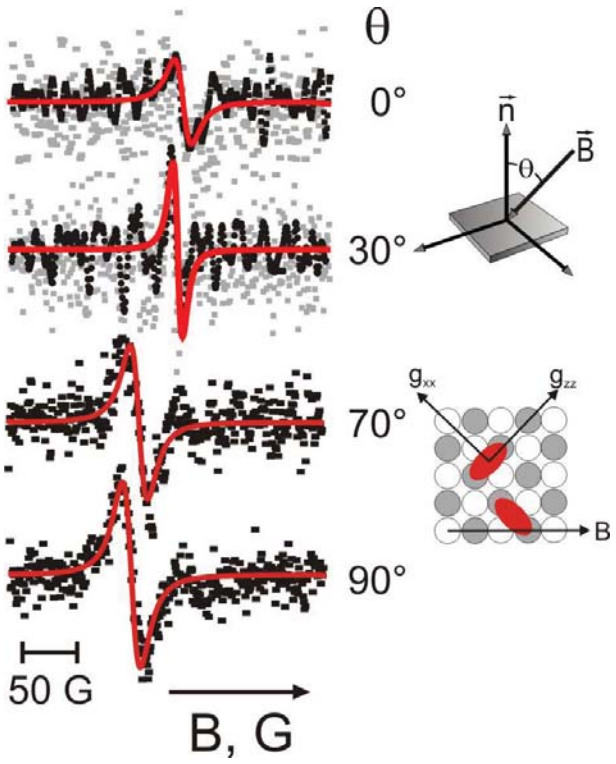

Figure 5.9: EPR spectra after 20 Langmuir exposure of molecular oxygen at 40 K on a 4 ML thick MgO(001) film as a function of polar angle θ. The magnetic field was oriented in the plane spanned by the direction equivalent to [100] and surface normal.

The g-matrix components measured here will be compared to values found for O_2^- radicals on the terraces of MgO powders, which were prepared by chemical means [92], and are given in Table 5.1. The x-component is unchanged, the y-component of the matrix is slightly decreased while a significantly larger z-component is found on powders. Understanding these differences requires a detailed understanding of the electronic structure, which was addressed by means of theory [52]. To investigate these differences a calculation of the g-matrix was performed [52] for an O_2^- radical adsorbed on a pure MgO cluster model, representing a (001) surface. The calculated g-matrix components as well as the geometry, which was obtained after optimizing this model, are shown in Ta-

ble 5.1. As expected for charged molecules, the oxygen bond length is elongated as compared to the neutral molecule. When comparing the calculation to the measurement on the powder, it is readily seen that the x component of the matrix is well reproduced, the y component is slightly overestimated while the g_{zz} component is considerably underestimated. Detailed studies have shown that the g_{zz} component is systematically underestimated in all calculations of O_2^-species [92]. However, trends such as that found when comparing the O_2^- radicals adsorbed on terrace and edge Mg^{2+} sites of MgO, which reveals a reduction of the g_{zz} component with decreasing coordination number, are well reproduced by theory. The model used so far for the thin film describes the situation where the main stabilization effect of the thin film, namely the polaronic distortion of the lattice, is absent. Polaronic distortion is a structural change of the film which is induced by the presence of the charged oxygen molecule on the surface. This distortion is only possible for ultrathin films of a few ML thickness. A calculation using a MgO cluster with a geometry which exhibits a significant polaronic distortion as found for a metal supported thin oxide film, indeed, reveals a sizable reduction of the g_{zz} component while the other two g-matrix components are only slightly modified, shown in Table 5.1. The change in g_{zz} is in line with a simple physical picture: the polaronic distortion will effectively increase the electric field which the radical is exposed to. The resulting increased electric field gives rise, in turn, to an increase of the energy difference between the π x and y orbitals of the oxygen radical. The shift of the g_{zz} component away from the free electron value is given by [69]

$$g_{zz} = g_e + 2[\lambda^2/(\lambda^2 + \Delta^2)]^{1/2}$$

with λ being the spin orbit coupling constant and $\Delta = 2\pi_g^y - 2\pi_g^x$. Therefore the increase of Δ due to the increased electric field will lead to the expected reduction in the g_{zz} component. In turn, the observed reduction of the g_{zz} component for the thin film can be interpreted to be a result of the polaronic distortion of the thin film.

In Chapter 4.3.2 the properties of MgO films grown at 600 K have been discussed. In particular, it was shown that Mo ions are present on the surface, therefore they may contribute to the reactivity of the film. To find out whether

Table 5.1: Measured and computed g-matrices for O_2 adsorbed on the surfaces of MgO/Mo(001) films and MgO powders.

	g_{xx}	g_{yy}	g_{zz}	d(O-Mg), Å	d(O-O), Å
MgO/Mo(001) (this work) Terrace	2.002	2.012	2.072	-	-
MgO powders [101] Terrace	2.002	2.008	2.091	-	-
MgO powders [25] Edge	2.002	2.008	2.077	-	-
MgO(001) theory [92] [(a)] Terrace	2.0022	2.0092	2.0639	2.329	1.345
MgO(001) theory [92][(a)] Edge	2.0021	2.0096	2.0527	2.158	1.353
MgO(001) theory [52] Terrace	2.0025	2.0093	2.0560	2.075	1.345

(a) Notice that in ref. [92] a different axis nomenclature convention is adopted for the orientation of the axes.

the formation of the O_2^- radicals described above is not related to the presence of Mo ions, the experiments were reproduced on films lacking Mo ions (see Chapter 4.2.2). In particular, molecular oxygen was adsorbed on films that were grown at 300 K and annealed to 1100 K. The lower curve in Figure 5.4 shows an EPR spectrum obtained after adsorbing 20 Langmuir of molecular oxygen at 40 K on a 4 ML thick MgO(001) film. The magnetic field was oriented in the surface plane collinear with a [100] equivalent direction. The spectrum consists of two lines: one symmetric line localized at a g-value of 2.037, another asymmetric line at g-value of 2.013. The second line is absent at the spectrum obtained after adsorbing molecular oxygen on the film grown at 600 K (see upper curve in Figure 5.4). The temperature stability of these two species was found to be different: the line at 2.037 disappears around 350 K (as it was found for O_2^- species on MgO film grown at 600 K), while the line around 2.013 is stable up to 600 K. The fact that the temperature stability of these two lines is different shows that the two lines do not correspond to the same species. On the contrary, they belong to different species. The line at g-value of a 2.013 can be the result of the presence of several oxygen radicals [128; 139; 120; 32; 103; 30]. These may be O_2^- species with different orientations on the surface. One can envision that on certain surface sites molecular oxygen can be dissociated and form O^-. On MgO powders, the g-matrix for O^- species had one component around the free electron g-value and two others between 2.0505-2.0186. Finally, O^- can react with O_2 and form O_3^-, which has one g-value around 2.0014 and two others around 2.018. The asymmetry of the line indicates the presence of several underlying components. Spectra taken with the magnetic field parallel to the MgO [100] direction and the MgO [110] direction

exhibit a change in the lineshape, but no significant shift. Angular-dependent measurements varying the angle between surface normal and the magnetic field show changes in the lineshape. This indicates g-matrix anisotropy, but information on the location of the species on the surface can not be disentangled in the X-band EPR experiment. The transformation of the lineshape of the line around 2.013 can be observed as well for different MgO film thicknesses as shown in Figure 5.10. It is rather broad and less intense than the line around 2.037 at a thickness of 1 ML, it gets more intense at 3 ML. At a thickness of 8 ML it becomes rather sharp and more intense than the line around 2.037. On the film of 15 ML there is a small indication of the presence of the line around 2.013. Most likely the line at a g-value of 2.013 is the result of a mixture of species. These can be O_2^- located at dislocation lines which are absent for films grown at 600 K, as well as O^- originating from cleavage of O_2 and O_3^-. These experiments have shown that the same O_2^- species can be produced on the MgO films grown at 300 K as on the films grown at 600 K. This means that the presence of Mo ions on the latter films is not influencing the O_2^- formation.

5.1.3 Conclusions

In summary, the results presented here are the first unambiguous proof for the spontaneous activation of molecular oxygen forming an O_2^- radical upon adsorption on a stoichiometric low energy oxide surface, using MgO(001). Theory [52] predicts that the surface can activate oxygen molecules by a charge transfer leading to an O_2^- radical which is stabilized by polaronic distortions of the MgO lattice. The latter distortion is only feasible for ultrathin films of a few ML thickness. Despite a lack of quantitative agreement, in particular with respect to the g_{zz} component, the comparasion with theoretical calculations allows us to associate the reduction of the g_{zz} component observed on the thin film relative to that on MgO powder to the polaronic distortion of the thin MgO film. Hence, these results provide the first experimental evidence for the presence of the polaronic distortion, predicted by theory to be a crucial ingredient for understanding the properties of these thin film systems.

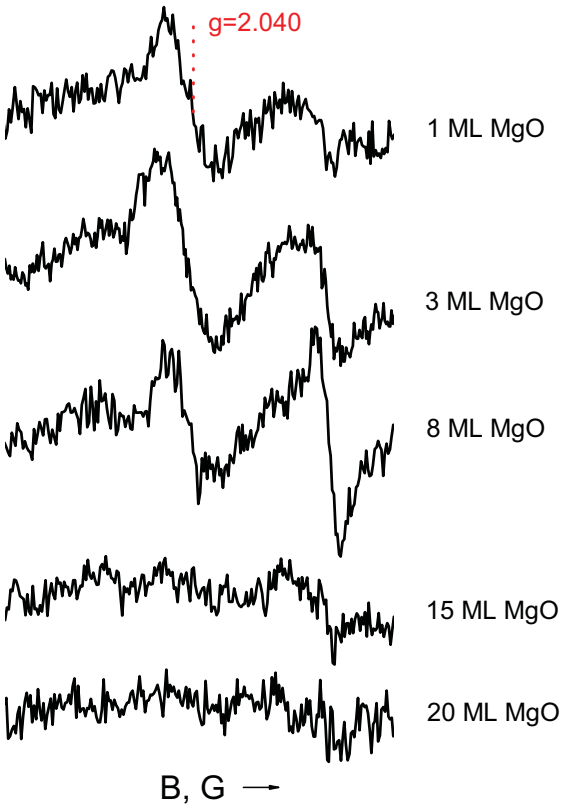

Figure 5.10: EPR spectra after 20 Langmuir exposure of molecular oxygen at 40 K on MgO(001) films with different thickness as indicated. The films were grown at 300 K and annealed to 1100 K.

5.2 O^- radicals on thin MgO films

5.2.1 Motivation

Li doped MgO is of interest as a potential catalyst for the oxidative coupling of methane. The underlying reaction mechanism is still not understood and the proposed mechanism debated [86]. The key process was thought to be hydrogen abstraction from methane by O^- species, created by Li doping with subsequent formation of Li^+O^- ion pairs. In recent work it was shown that Li^+O^- centers are not stable in Li doped MgO thin films [91]. Nonetheless, it is important to determine the properties of O^- species. However, different strategies need to be followed to prepare these centers. The purpose of this chapter is to present experimental evidence for the creation of O^- ions on a MgO film surface and to provide some experimentally determined properties.

O^- ions on the surface of MgO powders were studied from the early 70s and were claimed to have "undoubtedly the most controversial EPR spectrum in surface studies" [139]. One of the methods of O^- generation was based on the reaction of nitrous oxide with surfaces containing one-electron centers. The electron is transfered to the N_2O molecule which decomposes into O^- remaining on the surface and desorbing N_2:

$$e_s^- + N_2O \rightarrow O_s^- + N_2.$$

For one-electron centers on the MgO surface, $F_s^+(H)$ centers were used [128; 140; 103]. The above mentioned complexity of the EPR spectrum of surface O^- ions is the result of a remarkable variety of species which in turn is the result of a variety of structurally different surface electron traps [30]. Another method, which results in the formation of a single type of O^- species, are X-ray [32] or UV light [120] irradiation:

$$O_s^{2-} + h\nu \rightarrow O_s^- + e_s^-.$$

The later method results in rather well defined O^- species.

In this chapter we are going to show by the means of EPR that O^- centers

on the surface of thin single-crystalline MgO(001) films can be produced by the reaction of N_2O molecules with F_s^+ centers. These F_s^+ centers are oxygen vacancies with one trapped electron. The first step in O^- creation is the production of F_s^+ centers by electron bombardment:

$$\begin{array}{ccccccccccccc} \mathrm{O} & \mathrm{Mg} & \mathrm{O} & \mathrm{Mg} & \mathrm{O} & & \mathrm{O} & \mathrm{Mg} & \mathrm{e^-} & \mathrm{Mg} & \mathrm{O} \\ \mathrm{Mg} & \mathrm{O} & \mathrm{Mg} & \mathrm{O} & \mathrm{Mg} & \xrightarrow[-\mathrm{O}^{2-}]{\mathrm{e^-}} & \mathrm{Mg} & \mathrm{O} & \mathrm{Mg} & \mathrm{O} & \mathrm{Mg} \end{array}$$

The second step is exposure of the surface to N_2O:

$$\begin{array}{ccccccccccccc} \mathrm{O} & \mathrm{Mg} & \mathrm{e^-} & \mathrm{Mg} & \mathrm{O} & & \mathrm{O} & \mathrm{Mg} & \mathrm{O^-} & \mathrm{Mg} & \mathrm{O} & & \\ \mathrm{Mg} & \mathrm{O} & \mathrm{Mg} & \mathrm{O} & \mathrm{Mg} & \xrightarrow{\mathrm{N_2O}} & \mathrm{Mg} & \mathrm{O} & \mathrm{Mg} & \mathrm{O} & \mathrm{Mg} & + \mathrm{N_2}\uparrow \end{array}$$

5.2.2 Results and Discussion

First, the formation of the O^- ions on MgO films grown at 600 K will be discussed. In agreement with previous results [121; 116], after electron bombardment of a 20 ML thick MgO(001) film a single symmetric line around the free electron g-value appears (trace a in Fig. 5.11). The color centers created by electron bombardment react immediately with N_2O adsorbed on the surface at 40 K (trace b in Fig. 5.11). The single line characteristic for F_s^+ centers is replaced by a two-line structure with components around g=2.002 and g=2.045. The intensity of these two lines is about the same as obtained by double intergation. There is also an indication of the presence of a small component around g=2.023. The intensity of this component is ten times smaller. In this experiment the magnetic field direction was perpendicular to the surface normal and was oriented in the surface plane collinear with a MgO [100] equivalent direction. The species were found to be stable upon annealing up to approximately 300 K. These paramagnetic centers observed by EPR are located on the surface of the MgO film as verified by a complete quenching of the EPR signal upon adsorption of molecular oxygen at 40 K. As in the previous chapters, to estimate the number of paramagnetic species, the signal obtained here was compared to spectra measured for Au atoms deposited at low temperatures [143]. The amount of spins is around $6\pm2 \times 10^{12}$ cm^{-2}, approximately the same amount as the initially created F_s^+ centers.

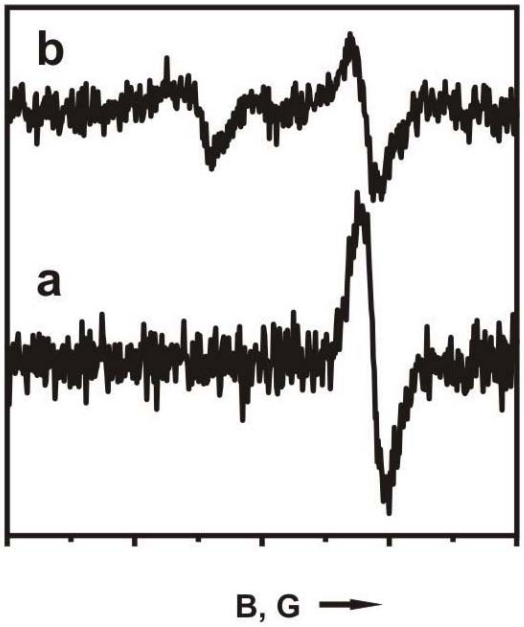

Figure 5.11: EPR spectrum of a 20 ML MgO(001) film grown at 600 K after electron bombardment (single line around g = 2.002) (a), after electron bombardment with subsequent exposure to nitrous oxide at 40 K (two lines around g = 2.005, 2.043) (b). The magnetic field direction was perpendicular to the surface normal (MgO [001]) and oriented parallel to MgO [100]. The spectra were recorded at T = 40 K.

The signal positions are in line with the expectations for O^- species on MgO. The g-matrix for O^- species on MgO powders had one component around the free electron g-value and two others ranging from 2.0505 to 2.0186 [128; 139; 120; 32; 103]. The g factors expected from the configuration $p_x^2 p_y^2 p_z^1$ have been obtained for the situation in which the degeneracy of the p functions is lifted by an orthorhombic crystal field so that p_z lies at an energy E above the mean of p_x and p_y whose separation is Δ (see Fig. 5.12) [128]. Such an ion should have two principal g factors $> g_e$ and the third one $< g_e$ [128].

In order to obtain information about the principal g-matrix components and its orientation with respect to the MgO surface, angular-dependent EPR measurements were performed. The magnetic field direction was varied in a plane spanned by the surface normal and the [100] equivalent direction of MgO (Fig. 5.13). The spectra vary as a function of angle as expected for species on a well defined single crystalline surface. Based on the location of the F_s^+ centers, the O^- species are expected to be located on the edges of MgO island [121; 116]. One has to mention that the minor third line around g=2.023 is consistent with O^-

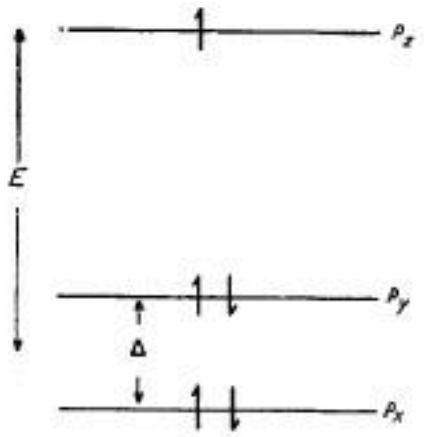

Figure 5.12: Energy levels for $p_x^2 p_y^2 p_z^1$ when degeneracy of p functions is lifted by an orthorhombic crystal field. Picture adapted from [128].

located on the corners, since the number of corner atoms among perimeter atoms is about 20 % and this number is comparable with the relative intensity of the line. For O^- located on edges (see Fig. 5.14 (c)), one of the matrix components is parallel to the edges of MgO islands (labeled z), another one has an angle ϕ with the surface normal (labeled x) and the third one is orthogonal to the former two (labeled y). Due to the four fold symmetry of the surface, two classes of magnetically inequivalent molecules are expected (see Fig. 5.14 (a)). Half of them have the z component of the g-matrix oriented parallel to the magnetic field direction, half of them have their z component perpendicular to the magnetic field. Then the experimental lines are the superposition of the spectra from these two orientations. One can fit the experimental data using Eq. 2.23, where g_{xx}, g_{yy}, g_{zz} and the angle between the x axis and surface normal are unknown variables. The following values have been obtained: g_{xx}=2.0346, g_{yy}=2.0072, g_{zz}=2.0459 and the angle around 8°. However, the obtained parameters are only consistent with this geometry, but they are not unique. So far we have been probing only the polar g-matrix anisotropy out of the surface plane. To study the g-matrix anisotropy in the surface plane, an additional experiment is required. Given the symmetry of the surface, it can be seen from the sketch in Fig. 5.14 b that rotation of the magnetic field in the plane of the surface by 45° (along a [110] equivalent direction) would render the two molecules indistinguishable by means of EPR spectroscopy. Thus, a single line would be expected in the EPR spectrum. Fig. 5.15 shows the

corresponding spectrum. Indeed, only a single line is observed, which is located at g = 2.023 as expected from the considerations mentioned above. There is no line observed around the free electron g-value, which means that all surface color centers are quenched by nitrous oxide adsorption. The line observed here is consistent with the data for the g-matrix principal values and tilting angle obtained from the fitting. Changing the angle between the surface normal and magnetic field direction by only 10 degrees makes the spectrum so broad that we cannot observe the line any more. The obtained g-matrix principal components are in line with the O^- species observed on MgO powder and expected in orthorombic environement.

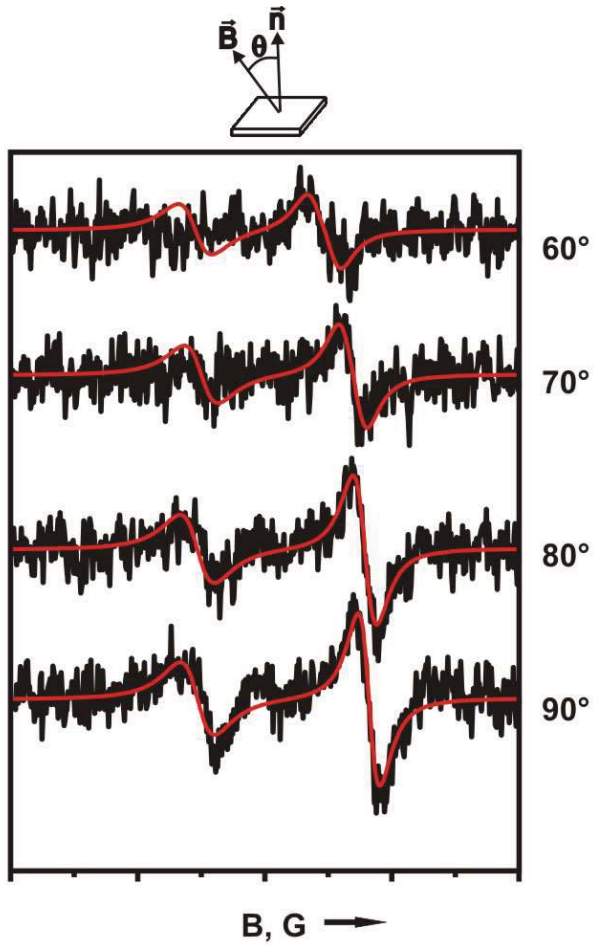

Figure 5.13: EPR spectra taken for O^- on a 20 ML MgO(001) film grown at 600 K as a function of the angle θ between the surface normal (MgO [001]) and magnetic field direction. The magnetic field was oriented parallel to MgO [100]. The spectra were recorded at T = 40 K.

In Chapter 4.3.2 it was shown that Mo ions are present on the surface of MgO films grown at 600 K. It is possible that they may contribute to the reactivity of

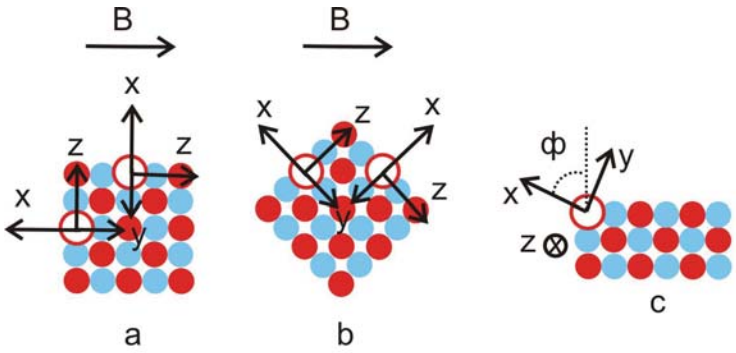

Figure 5.14: Schematic orientation of the g-matrix with respect to the MgO film surface. a) top view with B || [100], b) top view along the [100] direction, c) side view along the [100] direction.

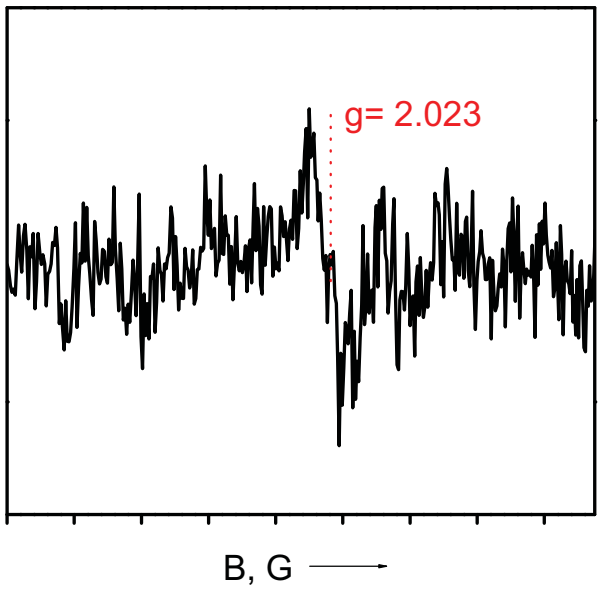

Figure 5.15: EPR spectrum (single line around g = 2.023) taken for O^- on a 20 ML MgO(001) film grown at 600 K. The magnetic field direction was perpendicular to the surface normal (MgO [001]) and was oriented parallel to MgO [110]. The spectrum was recorded at T = 40 K.

the film. To elucidate whether the formation of the O^- species described above is related to the presence of Mo ions, the experiments were reproduced on films grown at 300 K lacking Mo ions (see Chapter 4.2.2). As discussed in Chapter 4.2.2, electron bombardment leads to a single line close to the free electron g-value. From the experiments with molecular oxygen it is known (see Chapter 4.2.2), that around 10 % of the paramagnetic species are on the surface, and the rest are located in the bulk. After adsorption of nitrous oxide on the electron bombarded film (see Fig. 5.16, black line), the intense line around the free electron g-value becomes depleted by 5-10% and the line around g=2.045 appears. The position and intensity of the line around g=2.045 is the same as on MgO films grown at 600 K. It is not possible to make any conclusions about the second line, since it is overlapping with the huge bulk signal located at the same position in the spectrum. However, the decrease of the line provides evidence that the surface contribution is present beneath the bulk signal at g = 2.0023. The red line in Fig. 5.16 shows the spectrum of the O^- species produced on MgO grown at 600 K for comparison. One can conclude that O^- species can be produced on MgO films grown at 300 K as well, and the amount is expected to be comparable. This means that Mo ions present on the surface of MgO films grown at 600 K are not contributing to the formation of O^- species. In turn, it also provides additional evidence that the F_s^+ centers are not influenced by Mo ions either.

5.2.3 Conclusions

We have shown the possibility to produce O^- centers on single crystalline MgO(001) thin films by reaction of nitrous oxide with surface paramagnetic color centers. The amount of the O^- centers is estimated to be $6\pm2\times 10^{12}$ cm^{-2} and they are stable up to 300 K. Angular-dependent EPR spectra show that O^- radicals on MgO films are predominantly located on edges of MgO islands. The orientation of the g-matrix axis on the surface is as follows: the z axis of the g-matrix is oriented along MgO [100] equivalent direction, the x axis is tilted 8 degrees from the surface normal, and the y axis is perpendicular to both of them. The following g-values have been obtained: g_{xx}=2.0346, g_{yy}=2.0072, g_{zz}=2.0459.

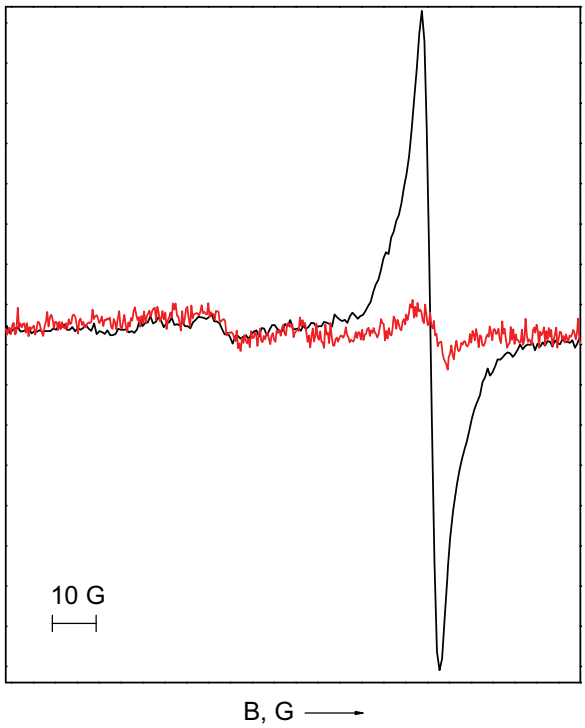

Figure 5.16: EPR spectrum taken for O^- on a 20 ML MgO(001) film grown at 600 K (red line) and at 300 K with subsequent annealing to 1100 K (black line). The magnetic field direction was perpendicular to the surface normal (MgO [001]) and was oriented parallel to MgO [100]. The spectra were recorded at T = 40 K.

Chapter 6

Summary

> I have not failed. I've just found 10000 ways that won't work.
>
> Thomas A. Edison

The aim of this work was to study surface paramagnetic species on single crystalline MgO(001) films using electron paramagnetic resonance (EPR) spectroscopy, which is a useful technique to determine the geometric and electronic properties of paramagnetic species. Despite the fact that EPR allows for studying paramagnetic species, which are difficult to probe by other surface science techniques, on single crystalline surfaces the technique is rarely used, mainly because of its lack of an inherent surface sensitivity.

In the first part of this work, paramagnetic defects on single crystalline films were studied. Defects intrinsic to the films and originating from the film growth were examined. It was shown by means of EPR that a single line appears near the free electron g-value upon the growth of MgO films at 300 K, and which could be attributed to electrons trapped at grain boundaries present in MgO films. Annealing the film to 1100 K quenches the signal due to rearrangements of the film. Hovewer, trapping sites for electrons do not disappear after the structural rearrangements. Instead, subseqent electron bombardment of the annealed film results in the appearance of EPR line located very close to the one of the pristine film. Again the species are located in the bulk of the film. More precisely combination with other experimental results suggests that the signal originates

from trapped electrons in screw dislocations of MgO films. Growing the film at higher temperatures (600 K) leads to smaller amounts of line defects and improved film ordering. On the other hand, a new signal associated with Mo^{5+} ions on the surface of MgO(001) films appears. The Mo^{5+} ions are shown to be present not only on ultrathin films, but also on thick ones and are shown to be reactive species. In light of the aim of this study, namely the the characterization of paramagnetic defects, these intrincic defects of the film complicate matters. As far as the Mo^{5+} ions are concerned, it is important to keep in mind that these species might interfere with the characteristics of the other defects. On the other hand, the bulk centers found for the films grown at 300 K sometimes hamper the interpretation of the EPR data due to their spectral overlap with the signals of the surface species. Since no way could be found to overcome the imperfections appearing by growing films at different temperatures, a strategy to obtain preparation-independent results by comparing ones obtained on films grown at 600 K with the ones grown at 300 K was undertaken.

First, paramagnetic point defects created on MgO film surface by different methods were studied. The EPR experiments show that paramagnetic surface color centers, F_s^+, are formed after the deposition of small amounts of Mg at low temperatures (50 K) on MgO(001) single-crystalline thin films. These centers are assigned to unpaired electrons trapped at morphological defects of the MgO surface. The number of Mg-induced F_s^+ centers goes through a maximum with increasing Mg coverage then decreases for Mg coverages above 0.03 ML. The depletion of the color centers at higher coverage is attributed to the formation of metallic magnesium clusters, which was confirmed by IR spectroscopy using CO as a probe molecule. It is found that CO binds to Mg clusters weakly (binding energy around 0.14 eV). The metallic Mg clusters are stable only at low temperatures and become oxidized even at 100 K. The second way of producing F_s^+ centers on single-crystalline MgO(001) thin films examined within this thesis is by contacting the film with hydrogen atoms at 100 K. The unpaired electrons are found to be trapped at morphological defects of the MgO surface, close to the hydrogen nucleus, as shown by isotope-substitution experiments.

In addition, surface oxygen radicals were investigated. The adsorption of

molecular oxygen on ultrathin MgO films was studied and provided the first unambiguous proof for the spontaneous activation of molecular oxygen forming an O_2^- radical upon adsorption on an ultrathin MgO(001) film. The reduction of the g_{zz} component observed for the ultrathin film in comparison with the MgO powder provided the first experimental evidence for the presence of a polaronic distortion predicted by theory. The other type of oxygen radical considered within this thesis is O^- centers. It was shown that O^- centers on single crystalline MgO(001) thin films can be produced by reaction of nitrous oxide with surface paramagnetic color centers. Angular-dependent EPR spectra show that these O^- radicals on MgO films are predominantly located on edges of MgO islands, which is in line with the location expected from the location of F_s^+ centers.

Bibliography

[1] `http://www.bruker-biospin.com` (2011).

[2] `http://www.fhi-berlin.mpg.de/KHsoftware/Balsac/index.html` (2011).

[3] `http://www.physicsarchives.com/index.php/courses/869` (2011).

[4] A. Abragam, *The principles of nuclear magnetism, vol.32, International Series of Monographs on Physics*, Claredon Press (1996).

[5] N. M. Atherton, *Principles of electron spin resonance*, Ellis Horwood PTR Prentice Hall (1993).

[6] P. W. Atkins, *Molecular Quantum Mechanics*, Oxford University Press (1997).

[7] A. Bals and J. Kliava, *Simulations of EPR spectra for d1 ions with distributed spin hamiltonian parameters*, J. Magn. Reson. **53**, 243 (1983).

[8] A. Bals *et al.*, *New approach to the EPR of d1 ions in glasses*, J. Phys. C **13**, L437 (1980).

[9] C. Barth and C. R. Henry, *Atomic Resolution Imaging of the (001) Surface of UHV Cleaved MgO by Dynamic Scanning Force Microscopy*, Phys. Rev. Lett. **91**, 196102 (2003).

[10] S. Benedetti *et al.*, *Morphology and optical properties of MgO thin films on Mo(001)*, Chem. Phys. Lett. **430**, 330 (2006).

[11] S. Benedetti *et al.*, *Structure and morphology of thin MgO films on Mo(001)*, Phys. Rev. B **78**, 195411 (2008).

[12] S. Benedetti *et al.*, *Spontaneous Oxidation of Mg Atoms at Defect Sites in an MgO Surface*, J. Phys. Chem. **115**, 3684 (2011).

[13] H.-M. Benia *et al.*, *Electron trapping in misfit dislocations of MgO thin films*, Phys. Rev. B **81**, 241415 (2010).

[14] B. Bennett *et al.*, *Multiple States of the Molybdenum Centre of Dimethylsulphoxide Reductase from Rhodobacter Capsulatus Revealed by EPR Spectroscopy*, Eur. J. Biochem. **225**, 321 (1994).

[15] R. Berger and M. Haddad, *Computer Simulations of ESR Spectra of Amorphous Thiomolybdates*, Phys. Stat. Sol. (b) **163**, 463 (1991).

[16] H. Bielawa *et al.*, *The Ammonia-Synthesis Catalyst of the Next Generation: Barium-Promoted Oxide-Supported Ruthenium*, Ang. Chem. Int. Ed. **40**, 1061 (2001).

[17] G. Blyholder, *Molecular Orbital View of Chemisorbed Carbon Monoxide*, J. Phys. Chem. **68**, 2772 (1964).

[18] D. Boudlich *et al.*, *Mo5+ ions as EPR structural probes in molybdenum phosphate glasses*, J. Non-Cryst. Sol. **224**, 135 (1998).

[19] Cabrera, *Theory of the oxidation of metals*, Rep. Progr. Phys. **12**, 163 (2002).

[20] C. T. Campbell, *Ultrathin metal films and particles on oxide surfaces: structural, electronic and chemisorptive properties*, Surf. Sci. Rep. **27**, 1 (1997).

[21] J. Carrasco *et al.*, *Bulk and surface oxygen vacancy formation and diffusion in single crystals, ultrathin films, and metal grown oxide structures*, J. Chem. Phys. **125** (2006).

[22] M. Che *et al.*, *EPR Studies on the Formation of O- Ions on Reduced Silica-Supported Molybdenum Catalysts Prepared by the Grafting Method*, J. Phys. Chem. **89**, 4526 (1985).

[23] M. Che and A. J. Tench, *Characterization and Reactivity of Molecular Oxygen Species on Oxide Surfaces* edited by D. Eley, H. Pines and B. Weisz, Paul, *Advances in Catalysis*, volume 32, pp. 1–148, Academic Press (1983).

[24] M. S. Chen and D. W. Goodman, *Ultrathin, ordered oxide films on metal surfaces*, J. Phys.: Cond. Matt. **20**, 264013 (2008).

[25] M. Chiesa *et al.*, *Continuous wave electron paramagnetic resonance investigation of the hyperfine structure of* $^{17}O_2$ *- adsorbed on the MgO surface*, J. Chem. Phys. **116**, 4266 (2002).

[26] M. Chiesa *et al.*, *First Evidence of a Single-Ion Electron Trap at the Surface of an Ionic Oxide*, Angew. Chem. Int. Ed. **42**, 1759 (2003).

[27] M. Chiesa *et al.*, *Single Electron Traps at the Surface of Polycrystalline MgO: an Assignment of the Main Trapping Sites*, J. Phys. Chem. B **109**, 7314 (2005).

[28] M. Chiesa *et al.*, *Excess Electrons Stabilized on Ionic Oxide Surfaces*, Acc. Chem. Res. **39**, 861 (2006).

[29] M. Chiesa *et al.*, *Multi-frequency high-field EPR study of (H+)(e-) pairs localized at the surface of polycrystalline MgO*, Chem. Phys. Lett. **438**, 285289 (2007).

[30] M. Chiesa *et al.*, *O- radical ions on MgO: a tool for a structural description of the surface*, Res. Chem. Interm. **28**, 205 (2002).

[31] J. S. Corneille *et al.*, *XPS characterization of ultra-thin MgO films on a Mo(100) surface*, Surf. Sci. **306**, 269 (1994).

[32] C. Di Valentin *et al.*, *O- radical anions on polycrystalline MgO*, Surf. Sci. **521**, 104 (2002).

[33] O. Diwald *et al.*, *H2 chemisorption and consecutive UV stimulated surface reactions on nanostructured MgO*, Phys. Chem. Chem. Phys. **1**, 713 (1999).

[34] O. Diwald and H. Knözinger, *Intermolecular electron transfer on the surface of MgO nanoparticles*, J. Phys. Chem. B **106**, 3495 (2002).

[35] Z. Dohnalek *et al.*, *Physisorption of CO on the MgO(100) surface*, J. Phys. Chem. B **105**, 3747 (2001).

[36] R. S. Drago, *Physical Methods in Chemistry*, W B Saunders, Philadelphia (1977).

[37] G. Ertl *et al.*, *Handbook of Heterogeneous Catalysis*, Wiley-VCH (2008).

[38] E. Fermi, *Über die magnetischen Momente der Atomkerne*, Z. Phys. A **60**, 320 (1930).

[39] A. M. Ferrari and G. Pacchioni, *Electronic Structure of F and V Centers on the MgO Surface*, J. Phys. Chem. **99**, 17010 (1995).

[40] A. M. Ferrari and G. Pacchioni, *Metal Deposition on Oxide Surfaces: A Quantum-Chemical Study of the Interaction of Rb, Pd, and Ag Atoms with the Surface Vacancies of MgO*, J. Phys. Chem. **100**, 9032 (1996).

[41] H. J. Freund *et al.*, *Preparation and characterization of model catalysts: from ultrahigh vacuum to in situ conditions at the atomic dimension*, J. Cat. **216**, 223 (2003).

[42] H.-J. Freund and G. Pacchioni, *Oxide ultra-thin films on metals: new materials for the design of supported metal catalysts*, Chem. Soc. Rev. **37**, 2224 (2008).

[43] P. Frondelius *et al.*, *Adsorption and activation of O_2^- at Au chains on MgO/Mo thin films*, Phys. Chem. Chem. Phys. **12**, 1483 (2010).

[44] M. C. Gallagher *et al.*, *Structure of ultrathin MgO films on Mo(001)*, Thin Solid Films **445**, 90 (2003).

[45] M. Gerloch, *Magnetism and ligand-field analysis*, Cambridge University Press (1993).

[46] E. Giamello, private communication (2010).

[47] E. Giamello *et al.*, *Electron-Paramagnetic-Resonance Investigation of the Interaction of Co with the Surface of Electron-Rich Magnesium-Oxide -*

Evidence for the Co- Radical-Anion, J. Chem. Soc.-Faraday Trans. **89**, 3715 (1993).

[48] E. Giamello *et al.*, *Surface Color-Centers on Magnesium-Oxide Generated by Magnesium and Alkali-Metal Doping*, J. Chem. Soc.-Faraday Trans. **90**, 3167 (1994).

[49] E. Giamello *et al.*, *Defect centers induced by evaporation of alkali and alkaline-earth metals on magnesium oxide: an EPR study*, J. Phys. Chem. **95**, 9385 (1991).

[50] L. Giordano *et al.*, *Tuning the surface metal work function by deposition of ultrathin oxide films: Density functional calculations*, Phys. Rev. B **73**, 045414 (Jan 2006).

[51] J. Günster *et al.*, *Mg clusters on MgO surfaces: Characterization with metastable impact electron spectroscopy, ultraviolet photoelectron spectroscopy (HeI), and temperature programmed desorption*, J. Vac. Sci. Technol. A **17**, 1657 (1999).

[52] A. Gonchar *et al.*, *Activation of Oxygen on MgO: O_2^- Radical Ion Formation on Thin, Metal-Supported MgO(001) Films*, Ang. Chem. Int. Ed. **50**, 2635 (2011).

[53] D. W. Goodman, *Model catalysts: from imagining to imaging a working surface*, J. Cat. **216**, 213 (2003).

[54] D. W. Goodman *et al.*, *Kinetics of the hydrogenation of CO over a single crystal nickel catalyst*, J. Cat. **63**, 226 (1980).

[55] W. Gordy, *Theory and Applications of Electron Spin Resonance*, John Wiley & Sons (1980).

[56] R. G. Greenler, *Infrared Study of Adsorbed Molecules on Metal Surfaces by Reflection Techniques*, J. Chem. Phys. **44**, 310 (1966).

[57] H. Grönbeck, *Mechanism for NO_2 Charging on Metal Supported MgO*, J. Phys. Chem. B **110**, 11977 11981 (2006).

[58] J. Gunn, *Microwave oscillations of current in III-V semiconductors*, Sol. St. Comm. **88**, 883 (1993).

[59] P. Gunter *et al.*, *Surface science approach to modeling supported catalysts*, Cat. Rev. - Sci. Eng. **39**, 77 (1997).

[60] J. Heidberg *et al.*, *The monolayer CO adsorbed on MgO(100) detected by polarization infrared spectroscopy*, Surf. Sci. **331-333**, 1467 (1995).

[61] A. Hellman *et al.*, *Low Temperature CO Oxidation over Supported Ultrathin MgO Films*, JACS **131**, 16636 (2009).

[62] B. Henderson and J. E. Wertz, *Defects in the alkaline earth oxides*, Adv. Phys. **17**, 749 (1968).

[63] C. Henry, *Surface studies of supported model catalysts*, Surf. Sci. Rep. **31**, 231 (1998).

[64] F. M. Hoffmann, *Infrared reflection-absorption spectroscopy of adsorbed molecules*, Surf. Sci. Rep. **3**, 107 (1983).

[65] P. Hollins, *The influence of surface defects on the infrared spectra of adsorbed species*, Surf. Sci. Rep. **16**, 51 (1992).

[66] P. Hollins and J. Pritchard, *Infrared studies of chemisorbed layers on single crystals*, Progr. Surf. Sci. **19**, 275 (1985).

[67] Z. Huesges, *Defect Chemistry of MgO Films: A Combined Theoretical and Experimental Approach*, Masther Thesis, Chemistry Department, FU Berlin (2011).

[68] L. Kantorovich *et al.*, *Mg clusters on MgO surfaces: characterization by MIES and electronic structure ab initio calculations*, Nucl. Instrum. Meth. B **157**, 162 (1999).

[69] W. Känzig and M. H. Cohen, *Paramagnetic Resonance of Oxygen in Alkali Halides*, Phys. Rev. Lett. **3**, 509 (1959).

[70] U. Katter, *ESR-Untersuchungen zum Adsorptionsverhalten und zur Dynamik von Di-tertiärem-butyl-nitroxid (DTBN) auf einkristallinen Oberflächen im Ultrahochvakuum*, PhD thesis, Chemistry Department, Ruhr-Universität Bochum (2010).

[71] E. Kieseritzky, *Adaptation of a W-Band EPR Spectrometer to UHV Conditions*, PhD thesis, Chemistry Department, FU Berlin (2010).

[72] A. Kiselev and V. Lygin, *Infrared Spectra of Surface Compounds*, Wiley (1975).

[73] M. Klaua *et al.*, *Growth, structure, electronic, and magnetic properties of MgO/Fe(001) bilayers and Fe/MgO/Fe(001) trilayers*, Phys. Rev. B **64**, 134411 (2001).

[74] P. F. Knowles, *Biological magnetic resonance volume 6: Edited by L J Berliner and J Reuben. pp. 300. plenum press, New York. 1984.*, Biochem. Ed. **14**, 43 (1986).

[75] T. Koenig *et al.*, *Measuring the Charge State of Point Defects on MgO/Ag(001)*, JACS **191**, 17544 (2009).

[76] A. Kolosov *et al.*, *ESR of O- and O2- stabilized on 95Mo ions in a molybdenum-silica gel support system*, Chem. Phys. Lett. **34**, 360 (1975).

[77] J. Kramer *et al.*, *Mechanism and kinetics of color center formation on epitaxial thin films of MgO*, Surf. Sci. **517**, 8797 (2002).

[78] L. D. Landau and E. M. Lifschitz, *Quantenmechanik*, Akademie-Verlag (1979).

[79] I. Langmuir, *A chemically active modification of hydrogen.*, JACS **34**, 1310 (1912).

[80] I. Langmuir, *The dissociation of hydrogen into atoms. [Part II.] Calculation of the degree of dissociation and the heat of formation.*, JACS **37**, 1139 (1915).

[81] I. N. Levine, *Quantum Chemistry*, 5.Aufl., Prentice Hall (2000).

[82] X. Lin *et al.*, *Charge-Mediated Adsorption Behavior of CO on MgO-Supported Au Clusters*, JACS **132**, 7745 (2010).

[83] L. Little, *Infrared Spectra of Adsorbed Species*, Academic (1966).

[84] C. Louis and M. Che, *EPR Investigation of the Coordination Sphere of Mo5+ Ions on Thermally Reduced Silica-Supported Molybdenum Catalysts Prepared by the Grafting Method*, J. Phys. Chem. **91**, 2875 (1987).

[85] D. J. Lowe *et al.*, *A new non-functional form of milk xanthine oxidase containing stable quinquivalent molybdenum.*, Biochem. J. **155**, 81 (1976).

[86] J. H. Lunsford, *The Catalytic Oxidative Coupling of Methane*, Angew. Chem.-Int. Edit. **34**, 970 (1995).

[87] L. Marchese *et al.*, *Dynamic and static interactions in CO layers adsorbed on MgO smoke (100) facelets: a FTIR and HRTEM study*, Surf. Sci. **269-270**, 135 (1992).

[88] K. P. McKenna and A. L. Shluger, *Electron-trapping polycrystalline materials with negative electron affinity.*, Nature Mat. **7**, 859 (2008).

[89] H. L. Meyerheim *et al.*, *Geometrical and Compositional Structure at Metal-Oxide Interfaces: MgO on Fe(001)*, Phys. Rev. Lett. **87**, 076102 (Jul 2001).

[90] E. G. Musaev *et al.*, *ESR studies of Mo–Mg oxide catalysts*, React. Kinet. Catal. Lett. **33**, 253 (1987).

[91] P. Myrach *et al.*, *Temperature-Dependent Morphology, Magnetic and Optical Properties of Li-Doped MgO*, Chem. Cat. Chem **2**, 854 (2010).

[92] F. Napoli *et al.*, *Formation of Superoxo Species by Interaction of O2 with Na Atoms Deposited on MgO Powders: A Combined Continuous-Wave EPR (CW-EPR), Hyperfine Sublevel Correlation (HYSCORE) and DFT Study*, Chem. A Eur. J. **16**, 6776 (2010).

[93] R. L. Nelson *et al.*, *Surface Reactivity of Irradiated Magnesium Oxide - Effects of Dose on Defect Concentrations Specific Surface Areas and Chemisorption Kinetics*, Trans. Faraday Soc. **64**, 2521 (1968).

[94] R. L. Nelson and A. J. Tench, *Chemisorption on Some Alkaline Earth Oxides 2. Intrinsic Bulk Defects and Adsorption of Oxygen on MgO, CaO, Sro*, Trans. Faraday Soc. **63**, 3039 (1967).

[95] R. L. Nelson *et al.*, *Chemisorption on Some Alkaline Earth Oxides 1. Surface Centres and Fast Irreversible Oxygen Adsorption on Irradiated MgO, CaO and SrO*, Trans. Faraday Soc. **63**, 1427 (1967).

[96] N. Nilius, private communication (2011).

[97] G. Pacchioni, *Quantum chemistry of oxide surfaces: From CO chemisorption to the identification of the structure and nature of point defects on MgO*, Surf. Rev. Lett. **7**, 277 (2000).

[98] G. Pacchioni, *Theory of point defects at the MgO surface, chapter 3*, Elsevier (2001).

[99] G. Pacchioni, private communication (2011).

[100] G. Pacchioni *et al.*, *Molecular orbital cluster model study of bonding and vibrations of CO adsorbed on MgO surface*, Int. J. Quant. Chem. **42**, 1115 (1992).

[101] G. Pacchioni *et al.*, *Cluster models of O2 adsorption on regular and defect sites and Fs centers of the MgO (100) surface*, Chem. Phys. Lett. **255**, 58 (1996).

[102] G. Pacchioni *et al.*, *Charging of Metal Atoms on Ultrathin MgO/Mo(100) Films*, Phys. Rev. Lett. **94**, 226104 (2005).

[103] G. Pinarello *et al.*, *O- radical ions on MgO as a tool to unravel structure and location of ionic vacancies at the surface of oxides: a coupled experimental and theoretical investigation*, Surf. Sci. **494**, 95 (2001).

[104] S. Pope *et al.*, *A theoretical study of the adsorption of simple molecules on MgO surfaces: CO, HCO, HOC, H2CO, HCOH, CH2OH and CH3O*, Surf. Sci. **139**, 299 (1984).

[105] P. A. Redhead, *Thermal desorption of gases*, Vacuum **12**, 203 (1962).

[106] D. Ricci *et al.*, *Paramagnetic Defect Centers at the MgO Surface. An Alternative Model to Oxygen Vacancies*, JACS **125**, 738 (2003).

[107] T. Risse, *ESR spectroscopy on well definded planar surfaces: from single atoms in ultrahigh vacuum to proteins under physiological conditions*, Habilitation Thesis, TU Berlin (2007).

[108] R. Ryberg, *Adsorption of molecules on free-electron-like metals: CO on Al(100)*, Phys. Rev. B **37**, 2488 (1988).

[109] S. Schintke *et al.*, *Insulator at the Ultrathin Limit: MgO on Ag(001)*, Phys. Rev. Lett. **87**, 276801 (2001).

[110] H. Schlienz *et al.*, *Electron Spin Resonance Investigation of the Molecular Dynamics of NO_2 on Al_2O_3(111) under Ultrahigh Vacuum Conditions*, Phys. Rev. Lett. **74**, 761 (1995).

[111] J. Schmidt *et al.*, *Characterization of a model Ziegler-Natta catalyst for ethylene polymerization*, J. Chem. Phys. **116**, 10861 (2002).

[112] E. G. Sharoyan *et al.*, *EPR and Spin-Lattice Relaxation of Mo*, Phys. Stat. Sol. (b) **66**, 773 (1974).

[113] D. R. Smith and A. J. Tench, *Reaction of Hydrogen Atoms at Oxide Surfaces*, Chem. Commun. **826**, 1113 (1968).

[114] J. Spaeth, *Atomic hydrogen and muonium in alkali halides*, volume 32, Springer Netherlands (1986).

[115] G. Spoto *et al.*, *Carbon monoxide MgO from dispersed solids to single crystals: A review and new advances*, Progr. Surf. Sci. **76**, 71 (2004).

[116] M. Sterrer *et al.*, *Identification of color centers on MgO(001) thin films with scanning tunneling microscopy*, J. Phys. Chem. B **110**, 46 (2006).

[117] M. Sterrer *et al.*, *Interaction of gold clusters with color centers on MgO(001) films*, Angew. Chem.-Int. Edit. **45**, 2630 (2006).

[118] M. Sterrer *et al.*, *Control of the charge state of metal atoms on thin MgO films.*, Phys. Rev. Lett. **98**, 096107 (2007).

[119] M. Sterrer *et al.*, *Crossover from three-dimensional to two-dimensional geometries of Au nanostructures on thin MgO(001) films: A confirmation of theoretical predictions.*, Phys. Rev. Lett. **98**, 206103 (2007).

[120] M. Sterrer *et al.*, *Energy transfer on the MgO surface monitored by UV-induced H2 chemisorption.*, JACS **125**, 195 (2003).

[121] M. Sterrer *et al.*, *Geometric characterization of a singly charged oxygen vacancy on a single-crystalline MgO(001) film by electron paramagnetic resonance spectroscopy*, Phys. Rev. Lett. **94**, 186101 (2005).

[122] M. Sterrer *et al.*, *Low temperature infrared spectra of CO adsorbed on the surface of MgO(001) thin films*, Surf. Sci. **596**, 222 (2005).

[123] M. Sterrer *et al.*, *CO adsorption on the surface of MgO(001) thin films.*, App. Cat. A: General **307**, 5861 (2006).

[124] S. Stoll and A. Schweiger, *EasySpin, a comprehensive software package for spectral simulation and analysis in EPR*, J. Mag. Res. **178**, 42 (2006).

[125] Y.-N. Sun *et al.*, *The Interplay between Structure and CO Oxidation Catalysis on Metal-Supported Ultrathin Oxide Films*, Ang. Chem. **122**, 4520 (2010).

[126] C. Tegenkamp *et al.*, *Defects in epitaxial insulating thin films*, J. Phys.-Condes. Matter **11**, 9943 (1999).

[127] A. J. Tench, *Temperature Effects on Hyperfine Coupling of a Surface Centre*, Surf. Sci. **25**, 625 (1971).

[128] A. J. Tench *et al.*, *Oxygen species adsorbed on oxides. Part 1.-Formation and reactivity of (O-)s on MgO*, J. Chem. Soc., Faraday Trans. 1 **68**, 1169 (1972).

[129] A. J. Tench and R. L. Nelson, *Adsorbed Nitro-Compounds and Electron Donor Properties of Magnesium Oxide*, Trans. Faraday Soc. **63**, 2254 (1967).

[130] A. J. Tench and R. L. Nelson, *Paramagnetic Defects Associated with Hydrogen Adsorbed on Surface of Magnesium and Calcium Oxides*, J. Colloid Interface Sci. **26**, 364 (1968).

[131] R. J. Tilley, *Principles and Applications of Chemical Defects*, Stanley Thornes, Cheltenham (1998).

[132] P. A. Tipler, *Physik*, Spektrum Akademischer Verlag (1994).

[133] S. P. Vincent and R. C. Bray, *Electron-paramagnetic-resonance studies on nitrate reductase from Escherichia coli K12.*, Biochem. J. **171**, 639 (1978).

[134] F. F. Volkenshtein, *Experiment and the electronic theory of catalysis*, Russ. Chem. Rev. **35**, 537 (1966).

[135] D. P. Wagner, H.J. and C. Schwerdtfeger, *EPR of Mo5+ in amorphous MoO3 thin films*, J. Non-Cryst. Sol. **34**, 335 (1979).

[136] H. Weber, *The Coloration of MgO-Crystals by Intrinsic Lattice Structures*, Z. Phys. **130**, 392 (1951).

[137] J. E. Wertz *et al.*, *Electron spin resonance studies of radiation effects in inorganic solids*, Discuss. Faraday Soc. **31**, 140 (1961).

[138] R. Wichtendahl *et al.*, *Thermodesorption of CO and NO from vacuum-cleaved NiO(100) and MgO(100)*, Phys. Stat. Sol. (A) **173**, 93 (1999).

[139] W. Williamson *et al.*, *The EPR spectrum of O- on magnesium oxide*, Chem. Phys. Lett. **9**, 33 (1971).

[140] N.-B. Wong and J. Lunspord, *EPR study of 17O- on magnesium oxide*, J. Chem. Phys. **55**, 3007 (1971).

[141] M. C. Wu *et al.*, *Synthesis and Characterization of Ultra-Thin Mgo Films on Mo(100)*, Chem. Phys. Lett. **182**, 472 (1991).

[142] N. Yaroslavsky and A. Terenin, Dokl. Akad. Nauk SSSR **66**, 885 (1949).

[143] M. Yulikov *et al.*, *Gold atoms and clusters on MgO(100) films; an EPR and IRAS study*, Surf. Sci. **603**, 1622 (2009).

[144] A. Zecchina *et al.*, *Defect Centers on Mg-Doped Mgo Surfaces*, Surf. Sci. **194**, 531 (1988).

[145] P. Zeeman, *On the Influence of Magnetism on the Nature of the Light Emitted by a Substance*, Astrophys. J. **5**, 332 (1897).

[146] C. Zupanc *et al.*, *The Interaction of Hydrogen with Ru/MgO Catalysts*, J. Cat. **209**, 501 (2002).

Abbreviations

3D	3 dimensional
AFM	Atomic Force Microscopy
AES	Auger Electron Spectroscopy
DFT	Density Functional Theory
EELS	Electron Energy Loss Spectroscopy
EPR	Electron Paramagnetic Resonance
FT IR	Fourier Transform Infrared
IRAS	Infrared Reflection Absorption Spectroscopy
L	Langmuir
LEED	Low Energy Electron Diffraction
ML	Monolayer
TPD	Temperature Programmed Desorption
STM	Scanning Tunneling Microscopy
UHV	Ultrahigh Vacuum
UV	Ultraviolet
XPS	X-Ray Photoelectron Spectroscopy

Zusammenfassung

In der vorliegenden Arbeit wird Elektronenspinresonanz (ESR) Spektroskopie verwandt, um eine Reihe paramagnetischer Defekte auf einkristallinen MgO(001)-Filmen unter Ultrahochvakuumbedingungen zu untersuchen. Neben den Punktedefekten, die das primäre Ziel dieser Arbeit darstellen, hat sich gezeigt, dass die verwandten MgO-Filme, die in diesem Fall auf einer Mo(001) Oberfläche gewachsen wurden, selbst auch über paramagnetische Zentren verfügen. Filme, die bei Raumtemperatur gewachsen werden, zeigen ein paramagnetisches Signal direkt nach der Präparation, das ungepaarten Elektronen in den vorhandenen Korngrenzen des MgO-Films zugeordnet werden kann. Beim Heizen auf 1100 K bei dem sich die langreichweitige Ordnung des Films deutlich erhöht verschwindet dieses Signal. Beschießt man die ausgeheizte Probe mit Elektronen (100 eV) so findet man erneut ein paramagnetisches Signal im Volumen des Films, das man Elektronen zuordnen kann, die in Schraubenversetzungen des Films lokalisiert sind. Wird der Film bei höherer Temperaturen (600 K) gewachsen, entstehen weniger eindimensionale Gitterfehler, so dass die oben beschriebenen Volumendefekte nicht auftreten. Allerdings findet man auf den so präparierten Oberflächen Mo^{5+}-Ionen. Die Untersuchung der verschiedenen Punktdefekte auf der MgO Oberfläche, die das eigentliche Ziel dieser Arbeit sind, werden im speziellen durch die Mo^{5+}-Ionen kompliziert, da diese redoxaktive Spezies sind und daher mit den chemisch reaktiven Defekten interferieren könnten. Aus diesem Grund wurden alle Untersuchungen auch an den bei Raumtemperatur präparierten Filmen durchgeführt, die diese Komplikation nicht haben. Auf der anderen Seite wird die detaillierte Analyse der Daten bei diesen Filmen durch die spektrale Überlappung mit den Volumenzentren erschwert. Die EPR-Experimente haben gezeigt, dass paramagnetische Farbzentren, F_s^+-Zentren, sowohl nach dem Auf-

dampfen kleiner Mengen an Mg als auch bei dem Kontakt mit Wasserstoff auf dünnen MgO-Filmen entstehen. Die Anzahl an Mg-induzierten F_s^+-Zentren in Abhängigkeit der Mg-Bedeckung weist ein Maximum auf, da bei höheren Mg-Bedeckungen Mg-Cluster gebildet werden. Letzteres wurde mit Hilfe der Infrarotspektroskopie (IR-Spektroskopie), bei der CO als Sondenmolekül verwandt wurde, nachgewiesen. Des Weiteren wurden Sauerstoffradikale auf der MgO-Oberfläche untersucht. Es wird gezeigt, dass bei der Adsorption von molekularem Sauerstoff auf ultradünnen MgO-Filmen, deren Dicke unterhalb von etwa 10 Monolagen ist, O_2^--Radikale entstehen. Eine detaillierte Analyse der ESR Parameter - genauer der g-Matrix- im Vergleich zu theoretischen Rechnungen liefert erste experimentelle Hinweise für eine Stabilisierung dieses Radikals aufgrund von polaronischen Verzerrungen, die von theoretischer Seite als wichtiger Grund für das Vorhandensein dieses aktivierten Zustands angesehen wird. Daneben wurden durch Reaktion von F_s^+-Zentren mit N_2O O^--Zentren erzeugt. Mit Hilfe winkelaufgelöster ESR-Experimente wird gezeigt, dass diese O^--Zentren bevorzugt Positionen zu finden sind, die entlang (100) äquivalenter Richtungen orientiert sind. Dies entspricht exakt den Erwartungen aufgrund der Historie dieser Zentren, da vorangegangene Untersuchen gezeigt hatten, dass die F_s^+-Zentren, aus denen die O^--Radikale erzeugt wurden, an den Stufenkanten der MgO-Inseln lokalisiert sind.

Abstract

In this work, different paramagnetic species on single crystalline MgO(001)/Mo(001) films are investigated by the means of electron paramagnetic resonance (EPR). It is shown by EPR that with the growth of MgO films at 300 K electrons trapped at grain boundaries of MgO domains appear, but disappear after annealing the film to 1100 K due to the rearrangements of the film. Subsequent electron bombardment of annealed films results in the appearance of trapped electrons at screw dislocations of MgO films. Growing the film at higher temperatures (600 K) leads to smaller amounts of line defects and better ordering, yet results in the appearence of Mo^{5+} ions on the surface of MgO(001) films. As both the films grown at 300 K and the films grown at 600 K exhibit imperfections, all experiments were performed and compared for both types of films, to achieve preparation-independent results. The EPR experiments have shown that paramagnetic surface color centers, F_s^+, appear after deposition of small amounts of Mg at low temperatures on MgO thin films, as well as after contact with hydrogen atoms. The number of Mg-induced F_s^+ centers goes through a maximum with increasing Mg coverage due to the formation of metallic Mg clusters, which was confirmed by infrared (IR) spectroscopy using CO as a probe molecule. Another aim of this thesis was to investigate oxygen radicals on the surface of MgO films. Here, the first unambiguous proof for the spontaneous activation of molecular oxygen forming an O_2^- radical upon adsorption on an ultrathin MgO(001) film is provided. Further, these experiments have given the first experimental evidence for the presence of the polaronic distortion predicted by theory. It is shown by angular-dependent EPR experiments that the O^- centers produced by reaction of nitrous oxide with F_s^+ centers are predominantly located on edges of MgO islands.

Publications

1. M. P. Lemeshko, E. S. Nazarenko, **A. A. Gonchar**, L. A. Reznichenko, O. Mathon, Y. Joly and R. V. Vedrinskii. *Phase transitions in lead-free piezoelectric ceramics: study of local atomic structure*, Europhys. Lett. 77 (2007), 26003.

2. M. P. Lemeshko, E. S. Nazarenko, **A. A. Gonchar**, L. A. Reznichenko, A. A. Novakovich, O. Mathon, Y. Joly and R. V. Vedrinskii. *XAFS studies of the local atomic structure of the lead-free piezoelectric ceramics* $K_xNa_{1-x}NbO3$ *over the temperature range 10-1023 K*, Phys. Rev. B. 76 (2007), 134106.

3. A. Lapierre, J. R. Crespo Lopez-Urrutia, T. M. Baumann, S. W. Epp, **A. Gonchar**, A. J. Gonzalez Martinez, G. Liang, A. Rohr, R. Soria Orts, M. C. Simon, H. Tawara, R. Versteegen and J. Ullrich. *Compact soft x-ray spectrometer for plasma diagnostics at the Heidelberg Electron Beam Ion Trap*, Rev. Sci. Instrum. 78 (2007), 123105.

4. G. S. Pokrovski, J. Roux, J.-L. Hazemann, A. Yu. Borisova, **A. A. Gonchar** and M. P. Lemeshko. *In situ X-ray absorption spectroscopy measurement of vapor-brine fractionation of antimony at hydrothermal conditions*, Min. Mag. 72(2) (2008), 667.

5. G. Y. Liang, J. R. Crespo Lopez-Urrutia, T. M. Baumann, S. W. Epp, **A. Gonchar**, A. Lapierre, P. H. Mokler, M. C. Simon, H. Tawara, V. Maeckel, K. Yao, G. Zhao, Y. Zou, and J. Ullrich. *Experimental Investigations of Ion Charge Distributions, Effective Electron Densities, and Electron-Ion Cloud Overlap in Electron Beam Ion Trap Plasma Using Extreme-Ultraviolet Spectroscopy*, Astrophys. J. 702 (2009), 838.

6. G. Y. Liang, T. M. Baumann, J. R. Crespo Lopez-Urrutia, S. W. Epp, H. Tawara, **A. Gonchar**, P. H. Mokler, G. Zhao, and J. Ullrich. *Extreme-ultraviolet spectroscopy of Fe VI-Fe XV and its diagnostic application for electron beam ion trap plasmas*, Astrophys. J. 696 (2009), 2275.

7. J. C. Lian, E. Kieseritzky, **A. Gonchar**, M. Sterrer, J. Rocker, H.-J. Gao, T. Risse. *N_2O adsorption on the surface of MgO(001) thin films: an infrared and TPD study*, J. Phys. Chem. C 114 (2010), 3148.

8. H.-M. Benia, P. Myrach, **A. Gonchar**, T. Risse, N. Nilius, H.-J. Freund *Electron trapping in misfit dislocations of MgO thin films*, Phys. Rev. B 81 (2010), 241415(R)-1-4.

9. P. Myrach, N. Nilius, S. Levchenko, **A. Gonchar**, T. Risse, K.-P. Dinse, L. A. Boatner, W. Frandsen, R. Horn, H.-J. Freund, R. Schlögl, M. Scheffler *Li-doped MgO: Temperature dependent morphology, magnetic and optical properties*, Chem. Cat. Chem. 2 (2010), 854.

10. **A. Gonchar**, T. Risse, E. Giamello and H.-J. Freund. *Additive coloring of thin, single crystalline MgO(001) films*, Phys. Chem. Chem. Phys. 12 (2010), 12520.

11. **A. Gonchar**, T. Risse, H.-J. Freund, L. Giordano, C. Di Valentin, and G. Pacchioni, *On the activation of oxygen on MgO: O_2^- formation on thin MgO(001) films*, Ang. Chem. Int. Ed. 50 (2011), 2635-2638.

12. **A. Gonchar**, T. Risse, H.-J. Freund, L. Giordano, C. Di Valentin, and G. Pacchioni, *Aktivierung von molekularem Sauerstoff auf MgO: Bildung von O_2^- auf dünnen, trägerfixierten MgO(001)-Filmen*, Ang. Chem. 123 (2011), 2684-2687.

Curriculum Vitae

For reasons of data protection,
the curriculum vitae is not included in the online version